ROAMING IN THE DARK:

DECIPHERING THE MYSTERY OF $NO_3 \rightarrow NO + O_2$ PHOTOLYSIS

A Dissertation

by

MICHAEL PATRICK GRUBB

Submitted to the Office of Graduate Studies of
Texas A&M University
in partial fulfillment of the requirements for the degree of

DOCTOR OF PHILOSOPHY

May 2012

Major Subject: Chemistry

Roaming in the Dark: Deciphering the Mystery of $NO_3 \rightarrow NO + O_2$ Photolysis

ROAMING IN THE DARK:

DECIPHERING THE MYSTERY OF $NO_3 \rightarrow NO + O_2$ PHOTOLYSIS

A Dissertation

by

MICHAEL PATRICK GRUBB

Submitted to the Office of Graduate Studies of
Texas A&M University
in partial fulfillment of the requirements for the degree of

DOCTOR OF PHILOSOPHY

Approved by:

Chair of Committee,	Simon W. North
Committee Members,	David H. Russell
	Robert R. Lucchese
	David A. Church
Head of Department,	David H. Russell

May 2012

Major Subject: Chemistry

ABSTRACT

Roaming in the Dark:

Deciphering the Mystery of $NO_3 \rightarrow NO + O_2$ Photolysis. (May 2012)

Michael Patrick Grubb, B.S., Texas A&M University

Chair of Advisory Committee: Dr. Simon W. North

The focus of this dissertation is to decipher the previously unknown reaction dynamics of NO_3 photodissociation. Although the $NO + O_2$ products are known to catalyze atmospheric ozone destruction, the mechanism by which these products are formed has remained a mystery, and no energetically accessible transition state has ever been calculated. Using velocity map ion imaging experiments to carefully study the stereochemistry of the product fragments combined with theoretical calculations performed by Drs. Xiao, Maeda, and Morokuma at Kyoto University, we have determined that the reaction proceeds exclusively via the unusual "roaming mechanism", with no evidence of a competing traditional transition state pathway. Within, the significance of this discovery is discussed in regards to both the NO_3 system and roaming dynamics in general, for which this system has provided new insight.

DEDICATION

This manuscript is dedicated to Dr. Simon North

ACKNOWLEDGEMENTS

At least 27 thanks are in order.

Thank you father, for being obsessed with airplanes. Being obsessed with things is trait which has proven profoundly useful in both enjoying and succeeding in life.

Thank you mother, you were my very first and still very best teacher. Thank you for raising me to enjoy learning, and for always believing that I am capable of whatever I put my mind too.

Thank you sister, with whom I conducted my very first chemistry experiments by mixing shampoos together in Dixie cups. Sadly our results were not publishable.

Thank you brother, for all of the creative projects and philosophical studies we have undertaken together. Your interest in things has always reaffirmed my own. Of the limited number of the "real people" in the world, you are the realest.

Kristin, thank you for teaching me the beauty of Ion Imaging. You are positive person and a patient mentor, and I'm sure you will do a great job inspiring your students at Arkansas State.

Thank you Michelle, we had a lot of great times running the experiment together. I pass on the sacred responsibility of the Imaging Chamber to your capable hands. Make me proud, little sister.

Thank you Rodrigo, you are a great researcher and I am proud to call you my rival. Thank you Buddhadeb, you were a lot of fun to work with and a much better scientist than you think you are. Thank you Qingnan, you are an amazing

experimentalist and a great all-around human being; I shall miss our laboratory guitar sessions. I hope to meet all three of you again someday as faculty colleagues.

Thank you Monica for helping me figure out how to use the copier so many different times, and Sandy for making all of the confusing graduate school paperwork so easy. Thank you Will for re-drilling all of the parts I told you the wrong dimensions for, and Bill for fixing all of the bubblers I accidently closed the fume-hood door on.

Thank you Michael, Hudson, and Aaron for all of the fun times. Thank you Kurt and Nic for being awesome and enthusiastic coworkers. I wish you both great success in your graduate schooling (by the Kurt, it's never too late to become a scientist).

Thank you Daniel for being one of the few people I can nerd out about physics and math with, sometimes I forget you are still just an undergrad. You're going to be a great PhD (the Science is strong in this one). Thank you Laura, your cheerful attitude always puts me in a good mood. You have a bright future as well. I hope the three of us will remain friends as we go our separate ways.

Thank you Drs. Morokuma, Maeda, Xiao, and Eisfeld for your insight and collaboration on the wonderful molecule that is NO_3, and Dr. Rakitzis for your help in understanding fragment vector correlations. Thank you Dr. Peterson for your insight into and ab initio calculations on the BrO system, which I have shamefully yet to utilize.

Dr. Hall, you are an inspiring and idealistic scientist. Thank you for all of the earnest help and advice you have given me, I could not have created the vector correlation equations or identified the NO Λ doublet propensities without you.

Dr. Gao, you were the first to encourage me to become a scientist. Thank you for believing in me. I hope things are going well for you in Beijing.

Finally, I must thank the person who has had the largest influence on my scientific development, Dr. Simon North. I did not really feel like a scientist until a joined your group. Thank you for making me feel like I had ownership over my project, you have always provided me with the perfect balance of instruction and independence. Thank you for the daily science discussions and coffee trips; they have helped me develop clear ways of thinking about research. Thank you for being excited about every piece of data I showed you, if you didn't care so much I don't think I would have either. Thank you for all of the encouraging late night phone calls to the lab when you knew I was working. Thank you for making me feel that I am exceptional. You are the best advisor I could have possibly chosen, and of all of the great scientists I in the world I would not have wished for any other.

Thank you.

TABLE OF CONTENTS

CHAPTER Page

LIST OF FIGURES

LIST OF TABLES

PROLOGUE

There were no windows in the tiny basement laboratory of Chappuis's Parisian apartment, so he could not see that the sky was blue, but he knew it to be true all the same. Everyone knew that the sky was blue, they had always known it, even before colors were given their names. What they did not know, however, was why. 'Except for me,' Chappuis thought giddily as he strained against the crank of his hand pump, watching the mercury level in the barometer slowly fall downwards. 'I'll know why the sky is blue, after today. For the first time in human history, I'll know.'

He would know for certain, anyway. Last month he had gotten his first clue when he and his good friend Mr. Hautefeuille had succeeded in liquefying ozone in their little vacuum chamber (although at that time, he has been increasing instead of decreasing the pressure with the hand pump). A dark blue mist had appeared moments after they had released the trapped oxygen through their electrical discharge. Mr. Hautefeuille had thought of the electrical discharge idea, and Chappuis had to agree it was a clever one. After all, one could clearly smell the ozone in the air after an electrical storm. They had presented their ozone liquefaction results at the recent meeting of the French Academy, to great acclaim.

While there, Chappuis had overheard something else as well: at King's College, Mr. William Hartley had deduced that the reason for the sharp cutoff in the ultraviolet region of the solar spectrum was due to the large presence of ozone in the upper atmosphere. The discovery had given him idea. Could ozone also account for the sky's blue color? Obviously liquid ozone was blue, but Chappuis needed to confirm the same was true for the gas to prove his theory. Furthermore, he had to obtain a more quantitative absorption spectrum to work out the necessary calculations. He had spent the past month modifying the chamber and constructing different lengths of glass tubing. Ten tubes had been constructed, varying in length from 0.25-2.00 meters. This would allow him to determine the absorption cross sections of the spectral lines. He was pumping down the largest of them now, to give him the most signal on his first attempt. The Mercury level fell just below the notch he had scratched in the glass to indicate his desired pressure. An excited, cackling laughter escaped his throat. It was ready.

Chappuis flipped on his electrical discharge, opened the oxygen source, and lit the Drummond lamp in front of the absorption cell. The intense glow emanating from the ignited calcium oxide filled the lab. Chappuis exhaled, and took a few moments to bask in the literal and metaphorical, for surely he would soon be famous, limelight before skipping around his experiment table to check the spectrometer. The light passing through the glass cell entered the spectrometer through a narrow slit, after

which the colors were separated by a prism and projected onto a white piece of paper beneath a mounted ruler. His eyes moved to the paper immediately, and a smile slowly crept across his cheeks. The red was missing. Ozone was blue.

He felt about frantically behind his back for the lab notebook to record the dark lines on the ruler where the light was missing, not wanting to take his eyes off of the beautiful results. Crack. His heart stopped. Had he damaged the chamber somehow? He glanced over at the barometer, and sure enough the pressure was slowly but steadily increasing. 'Chappuis, you fool!' he thought, picking up his pen and furiously trying to record the line positions before he ran out of time. But wait…what was this? New lines were appearing, and they weren't from molecules that he normally observed in air. He had memorized the positions of those. Something new was happening, a reaction was taking place with the ozone inside the cell. Chappuis absently jotted down the new line positions as well, maybe the new molecule would be of interest to somebody.

'Bah, it will take me all week to make a new absorption cell…'

CHAPTER I

THE EXPOSITION: BACKGROUND AND INTRODUCTION

"Everything must have a beginning ... and that beginning must be linked to something that went before."

-Mary Shelley

What Chappuis had accidently discovered that day was the nitrate radical, NO_3.[1] The leak in his vacuum chamber allowed atmospheric nitrogen gas to pass through his electrical discharge, creating a variety of NO_x compounds for which he recorded the absorption spectrum. Interestingly, the method by which he had synthesized NO_3 is the same method utilized by nature, as NO_x compounds are produced from atmospheric lightning breakdown of air (N_2/O_2). In our modern age the majority of NO_x production is anthropogenic, being emitted as a byproduct of fossil fuel combustion. Any NO_3 produced during the daytime however is immediately destroyed by sunlight, which has lead NO_3 to be referred to as the "vampire molecule".[2] Following the absorption of a visible photon, NO_3 dissociates into one of two sets of products:

$$NO_3 + h\nu \rightarrow NO_2 + O \quad \text{(atomic elimination)}$$
$$\rightarrow NO + O_2 \quad \text{(molecular elimination)}$$

This dissertation follows the style of the *Journal of Chemical Physics*.

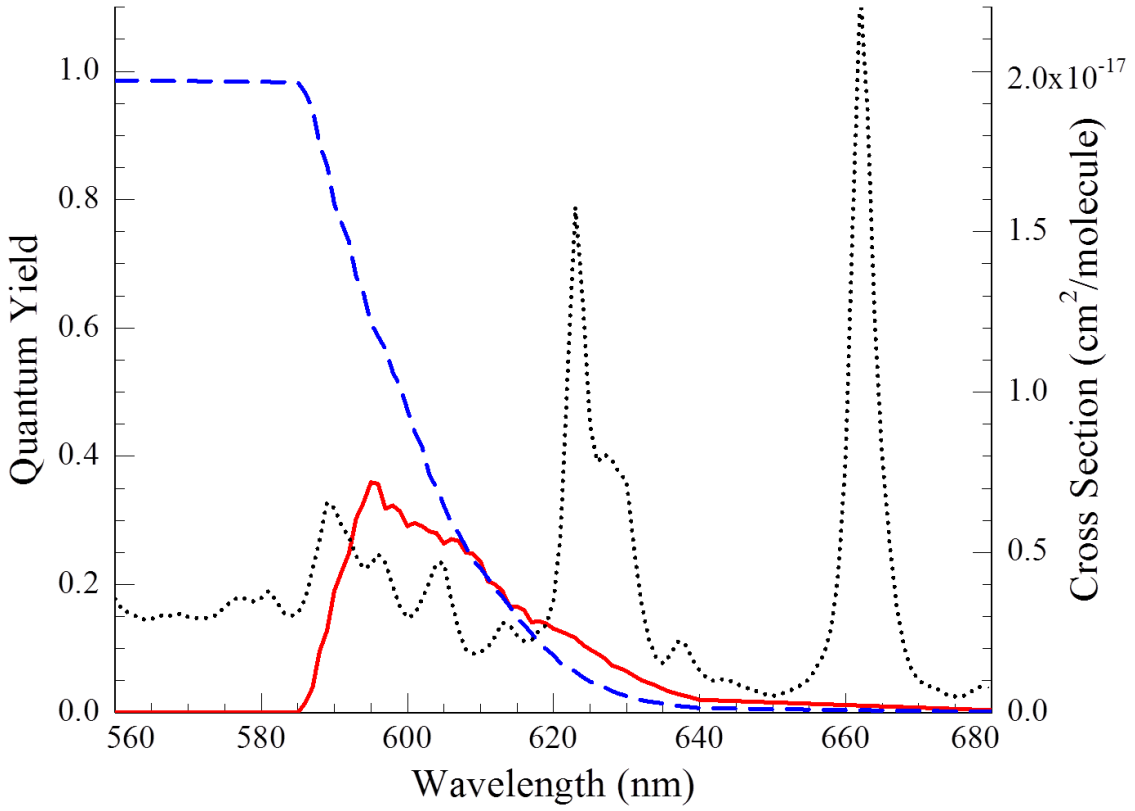

Figure 1: Absorption cross-section and product channel quantum yields of NO_3. Absorption cross section of NO_3 (dots) and wavelength dependent quantum yields of the two product channels: $O + NO_2$ (dashed line) and $O_2 + NO$ (solid line).

The atomic elimination channel (89% of atmospheric photoproducts) leads to a chemically null cycle, but the molecular elimination channel (11% of atmospheric photoproducts) is of considerable interest as it initiates the catalytic destruction of ozone via the following mechanism:[3]

$$
\begin{array}{lcl}
NO_3 + h\nu & \rightarrow & NO + O_2 \\
NO + O_3 & \rightarrow & NO_2 + O_2 \\
NO_2 + O_3 & \rightarrow & NO_3 + O_2 \\
\hline
\text{NET: } 2O_3 & \rightarrow & 3O_2
\end{array}
$$

Because of the potential significance of this channel, the branching ratio of these pathways as a function of photolysis wavelength have been carefully determined by Magnotta and Johnston,[4] and later by Johnston et al.[3] The molecular elimination channel takes place over a narrow range of wavelengths, from 594.5 to 585.5 nm at 0 K (Figure 1). Above the 585.5 nm threshold, the much faster atomic elimination channel is accessible which accounts for nearly 100% of the photoproducts at those wavelengths.

The 594.5 nm threshold for the molecular elimination channel was originally assumed to arise from the barrier of a "tight", concerted 3-center transition state,[5] however no such transition state at an accessible energy has previously been identified. Despite the atmospheric relevance of the reaction, the mechanism by which it occurs has remained a mystery. Finding this mechanism will be a central focus of this dissertation.

A. Chemical mechanisms

The dynamics tell the story of a chemical reaction, and describe how the electrons and nuclei of the reactant molecules rearrange themselves and move along a potential energy surface to form the product molecules. This story does not have a linear progression, however, as the molecule may explore the same region of the potential surface multiple times in a single trajectory. The available energy in the reactants redistributes amongst the available degrees of freedom of the molecule, until sufficient energy is allocated in the particular degree of freedom, the reaction coordinate q_{rxn}, to react. A more useful way to describe the mechanism is therefore by an intermediate structure known as the transition state, the dividing surface on the potential separating the reactants from the products through which all reacting trajectories must cross.

The identification of a transition state is critical to canonical rate theory, which defines the rate constant *k(T)* of a unimolecular reaction by the equation:

$$k(T) = \frac{k_b T}{h} \frac{Q^{\neq}(T)}{Q(T)} \exp(-E^{\neq}/k_b T) \quad (1.1)$$

Where $Q(T)$ and $Q^{\neq}(T)$ are the partition functions of the initial reactant molecule and the transition state respectively, and $E^{\neq}$ is the transition state energy. The transition state is rigorously defined as the dividing surface of minimum flux between the reactants and the products, where:

$$\frac{\partial k(T)}{\partial q_{rxn}} = 0 \quad (1.2)$$

A variational treatment of Equation 1.1 can therefore be used to determine the transition state location which results in the smallest reaction rate. Two competing terms govern the reaction rate and thus location of the transition state dividing surface: a statistical term $\frac{Q^{\neq}(T)}{Q(T)}$ which is minimized when the system has the lowest density of states (such as when a reactive complex is formed out of multiple species), and an energetic term $\exp(-E^{\neq}/k_b T)$ which is minimized at the highest energy point along the trajectory. This description of a transition state leads to the categorization of two broad types of transition states: 'tight' and 'loose'.

The potential energy surface governing 'loose' transition states often do not have an energetic maximum along the trajectory, and thus the location of the transition state is not immediately obvious and typically temperature dependant. Simple bond breaking, such as the $H_2CO + h\nu \rightarrow HCO + H$ reaction (**Figure 2**), is an example of a reaction with a 'loose' transition state. In this case the potential is broad and characterized by

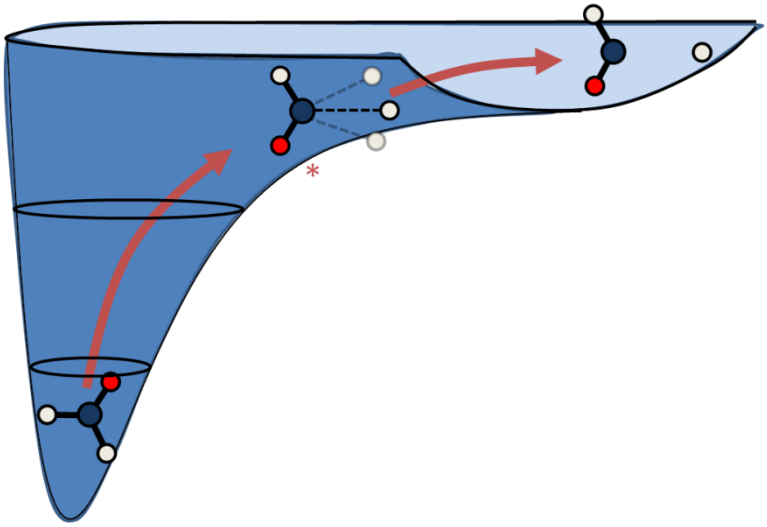

Figure 2: The schematic potential of the $H_2CO + h\nu \rightarrow HCO + H$ photolysis reaction in formaldehyde as an example of a 'loose' transition state. The location of the transition state (asterisk) is not obvious from the potential, and the exit channel dynamics are unconstrained and characterized by large amplitude motion.

low frequency motion, leading to unconstrained dynamics. The hydrogen atom can be pulled off at a variety of bond angles, and the majority of the trajectories do not necessarily follow the lowest energy path to the products. Typically, the internal energy in the product fragments associated with a loose transition state is statistically distributed, as there are no directed forces channeling the available energy into particular coordinates. The $NO_3 + h\nu \rightarrow NO_2 + O$ reaction is an analogous example, and measurements confirming the characterization of a 'loose' transition state are provided in Appendix B.

A 'Tight' transition state is simply the energetic maximum along the trajectory, independent of temperature. 'Tight' transition states generally arise in reactions where significant structural rearrangement of the atoms needs to occur, leading to a large

energy barrier between the reactants and products. The dynamics are highly constrained to a particular geometry, and are characterized by high frequency motion and a well-defined saddle point on the potential energy surface. These directed forces in the exit channel often lead to non-statistical energy distributions in the product fragments. The major pathway of the $H_2CO + h\nu \rightarrow CO + H_2$ reaction contains an example of a 'tight' transition state (**Figure 3**). A combination of symmetric in-plane and out-of-plane bending motion leads to a skewed transition state structure where the two hydrogen atoms can form a chemical bond, while simultaneously breaking their C-H bonds. The $NO_3 + h\nu \rightarrow NO + O_2$ should be analogous; however, no transition state structure with an accessible energy barrier has so-far been identified.

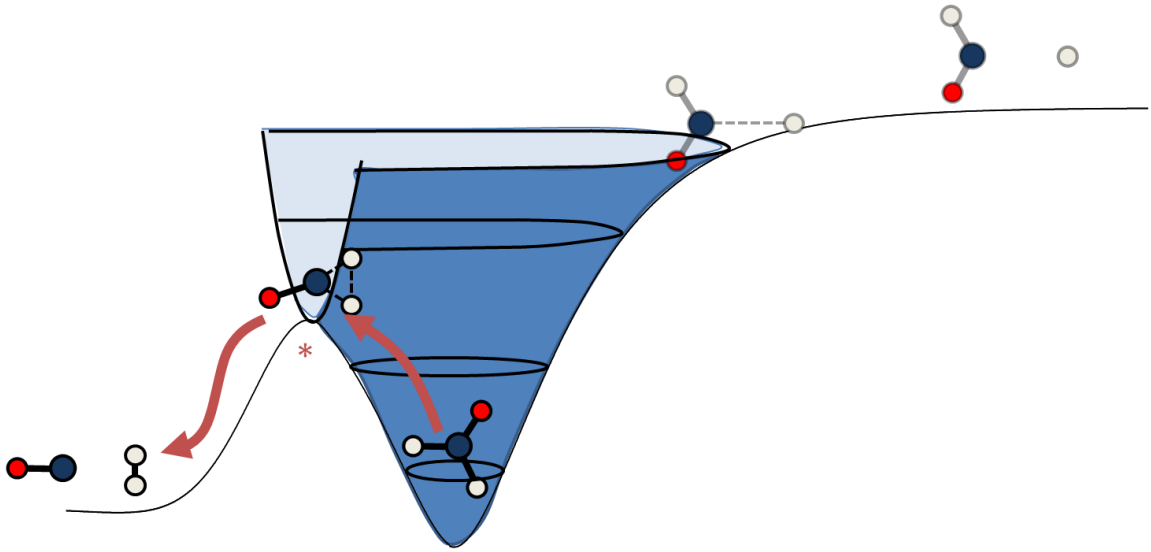

Figure 3: The schematic potential of the major pathway of the $H_2CO + h\nu \rightarrow CO + H_2$ photolysis reaction in formaldehyde as an example of a 'tight' transition state. The location of the transition state is given by the maximum energy along the reaction path (asterisk), which is governed by a constrained saddle point on the potential.

Recently, a second minor pathway has been identified in the $H_2CO + h\nu \rightarrow CO + H_2$ reaction, which is defies the conventional way of thinking about transition states.[6-7] The pathway is initiated by the loose elongation of a C-H bond, like the atomic elimination pathway, however the bond is not able to break. The H atom, still weakly bound, "roams" around the rest of the molecule until it encounters the other H atom and a bond is formed leading to the $CO + H_2$ products. This so-called 'roaming' mechanism bypasses the 'tight' transition state of the major pathway entirely, but leads to the same set of products (**Figure 4**). Several questions remain open regarding the nature of roaming dynamics: is it necessary for a circumvented 'tight' transition state pathway to exist for roaming to occur? Is roaming common? Is roaming always a minor pathway? Is roaming always governed by unconstrained 'loose' dynamics? How can we treat roaming using theoretical models, and what is the roaming transition state?

These are questions that will be addressed within this dissertation, as we will soon discover roaming dynamics play a large role in the NO_3 photodissociation.

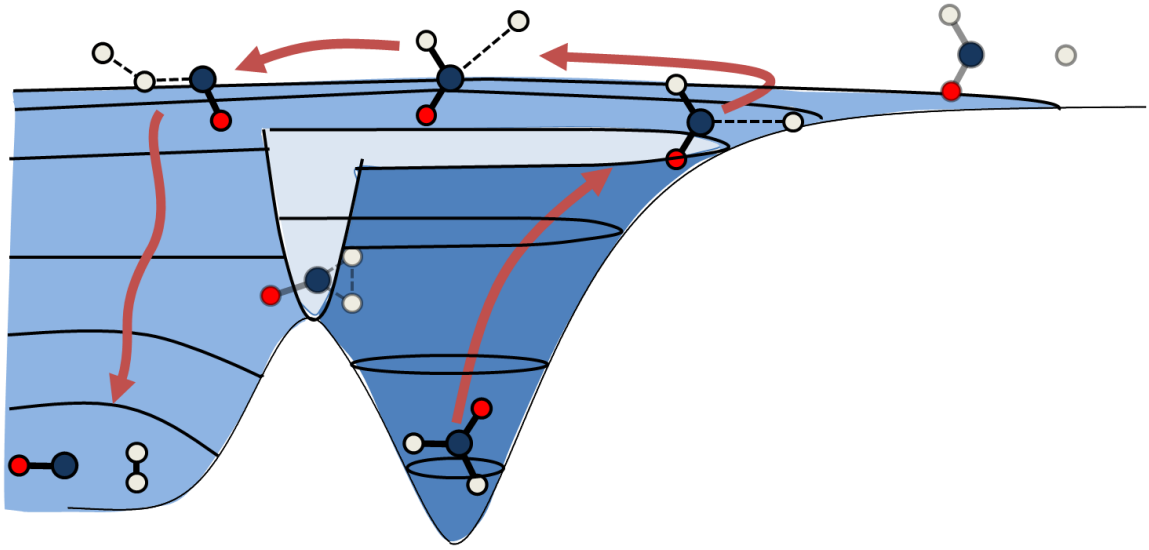

Figure 4: The schematic potential of the minor pathway of the $H_2CO + h\nu \rightarrow CO + H_2$ photolysis reaction in formaldehyde as an example of 'roaming' dynamics. The tight transition state has been bypassed by the loose dynamics of a frustrated $H_2CO \rightarrow HCO + H$ reaction. We are just now learning how to think about this type of reaction.

B. Dynamics from the top down

A molecular reaction involves a complicated maneuvering of atoms on a very short time scale (< 1 picosecond). Experimentally observing the reaction choreography in real-time is a difficult task, and requires the use of ultra-fast lasers. A simpler and sometimes more informative approach is to characterize a reaction through detailed measurements of the product fragments, which are sufficiently long-lived. The observed scalar and vector properties of the fragments can provide clues that may be used to decipher their founding mechanism.

A molecule is described by its quantum state ($^{\Sigma}\Lambda_{\Omega}$; v; N), which is comprised of three main components: rotational (N), vibrational (v), and electronic ($^{\Sigma}\Lambda_{\Omega}$). The degree of rotational and vibrational excitation in the product fragments may reveal the underlying forces and torques involved in the reaction, while the electronic configurations can tell us about the evolution of the chemical bonds themselves. The quantum state of a single product molecule can be detected spectroscopically, but knowing the quantum state of *both* product molecules (the NO and the O_2) originating from the same photodissociation event gives us a much better picture of the dynamics. When a molecule dissociates, the leftover energy goes into the fragment's recoil velocity. Because energy and momentum must always be conserved, if we measure a single product's quantum state *and* recoil velocity we can determine the quantum state of the coincident product as well. This idea is the heart of the velocity map ion imaging technique.[8-9] Furthermore, because velocity map ion imaging measures the fragment velocity vector, which includes a directional component as well as a magnitude, we can reveal directed forces and torques on the photofragments as well.[10]

CHAPTER II

THE EXPERIMENTAL APPARATUS

"A physicist is just an atom's way of looking at itself."
-Niels Bohr

If we want to measure a fragment's recoil velocity, it is crucial that the experiment be performed in a collision free vacuum. Additionally, if we want to measure only the momentum originating from photolysis, we need to dissociate a zero velocity (at least along the measurement plane) NO_3 molecule. To do this, we require the Ion Imaging Apparatus (Figure 5). The Apparatus is composed of three vacuum chambers: the source, main, and detector regions. The source and main chambers are differentially pumped by 6-inch oil diffusion pumps (Varian) backed by Welch 1410 mechanical pumps, capable of achieving pressures below 10^{-7} Torr, while the detector region is pumped by an oil-less turbo pump ($< 10^{-8}$ Torr) at all time.

Briefly, the Apparatus operates in the following way: First, the gas sample is brought through the inlet tube (A) and expanded into the source region by a solenoid pulse valve (B). Although the gas expands from the pulse valve nozzle in all directions, a conical skimmer (C) ensures only the molecules moving straight along the z-axis are able to pass through into the main chamber. Next, a pulsed laser fired through a quartz window in the side of the chamber intersects this beam of molecules and photolyzes the NO_3 into NO and O_2. A second pulsed laser then selectively ionizes a specific quantum state ($^{\Sigma}\Lambda_{\Omega}$; v; N) of the NO fragment, and the resulting NO^+ cation is accelerated by a set of focusing lenses (D) down the time of flight tube toward the position sensitive (in the

x-y plane) ion detector (E). Because the NO_3 molecules in the beam have no initial velocity in the x or y direction, the recoil velocity of the NO fragment can be determined by its displacement from the center of the detector. In this way, both the NO velocity and ($^{\Sigma}\Lambda_{\Omega}$; v; N) quantum state are simultaneously detected.

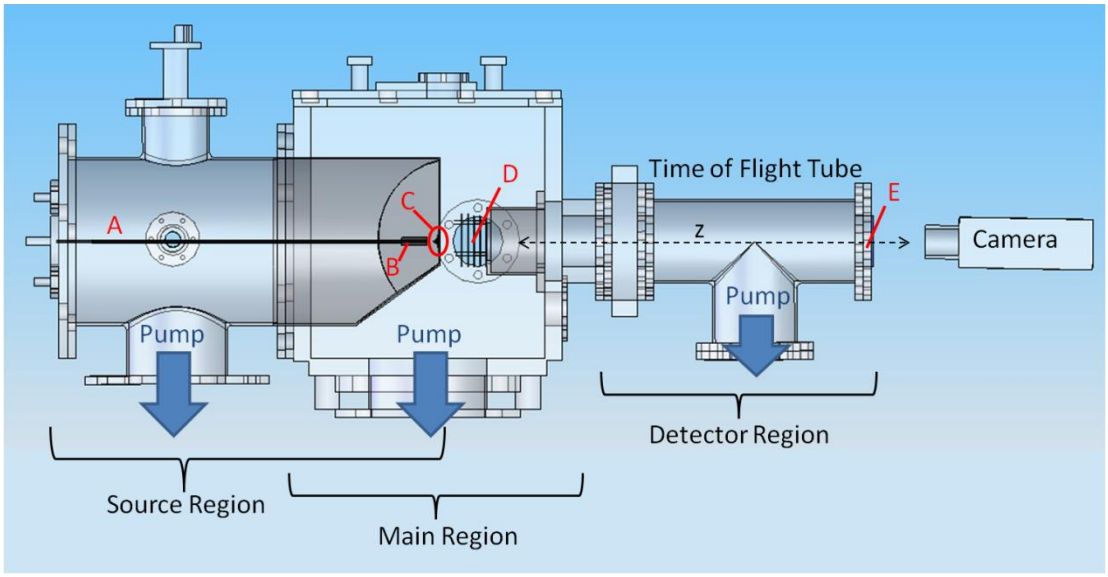

Figure 5: Diagram of the ion imaging apparatus. A) inlet tube, B) pulse valve, C) conical skimmer, D) ion optics array, E) MCP/Phosphor screen detector.

A. Generating NO_3

First, however, the NO_3 must be created. NO_3 is an open-shelled molecule, and thus highly reactive. The short lifetime of this molecule therefore necessitates that it is synthesized *in situ*, moments before it enters the collision free vacuum. Chappuis synthesized NO_3 in his leaky vacuum chamber by accident, through the electrical breakdown of ambient N_2 and ozone.[1] Electrical discharge, unfortunately, is not a suitable method for ion imaging experiments. The electrical discharge results in the

production of residual ions and electrons in the beam, undermining the experimental detection which relies on the selective ionization of particular molecular fragments. A different method for *in situ* synthesis of NO_3 is therefore required.

A convenient method of NO_3 generation is through the thermal decomposition of $N_2O_5 \rightarrow NO_3 + NO_2$ (ΔH_{rxn} = 22.21 kcal/mol). N_2O_5 is chemically stable at low temperatures, and is easily synthesized by gas phase mixing of NO_2 and Ozone.[11] The N_2O_5 then traps as a white powder at dry ice/acetone temperatures in a bubbler.

From there, the bubbler of trapped N_2O_5 is connected to the Teflon inlet tube (A) of the source chamber. The bubbler is then warmed to -15°C, a temperature at which N_2O_5 has a vapor pressure of ~7 Torr. A backing pressure of 800-1000 Torr of Helium is applied, resulting in a gas mixture of < 1% N_2O_5. The inlet tube is terminated by a solenoid pulse valve (Series 9, Parker Hannifin) inside the source chamber. This pulse valve is electromagnetically opened 10 times per second for 600 μs durations to release pulses of the gas mixture into the chamber. First, however, the gass passes through a ceramic tube wrapped in NiCr wire which is resistively heated to 650-750 K, generating NO_3 from N_2O_5 decomposition just moments before the gas expands into our collision-free vacuum. The free jet expansion of the gas mixture is then collimated into a molecular beam of NO_3 in Helium by a 0.8 mm conical skimmer as it enters the Main chamber as shown in Figure 6.

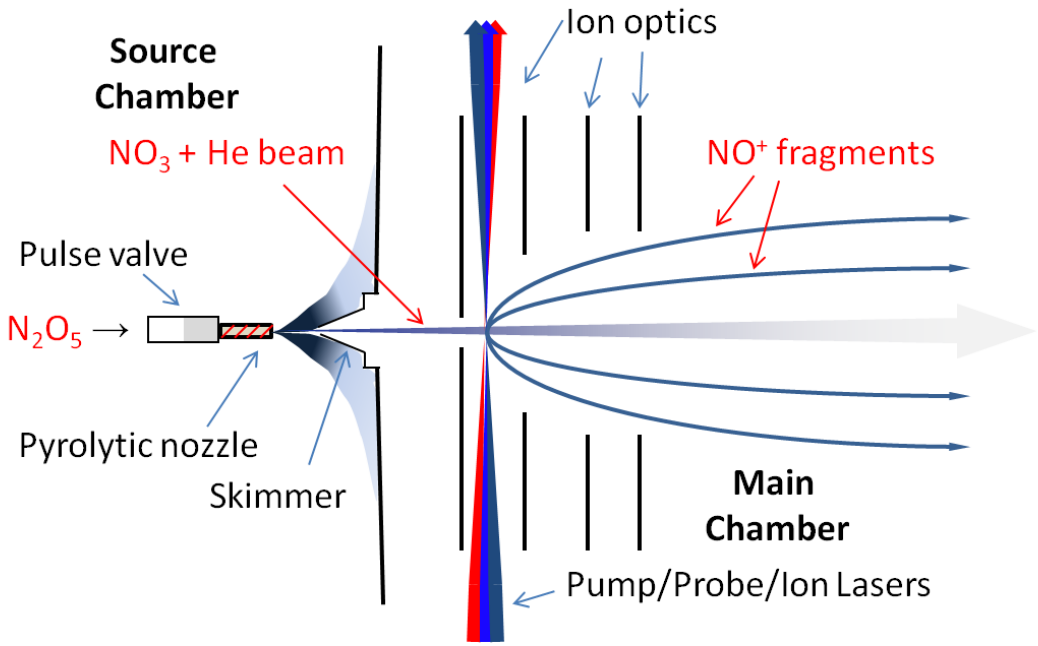

Figure 6: Diagram of the interaction region of the experimental apparatus.

B. Photolysis

We have now satisfied the prerequisites of our measurement. We have created a molecular beam of NO_3 (> 5 x 10^{12} molecules/cm^3) in a 10^{-7} Torr vacuum, which only has significant momentum in the z direction. Any momentum of the photofragments in the x and y directions will therefore arise from the recoil generated by the photolysis.

The NO_3 → NO + O_2 photolysis is initiated by a pulsed (~10 ns pulse width, 0.5 mJ/pulse) laser beam (Pump, Figure 6). The laser is generated by a tunable PDL dye laser (Kiton Red 620 dye) pumped by the 2nd harmonic output of an Nd:YAG laser (532 nm). Typically, a wavelength of 588 nm was utilized as the NO + O_2 channel yield is highest at that wavelength. After absorption of the photon, the NO_3 molecule has an

excited state lifetime of ~1 ns before dissociating into the NO and O_2 fragments.[12] The fragments are imparted with an average total recoil velocity of about 4000 m/s, and can be ejected in any direction. This results in a spherical distribution of fragments rapidly expanding in space, which we refer to as the Newton Sphere.

C. Photoionization

The NO fragments in the Newton Sphere are created in a wide distribution of quantum states, but our experiment requires that we are able to measure the velocity of only one of those quantum states at a time. This quantum state selection is achieved via a 1 + 1 Resonance Enhanced Multi-Photon Ionization (REMPI) scheme.[13] First, a resonant photon excites a particular NO ($^{\Sigma}\Lambda_{\Omega}$; v; N) state to an intermediate electronic state, and then a second non-resonant photon ejects the electron and creates an NO^{+} cation (Figure 7).

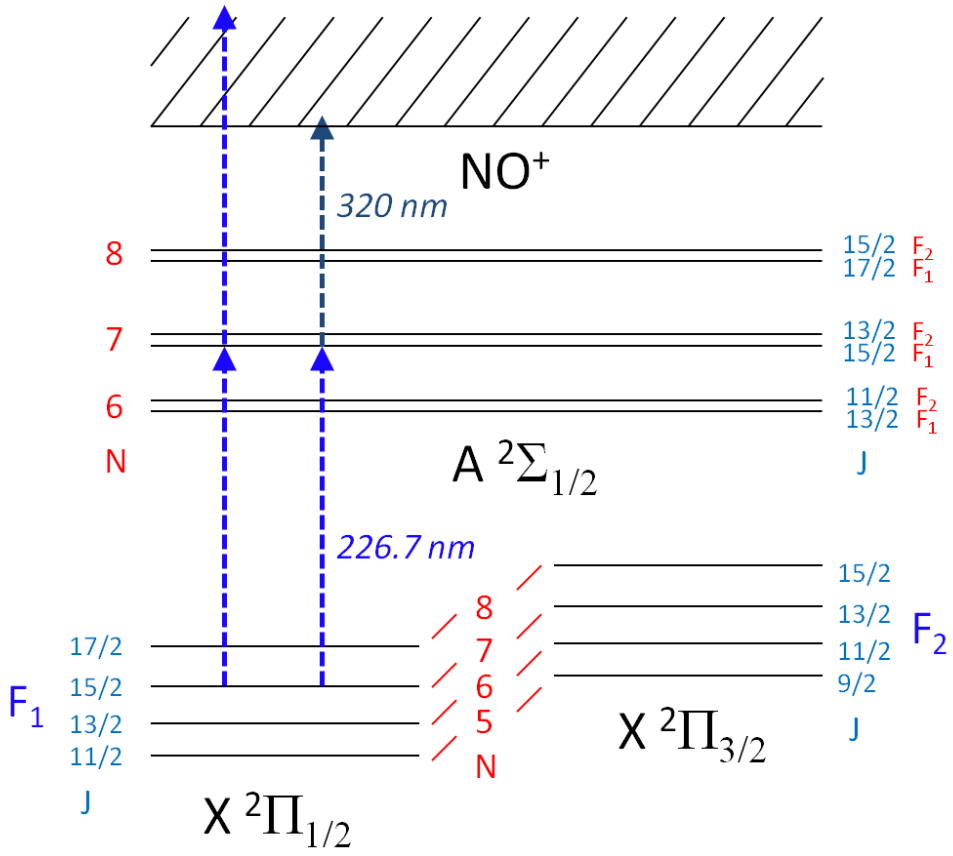

Figure 7: NO Resonance Enhanced Multi-Photon Ionization (REMPI) schemes. Shown are 1 + 1 and 1 + 1' REMPI schemes for ionizing NO ($^2\Pi_{1/2}$; v = 0; N=7). When a 1 + 1' REMPI scheme is employed, a separate non-resonant laser is used for the ionization step. Energy levels are not to scale, and Λ doublet splitting is not shown.

Most of the fragments were probed via the A ($^2\Sigma^+_{1/2}$; v = 0; N) ← X ($^2\Pi_\Omega$; v = 0; N) rotational band at ~225 nm. The ~225 nm photon was generated using the doubled 450 nm output of a LDL dye laser (Coumarin 450 dye) pumped by the third harmonic output of a pulsed Nd:YAG laser (355 nm). When sufficiently high power is used (> 50 uJ/pulse) and focused (~20 cm focal length lens), a second 225 nm photon can be used for the non-resonant ionization step. Otherwise, a third 320 nm laser was employed

generated by the doubled 640 nm output of a PDL dye laser (DCM dye) pumped by the second harmonic output of a Nd:YAG laser (532 nm). The reasons for employing a separate laser for the ionization step are discussed in later chapters.

The total ion signal as a function of probe wavelength yields the excitation spectrum of the NO ($A\ ^2\Sigma_{1/2}$) state, as shown in Figure 8. Also shown is the simulated spectrum performed with the LIFbase software.[13] Using the simulations, we can determine the origin of each transition and probe a desired quantum state of the NO fragment in the ion imaging experiment. During the image acquisition it is necessary to scan the probe wavelength over a small range (~0.005 nm) to account for Doppler shifting, as the fragments can be traveling with a recoil velocity (v) of up to 3000 m/s which leads to a shift ($\Delta\lambda$) in the initial 225 nm probe wavelength (λ_0) of about 0.0023 nm using the following equation.

$$\Delta\lambda = \lambda_0 \left(\frac{v}{c}\right) \tag{2.1}$$

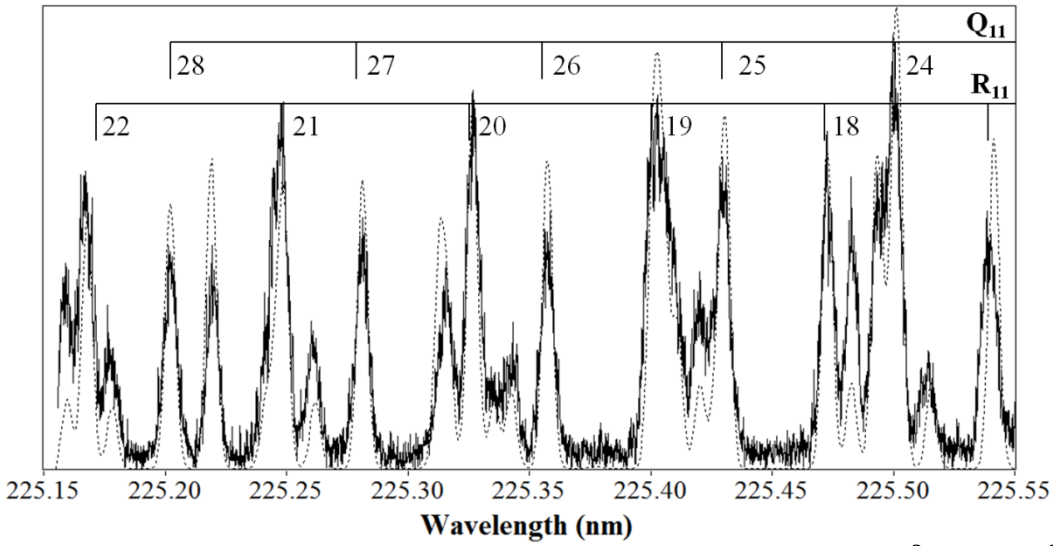

Figure 8: NO REMPI scane, 225.15-225.55 nm. REMPI ($NO^+ \leftarrow A\ ^2\Sigma_{1/2} \leftarrow X\ ^2\Pi_\Omega$) scan of NO (solid lines) along with simulated spectrum (dashed lines) assuming a Gaussian laser linewidth of 0.005 nm, and a NO rotational distribution of 1300 K. The combs indicate the probed NO ($X\ ^2\Pi_\Omega$, v = 0) rotational quantum number N, via the Q and R rotational branches. The other branch labels are omitted for clarity.

D. Ion time of flight

The NO fragments which are not ionized quickly fly out of the interaction area and are eventually evacuated from the chamber by the vacuum system. The sphere of NO^+ cations, however, is immediately accelerated toward the detector down the time of flight tube by a series of four ion optics. The optics focus the trajectory of each ion such that its radial displacement on the detector is only a function of its x-y velocity, not its initial position (as the molecular beam has a finite width).[9] Additionally, the optics serve the purpose of compressing or stretching the temporal profile of the NO^+ ion cloud as it flies toward the detector. If we wish to collect the signal from the whole Newton

Sphere (crushed imaging), we want to compress the temporal profile so that all of the ions hit the gated detector in a small time window, minimizing background ion counts and increasing signal to noise. However, it is sometimes beneficial to collect only the center slice of the Newton Sphere (DC slice imaging).[14] Slice imaging collects a direct velocity profile of the fragments, unlike crushed imaging where the velocity distribution must be obtained by mathematically reconstructing the crushed image (see Chapter 3).[15] The reconstruction algorithms are only valid when the image contains cylindrical symmetry about the image plane, and thus cannot be performed when laser polarizations that break thus symmetry are utilized. DC slicing is experimentally difficult, however, and creates uncertainties in the analyzed speed distribution due to finite cloud slicing. Therefore, we primarily use the crushed imaging technique except when it is necessary to use non-standard laser polarizations.

E. Ion detection

At the end of our time of flight tube lies a position sensitive ion detector, composed of a dual chevron configuration of 4 cm diameter MicroChannel Plates (MCP) in front of a fast phosphor screen (radiative lifetime of a few nanoseconds). When each ion in the Newton Sphere hits the front MCP plate (which is grounded) it begins a cascade of electrons through one of the microchannels. The number of electrons is amplified as the they are accelerated toward the positively charged back MCP and then onto the phosphor screen, which will illuminate when struck by the electrons. Gating the voltage on the back MCP allows the selective detection of certain ion masses (NO^+ m/z = 30), as it must be held above ~1800 kV for sufficient signal gain to occur.

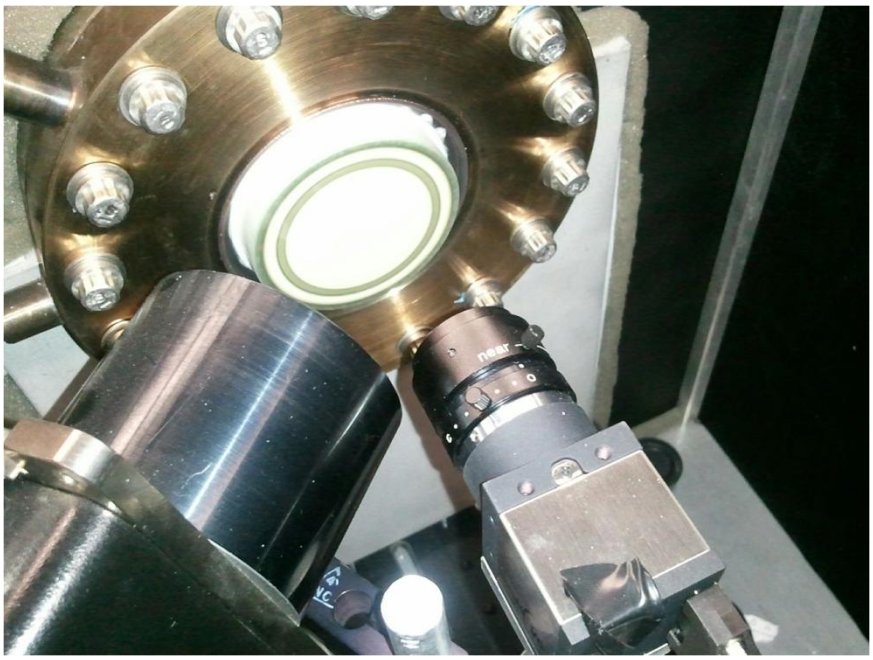

Figure 9: Photograph of the ion detection system. USB camera (right) and photomultiplier tube (left) pointed at the MCP/Phosphor screen detector.

F. Capturing the image

A photomultiplier tube collects the total time resolved signal on the phosphor screen, and a triggered USB camera takes photographs, capturing a snapshot of the position of all of the ions (**Figure 9**). A grayscale text or bitmap snapshot captured by our camera is represented as a simple two dimensional array of intensities. The resolution of each snapshot is 768×768, meaning the 2D-array is composed of 589,824 separate pixels. The glowing dot (100-1000 μm diameter) observed on the phosphor screen when an ion collides with the detector screen assembly is somewhat larger than the space encompassed by a single pixel on our camera frame (~70 μm). The true location of each ion striking the detector is therefore approximated by the "center of

mass" (center of pixel area weighted by intensity) of each dot of signal observed. Each snapshot captured by the camera is then converted to a binary image, where the pixel associated with the center of mass of each observed dot on the detector is assigned an intensity of 1, and all other pixels are given an intensity of 0. This binary image of each camera snapshot is added to the binary images of each previous snapshot to form a 768×768 unsigned 8-bit (the intensity of each pixel ranges from 0 to 256) accumulated image. This image is the final result of our experiment, and when accumulated for a sufficiently long period of time, represents the full 2D (sliced Image) or 3D (crushed Image) spatial distribution of a photofragment. Analysis of this image provides us with the correlated product distribution we require to decipher the dynamics of the photodissociation reaction.

CHAPTER III

THE IMAGE

"The Image is one thing and the human being is another. It's very hard to live up to an image…"

-Elvis Presley

At the end of all our trials and labors, the experiment provides us with just one thing: The Image. The Image contains the accumulated information of several thousand photochemical reactions on a single two-dimensional landscape. The Image is a map of the journey of each photofragment from the time of its creation to the time of its detection. Learning to read this map, however, is a journey in of itself. In this section, we will first detail how to process an ion image and extract the radial and angular signal distributions. Second, we will learn how to meaningfully interpret these distributions, and determine the correlated internal energy distribution and stereochemistry of the product fragments.

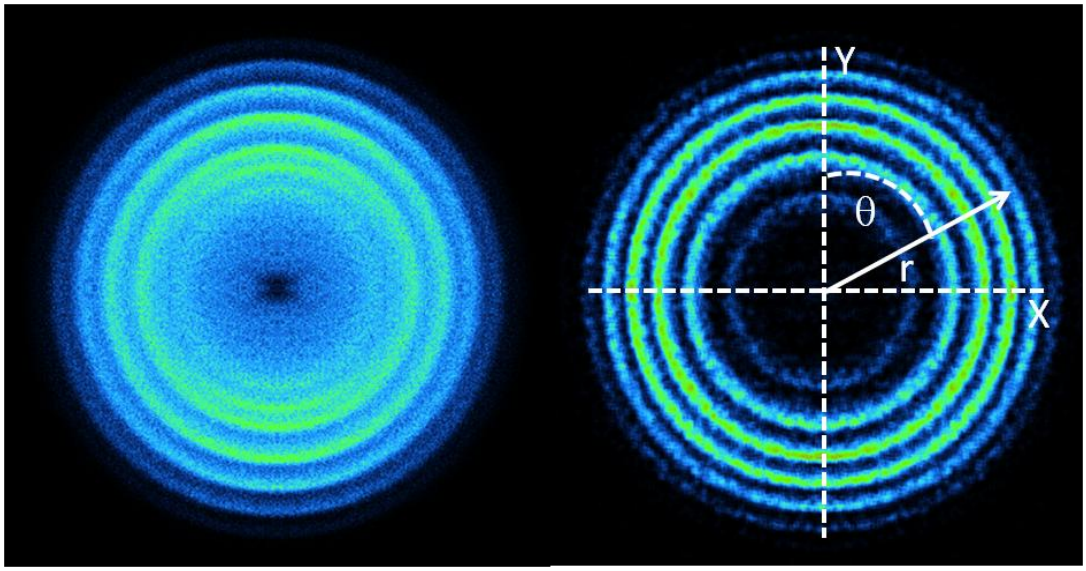

Figure 10: Symmetrized crushed (left) and DC sliced (right) images of NO ($^2\Pi_{3/2}$; v=0; j=6.5) obtained from NO_3 photolysis with a 588 nm photon.

A. Processing the image

Figure 10 shows an ion image (obtained via both the crushed and DC slice imaging methods) of the NO($^2\Pi_{3/2}$; v=0; j=6.5) fragment resulting from NO_3 photolysis. The raw Image is represented by an inconvenient and arbitrary set of Cartesian coordinates: x-pixel and y-pixel. Radial coordinates, r and θ, represent a much more physical interpretation of the dynamics, as r is linearly proportional to the speed of the detected fragment. Therefore the first step in our journey to interpret the Image begins with conversion of $I(x,y)$ to $I(r,\theta)$.

This conversion is straightforward, where

$$r = \sqrt{(x - x_{center})^2 (y - y_{center})^2} \tag{3.1}$$

$$\theta = arctan\left(\frac{x-x_{center}}{y-y_{center}}\right) \quad (3.2)$$

These equations require accurate determination of the Image origin (x_{center}, y_{center}), which can be non-trivial. A convenient method for determining this origin is fourfold symmetrization, where the horizontal and vertical reflections of the Image around the best guess of (x_{center}, y_{center}) are merged. The (x_{center}, y_{center}) values can then be adjusted until the reflections overlap each other exactly, as the four image quadrants must be identical (when imaging an unoriented molecular beam with linearly polarized pump light). An example of this is shown in Figure 11. The resulting symmetrized Image may be analyzed in place of the raw Image to achieve an enhanced signal to noise distribution for each quadrant.

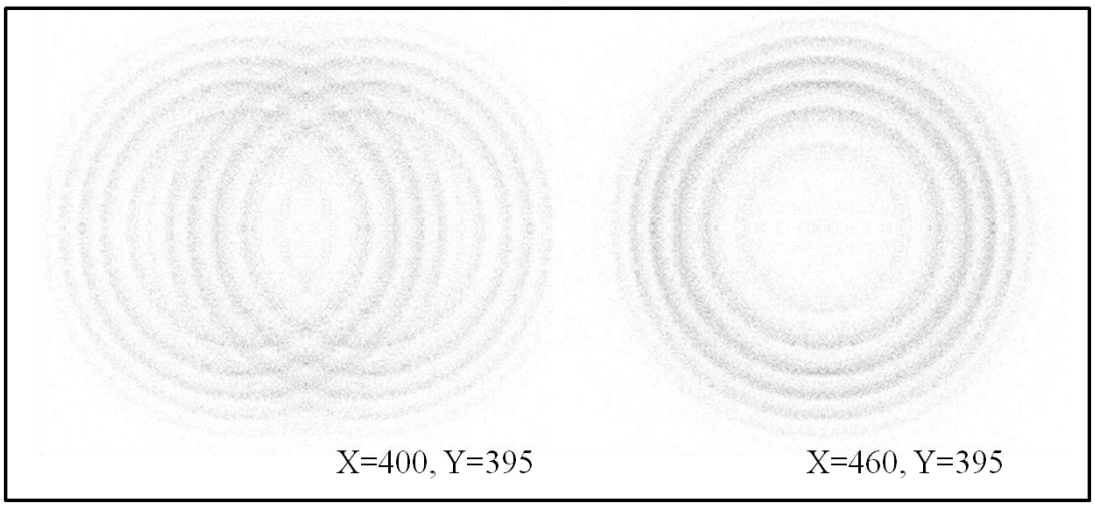

Figure 11: Example of the symmetrization methond of image centering. Both images are fourfold symmetrized around a different (x,y) origin. The symmetrization allows for easy visual affirmation of the image center.

Equations 3.1 and 3.2 will provide the true photofragment $I(r,\theta)$ distribution when applied to a raw sliced ion image (although adjustments may be required to account for finite ion cloud slicing) (Figure 12). A crushed ion image, however, requires further processing since it represents a 3D fragment distribution projected onto a 2D plane. The apparent r is therefore not representative of the fragment's true velocity due to the unknown z dimension of the velocity vector of each ion. However, if the signal distribution is cylindrically symmetric around an axis within the image plane, the proper 2D signal distribution can be mathematically reconstructed.

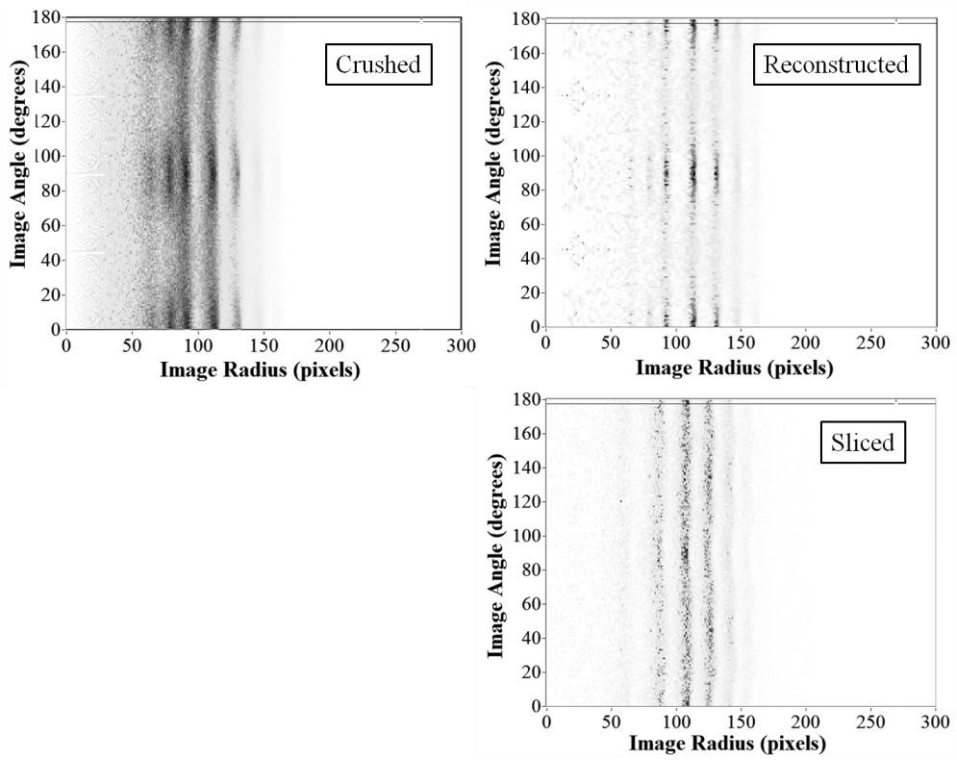

Figure 12: $I(r,\theta)$ distributions of a crushed, reconstructed (using the POP algorithm), and DC sliced ion image. The anisotropy observed in the crushed image is due to an incomplete Doppler scan, and does not illustrate a difference between crushed and sliced imaging.

Many methods exist for remapping the crushed 3D $I(r,\theta)$ distribution into a proper 2D $I(r,\theta)$ distribution, but we have chosen the Polar Onion Peeling method (POP) to integrate into our analysis software.[15] The POP algorithm is quite simple, and begins with the correct assumption that the distribution at the outer edge of the image, $I(r_{max},\theta)$, is equivalent to the true 2D distribution, since the *z* component of the velocity vector must be zero when the *x* and *y* components are at their maximum. Assuming the image is cylindrically symmetric, the signal contribution of the true outer r_{max} shell of the image is known for all apparent *r* values, and can then be subtracted from the rest of the image. This results in a new image where the outer layer of the crushed sphere has been "peeled" away. The same procedure may then be repeated until every layer has been peeled away and the entire 2D $I(r,\theta)$ distribution is known. The POP algorithm, or any other image reconstruction technique, is only valid when the image possesses cylindrical symmetry about the imaging plane. This is only true if both the pump and probe lasers are linearly polarized within the imaging plane. For some measurements, such as the determination of certain dynamical vector correlations, it is necessary to use symmetry breaking laser polarizations and thus crushed imaging is not feasible, and sliced imaging should be used instead.[16]

Once the $I(r,\theta)$ distribution has been obtained, the radial distribution can simply be obtained by integrating over all θ values in the following way:

$$I(r) = \int I(r,\theta) \cdot r \, d\theta \tag{3.3}$$

The *r* factor is included to account for the signal which has been sliced away. The true signal distribution is spread across a 2D spherical surface, not a 1D circumference and thus an additional factor of *r* is required.

Once the radial distribution of the signal has been extracted from the image, the radial coordinate (pixels) must be converted to fragment speed v_{NO} (m/s) by multiplying by a linear conversion factor, γ_p. Figure 13 shows the derived $I(v_{NO})$ distributions from the images in Figure 10. The radial distribution from a sliced image must be adjusted to account for finite slicing by the detector. The method for obtaining the γ_p factor, which is dependent on the voltages of the ion optics and the mass of the detected fragment, will be discussed later in this chapter.

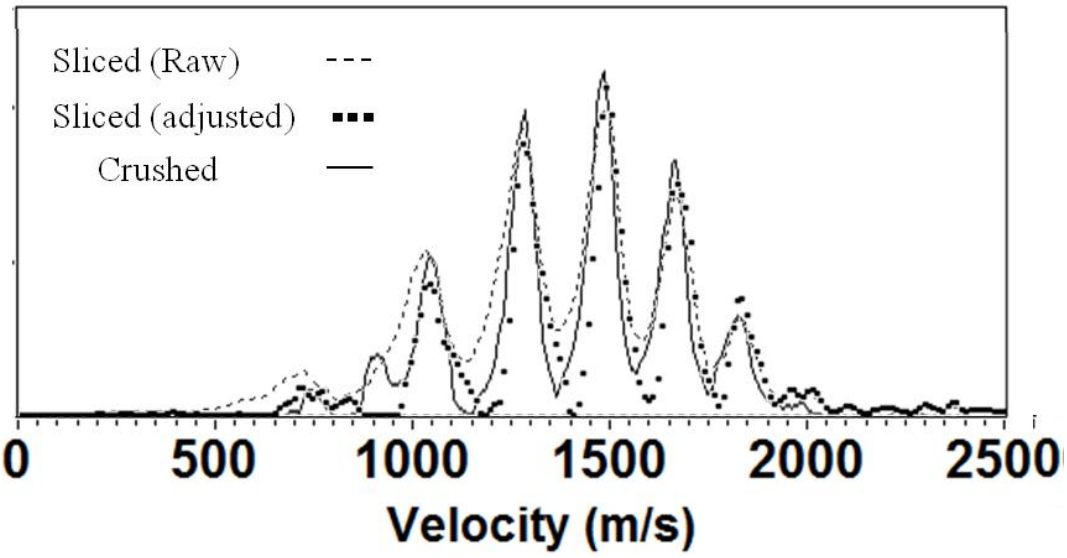

Figure 13: Crushed and sliced velocity distributions of NO($^2\Pi_{3/2}$; v=0; j=6.5) originating from NO_3 photolysis at 588 nm. Slice images always have a finite slice width, here assumed to be 45 pixels, which can later be accounted for.

In addition to speed, the radial distribution can be expressed as a function of total translational energy, E_T, which is related to v_{NO} in the following way:

$$E_T = \frac{1}{2} m_1 \left(\frac{m_1}{m_2} + 1\right) {v_{NO}}^2 \quad (3.4)$$

This is derived from conservation of momentum,

$$m_{NO} v_{NO} = m_{O_2} v_{O_2} \quad (3.5)$$

and the expression:

$$E_T = \frac{1}{2} \mu v_R^2 \quad (3.6)$$

Where v_R is the relative velocity of the fragments:

$$v_R = v_{NO} + v_{O_2} \quad (3.7)$$

Additionally, since the conversion from speed to translational energy is nonlinear, a Jacobian factor of $\frac{1}{v_{NO}}$ is required when converting $I(v_{NO})$ to $I(E_T)$:[17]

$$I(E_T) = \frac{1}{v_{NO}} I(v_{NO}) \quad (3.8)$$

B. Interpreting the speed distribution

The speed distribution leads us to a complete understanding of the energetics of single photochemical event. More specifically, it allows us to find the correlations between the internal energy of both product fragments. The acquisition of correlated product distributions is what allows us to decipher the photochemical dynamics, and what makes velocity map ion imaging superior to simple spectroscopic measurements of total product internal energy distributions. The total available energy for any physical process must be conserved, and the same is of course true for photodissociation. Any "leftover" energy from a photodissociation event that does not go into the internal

energy of the fragments goes into their translational energy, E_T. Therefore by measuring both the internal energy and the recoil speed of a fragment, the internal energy of the coincident cofragment is revealed as well. The internal energy of a molecule can be broken down into three components: the electronic energy E_{elec}, the vibrational energy E_{vib}, and the rotational energy E_{rot}. The manner in which the energy is distributed among these components in both photoproducts provides insight into the dynamics of the reaction. Here we show how to determine the correlated internal energy distribution of the O_2 fragment from the speed distribution shown in **Figure 13**, obtained by imaging the NO($^2\Pi_{3/2}$; v=0; j=6.5) fragment resulting from 588 nm photolysis of NO_3.

Table 1: Dissociation energies of relevant reactions

Reaction	ΔE_{rxn} (kcal/mol)
$NO_3 \rightarrow NO + O_2$	2.6[18]
$NO_3 \rightarrow NO_2 + O$	48.83[18]
$NO_2 \rightarrow NO + O$	71.71[19]

Table 2: Spectroscopic constants of relevant molecules and reactions

(cm^{-1})	T_e	ω_e	$\omega_e\chi_e$	B_e	D_e	α_e
$NO(^2\Pi_{3/2})$[20]	-	1904.20	14.075	1.6720	$5.4E^{-7}$	0.0171
$NO(^2\Pi_{1/2})$[20]	119.82	1904.04	14.100	1.7202	$1.023E^{-5}$	0.0182
$O_2(^3\Sigma^-_g)$ [21]	-	1580.19	11.980	1.4377	$4.839E^{-6}$	0.0159
$O_2(^1\Delta_g)$[22]	7918.1	1483.50	12.000	1.4264	$4.86E^{-6}$	0.182
$O_2(^1\Sigma^+_g)$[23]	13195.1	1432.77	14.000	1.4004	$5.351E^{-6}$	0.0171

After an NO_3 molecule of a particular energy $E_{NO_3}(E_{elec}, v_{1-6}, J)$ absorbs a photon of light with energy $h\frac{c}{\lambda}$ and dissociates, conservation of energy dictates that the energy that was not consumed by the $NO_3 \rightarrow NO + O_2$ reaction (ΔE_{rxn}) is imparted to the fragments as either internal energy (E_{elec}, v, j) or translational energy, E_T. The total translational energy available of the photofragments is thus given by the expression:

$$E_T = h\frac{c}{\lambda} + E_{NO_3}(E_{elec}, v_{1-6}, J) - \Delta E_{rxn}$$
$$-E_{NO}(E_{elec}, v, j) - E_{O_2}(E_{elec}, v, j) \quad (3.9)$$

The photon energy $h\frac{c}{\lambda}$ can be easily calculated (588 nm = 48.62 kcal/mol), and ΔE_{rxn} is given in **Table 1** (2.6 kcal/mol). The spectroscopic constants required to calculate the internal energy of the fragments from the following equations are given in **Table 2**:

$$E_{vib} = \omega_e\left(v + \tfrac{1}{2}\right) - \omega_e\chi_e\left(v + \tfrac{1}{2}\right)^2 \quad (3.10)$$

$$E_{rot} = B_eJ(J+1) - D_eJ^2(J+1)^2 - \alpha_eJ(J+1)\left(v + \tfrac{1}{2}\right) \quad (3.11)$$

Using these equations, NO($^2\Pi_{3/2}$; v=0; j=6.5) has an internal energy of 0.61 kcal/mol. The internal energy distribution of the parent NO_3 molecule is quite cold after expansive cooling in the vacuum, and was found to be negligible (Chapter V.A) and thus assumed to be ~0 kcal/mol in our energetics calculations. Because every other variable in Equation 3.9 is accounted for (the sum of which we shall call E_{avail}), the experimentally obtained translational energy distribution E_T the internal energy distribution of the O_2 fragment can now be determined:

$$I(E_T) = E_{avail} - I\left(E_{O_2}\right) \tag{3.12}$$

Figure 14 shows the $I(E_T)$ obtained from the NO($^2\Pi_{3/2}$; v=0; j=6.5) ion image, along with a forward convolution simulation of the $I\left(E_{O_2}\right)$ distribution. The comb above the distribution shows the maximum E_T for the formation of a particular vibrational state of the O_2 fragment in its ground electronic state, O_2 ($^3\Sigma_g$, v). It is clear that each peak in the $I(E_T)$ spectrum arises from a different vibrational quantum number of O_2, which arise to the left of the comb due to the distribution of O_2 rotational states which does not peat at j=0.

The O_2 rotational distribution, $I_{O_2}(j)$, has been fit by a Boltzmann distribution at 300 K in the simulation, although there is no reason to assume this distribution must be thermal.

$$I_{O_2}(j) = (2j+1)e^{-E_{rot}/kT} \tag{3.13}$$

The rotational energy spacing is too small to be observed in $I(E_T)$, but presents itself as the a broadening of the peaks associated with the O_2 vibrations. The forward convolution

fit of the $I(E_{O_2})$ function was generated by placing weighted Gaussian functions, representing the instrument function, at each possible $E_{O_2}(E_{elec}, v, j)$ state. The instrument was previously determined to give a velocity resolution of ~5% $\left(100 \times \frac{\Delta v}{v}\right)$, resulting in Gaussian widths of $(\Delta v = 0.05 \times v_{NO})$.

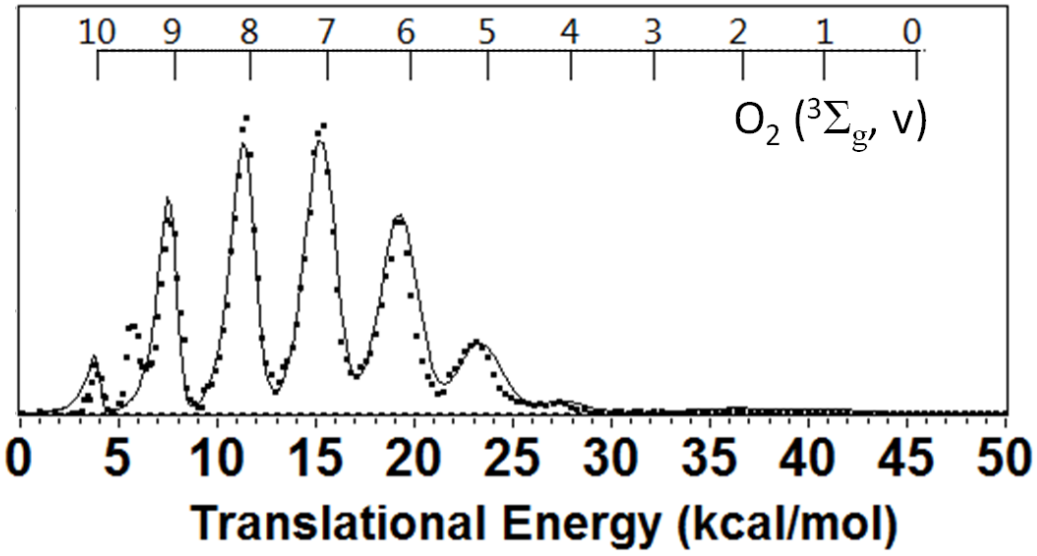

Figure 14: NO($^2\Pi_{3/2}$; v=0; j=6.5) translational energy distribution obtained from NO_3 photodissociation at 588 nm (dots). Forward convolution simulation of the velocity distribution assuming an O_2 rotational distribution of 300K. The O_2 vibrational state corresponding to each peak is labeled by the comb above the graph.

C. Speed to pixel ratio

This section provides an example of how to determine the factor γ_p which converts the radial displacement in the image (measured in camera pixels) to speed (m/s). This factor is dependent on both the ion optics voltages and the mass to charge ratio of the detected ion. High voltages and smaller mass fragments lead to a shorter time of flight which leads to a smaller radial displacement on the detector. For our experiments, this means determining the speed to pixel ratio for NO^+ ions using ion optic voltages of 3000 V, 2658 V, and 2310 V (for crushed imaging).

The background signal from $NO_2 \rightarrow NO + O$ photodissociation at our probe laser wavelength (~225 nm) provides a convenient reference point for calculating the speed to pixel ratio. Because the state-selected NO fragment is formed in coincidence with an atomic partner (whose internal energy is entirely electronic), it should recoil with a discrete and predictable velocity.

Single photon dissociation of NO_2 can produce either ground state oxygen fragments, $O(^3P)$, or excited state $O(^1D)$ (15889 cm^{-1}). Using the constants in **Table 1** and **Table 2** and the methods discussed in the previous section, we calculate that NO_2 dissociates at 226.7 nm into $NO(^2\Pi_{3/2}; v=0; N=6)$ and $O(^3P)$ which results in an NO fragment with a recoil velocity of ~2285 m/s. Additionally, if $O(^1D)$ is formed the NO fragment recoils with a velocity of ~905 m/s.

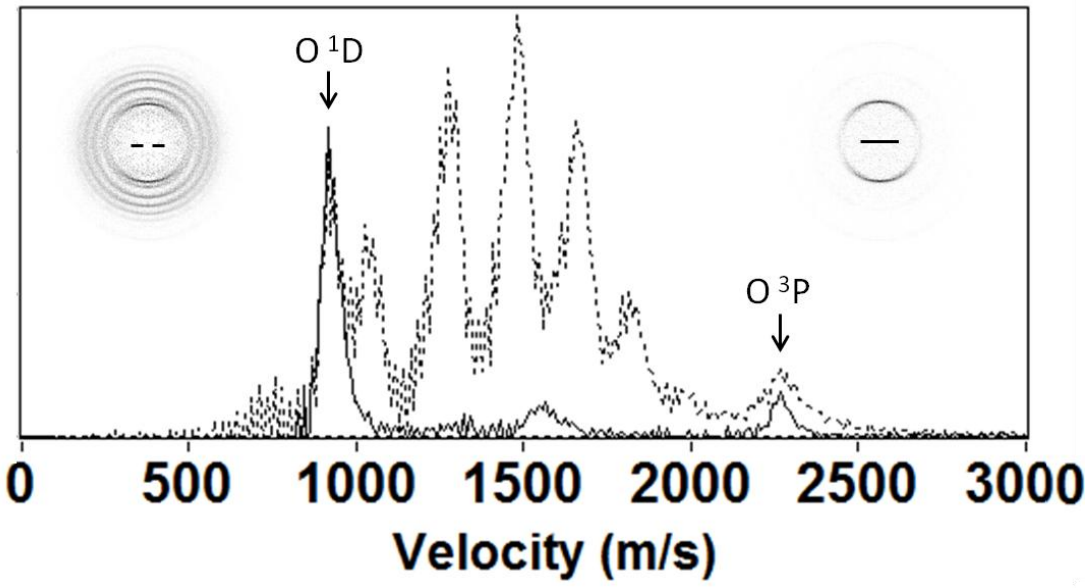

Figure 15: Velocity distribution of background NO_2 signal as a reference point for speed to pixel calibration. Observed NO ($^2\Pi_{3/2}$; v=0; N=6) velocity distribution with only the 226.7 nm probe laser beam active (solid line) and when the 588 nm pump laser is turned on (dashed line). The background probe signal arises from NO_2 → NO + O photodissociation at 226.7 nm.

Figure 15 shows the velocity distribution obtained from NO_2 photodissociation at 226.7 nm. The sharp and intense inner ring is due to NO_2 → NO + O(^{1}D), while the smaller outer ring arises from NO_2 → NO + O(^{3}P). Since we have already calculated the necessary velocities of these peaks, we determine that the speed to pixel ratio γ_p of 11.27 m/s/pixel.

D. Characterizing the angular distribution

Although the energetic information obtained from the radial distribution is often the primary result of ion imaging, careful analysis of the angular distribution also provides valuable insight into the reaction dynamics. The angular distribution provides insight into the underlying dynamics of the reaction revealing the excited state symmetry

and couplings, dissociation time-scales, and details about forces and torques between the separating fragments. Because the angular distribution is a vector measurement instead of a scalar measurement, it provides directional information such as the orientation and relative motion of the molecule and its fragments during the dissociation.

Prior to excitation, the molecules are not aligned in the laboratory reference frame. Where does this anisotropic signal, then, originate? The origin of the angular distribution of an ion image comes from the interaction of polarized light with the measured molecules. Light can be thought of as an electromagnetic wave propagating through space. The light emitted by our lasers is linearly polarized, meaning the electric field of the light oscillates back and forth along one axis at some frequency, perpendicular to the direction the photon is traveling. It is this electric (or in some cases, magnetic) field which is capable of interacting with atoms and molecules.

In order for the electric field of light $\boldsymbol{E}$ to affect a molecule, that molecule must have an electric dipole to interact with. The dipole which interacts with the electric field for a given process is called the transition dipole moment $\boldsymbol{\mu}$. The probability of the molecule absorbing and being affected by the light is dependent on the square of the projection of $\boldsymbol{E}$ onto $\boldsymbol{\mu}$ ($P = |E \cdot \mu|^2$).[24] That is, if a photon approaches the molecule at an angle such that $\boldsymbol{E}$ and $\boldsymbol{\mu}$ are perpendicular to each other, the light cannot interact with the dipole moment and thus will not be absorbed. If $\boldsymbol{E}$ is parallel to $\boldsymbol{\mu}$, the light interacts with the full dipole moment of the transition and has the greatest chance of being absorbed. The dot product of two vectors can be written in terms of the angle between those vectors, leading to:

$$|E \cdot \mu|^2 = |E|^2|\mu|^2 \cos^2\theta_{E\mu} \quad (3.14)$$

The laser polarization therefore acts as a way of "aligning" the molecules in the lab frame, since certain orientations are preferentially detected. This includes both the parent molecule (**μ_{par}**) which is aligned via the pump laser polarization, and the fragment molecule (**μ_{frag}**) which is aligned via the probe laser polarization. Each absorption of a photon in the experiment can result in an additional $\cos^2\theta$ term in the signal distribution.[16] For our experiments, we utilize one photon dissociation and one (resonant) photon detection and thus we can at most expect a $\cos^4\theta$ distribution. Two photon dissociation and a one resonant photon probe however, could result in a $\cos^6\theta$ signal distribution.

Angular distributions are typically expressed as an expansion of Legendre polynomials instead of $\cos^n\theta$ terms, as the β_n^{FG} coefficients of $P_n(\cos\theta)$ terms are more physically interpretable.[17] The full equation of the angular image intensity when pumped and probed with linearly polarized light (which only allows even n terms) therefore becomes:

$$I(\theta) = 1 + \beta_2^{FG} P_2(\cos\theta) + \beta_4^{FG} P_4(\cos\theta) + \cdots \beta_n^{FG} P_n(\cos\theta) \quad (3.15)$$

Where *F* and *G* stand for the lab-frame polarization of the pump and probe lasers respectively, as different laser polarizations will result in a different $I(\theta)$ distribution. A vertical arrow (↕) indicates that the laser is polarized along the image plane, while an out of plane arrow (⊙) indicates the laser is polarized normal to the image plane. Lasers

polarized orthogonal to the ion image plane will not contribute a $\cos^2\theta$ term to the signal distribution, and thus $\beta_n^{\odot\odot}$ will always lead to an isotropic image.

E. Extracting the β_n coefficients: least squares regression

The β_n coefficients, which we shall call the anisotropy parameters, must be obtained by fitting the angular signal distribution to Equation (3.15). The anisotropy parameters are often dependent on fragment speed, and thus must be calculated as a function of image radius. The most straightforward way of accomplishing this fit is a series of simple least squares regressions of the total angular signal with a certain radial range.[25]

Equation (3.15) can be expressed at a particular image radius *r* as the matrix equation:

$$\begin{pmatrix} I_r(0) \\ I_r(\dots) \\ I_r(180) \end{pmatrix} = \begin{pmatrix} 1 & P_2(\cos 0) & P_4(\cos 0) \\ 1 & P_2(\cos \dots) & P_4(\cos \dots) \\ 1 & P_2(\cos 180) & P_4(\cos 180) \end{pmatrix} \begin{pmatrix} c_0 \\ c_2 \\ c_4 \end{pmatrix} + \begin{pmatrix} \epsilon_0 \\ \epsilon_{\dots} \\ \epsilon_{180} \end{pmatrix} \tag{3.16}$$

where $\beta_n = \frac{c_n}{c_0}$ and ϵ_n represents the error. Or more simply:

$$[I_r]_\theta = [P]_{\theta,n}[c]_n + [\epsilon]_\theta \tag{3.17}$$

To determine the least squares fit for the c_n coefficients, we want to minimize the error which can be rewritten as:

$$[\epsilon]_\theta = [I_r]_\theta - [P]_{\theta,n}[c]_n \tag{3.18}$$

The minimum error occurs when the error vector is orthogonal to the $[P]_{\theta,n}$ matrix, that is when:

$$[\epsilon]_\theta{}^T \cdot [P]_{\theta,n} = 0 \tag{3.19}$$

Substituting Equation 3.19 into Equation 3.18 and solving for $[c]_n$, we arrive at:

$$[c]_n = \left([P]_{\theta,n}{}^T [P]_{\theta,n}\right)^{-1} [P]_{\theta,n}{}^T [I_r]_\theta \tag{3.20}$$

Once the optimal β_{n} parameters are determined from the $[c]_n$ matrix, it is also trivial to solve for the error matrix $[\epsilon]_\theta$, and the total σ^2 variance of the fit is simply:

$$\sigma^2 = \frac{\sum_{\theta=0}^{180}([\epsilon]_\theta)^2}{180} \tag{3.21}$$

The error limits of each β_{n} coefficient are sometimes desired as well as the total variance. This can be found by creating a σ^2 surface of constant error equal to twice the value of the best fit σ^2, in c_{n} space. The error in c_{n} is then obtained by averaging the difference between the c_{n} values of points on the σ^2 surface and the best fit c_{n} values. An example of a least squares fit with error limits is shown in **Figure 16**.

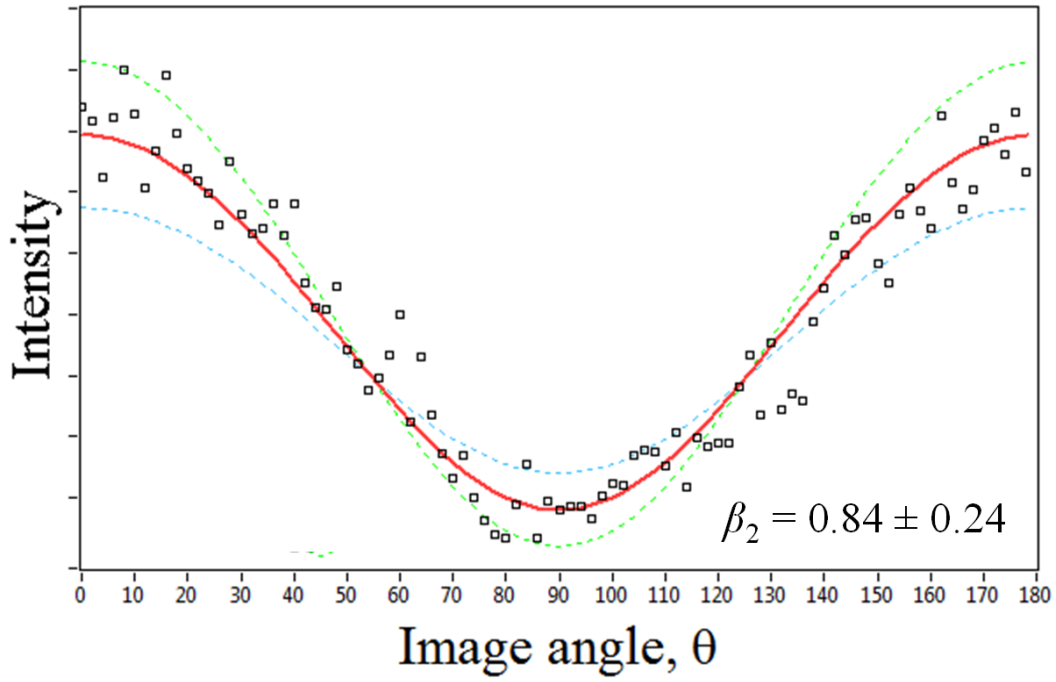

Figure 16: Example ion image angular distribution fit using the linear least squares method. The open squares represent the experimental data, and the best least squares fit is shown as the solid line. The error range is shown by the dashed lines.

F. Fourier series: the more elegant solution

A more computationally elegant determination of the anisotropy parameters comes when the angular intensity at a particular radius is expressed as the following Fourier series:[26]

$$I_r(\theta) = a + b\cos(2\theta) + c\cos(4\theta) \tag{3.22}$$

This is a convenient representation, because the a, b, and c parameters can be determined without performing a fitting algorithm:

$$\int_0^{2\pi} I_r(\theta) \cdot 1 \, d\theta = \int_0^{2\pi} \big(a + b\cos(2\theta) + c\cos(4\theta)\big) \, d\theta = a \tag{3.23}$$

$$\int_0^{2\pi} I_r(\theta) \cdot \cos(2\theta)\, d\theta =$$

$$\int_0^{2\pi} \big(a + b\cos(2\theta) + c\cos(4\theta)\big) \cdot \cos(2\theta)\, d\theta = \frac{b}{\pi} \tag{3.24}$$

$$\int_0^{2\pi} I_r(\theta) \cdot \cos(4\theta)\, d\theta =$$

$$\int_0^{2\pi} \big(a + b\cos(2\theta) + c\cos(4\theta)\big) \cdot \cos(4\theta)\, d\theta = \frac{c}{\pi} \tag{3.25}$$

The integrals can be calculated as Riemann sums, which can be computationally executed during the I(x, y) → I(r, θ) conversion step. The a, b, and c coefficients can later be related to the β_{n} coefficients by derived algabraeic expressions:

$$\beta_2 = \frac{10\left(16\frac{\mathrm{c}}{\pi \mathrm{a}} - 28\frac{\mathrm{b}}{\pi \mathrm{a}}\right)}{7\left(\frac{\mathrm{c}}{\pi \mathrm{a}} + 5\frac{\mathrm{b}}{\pi \mathrm{a}} - 15\right)},\ \beta_4 = -\frac{384\frac{\mathrm{c}}{\pi \mathrm{a}}}{7\left(\frac{\mathrm{c}}{\pi \mathrm{a}} + 5\frac{\mathrm{b}}{\pi \mathrm{a}} - 15\right)} \tag{3.25}$$

CHAPTER IV

THE VECTOR CORRELATIONS

"When you can measure what you are talking about and express it in numbers, you know something about it."

-Lord Kelvin

The angular distribution of the ion image is a result of the stereodynamics of the photodissociation, the orientation and movement of the molecules in space. The stereodynamics of a unimolecular reaction can largely be described by three vectors: the spatial orientation of the parent molecule (conveniently described in optical experiments by the transition dipole moment $\boldsymbol{\mu}_{\mathbf{par}}$), the relative recoil velocity **v** of the departing photofragments, and the angular momentum vector(s) **j** of the photoproducts (which can be optically detected by $\boldsymbol{\mu}_{\mathbf{frag}}$).[24, 27-28] The inherent measurement of the fragment velocity vector **v** is the primary benefit of velocity map ion imaging. Correlations between $\boldsymbol{\mu}_{\mathbf{par}}$, **v**, and **j** can be extracted from the angular distribution of the image vectors provide key dynamical information.

Several formalisms have been developed to describe the stereodynamics of the photofragments.[29-32] However, the bipolar moment $\beta_Q^K(k_1k_2)$ parameters of Dixon have the most straightforward physical interpretation for semi-classical dynamics of direct photodissociation.[33] Single photon probing of one-photon photodissociation of isotropic samples gives Doppler or ion imaging data sensitive to five low-order bipolar moments: the **μ-v** correlation $\beta_0^2(20)$, the **v-j** correlation $\beta_0^0(22)$, the **μ-j** correlation

$\beta_0^2(02)$, the quadratic **μ-v-j** correlation $\beta_0^2(22)$, and the quartic **μ-v-j** correlation $\beta_0^2(42)$.[34] These bipolar moments are the expansion coefficients in a bipolar harmonic expansion of the spatial probability distribution of **v** and **j** in the frame of $\boldsymbol{\mu}_{\mathbf{par}}$, which is in turn aligned in the space-fixed frame of the photolysis polarization.[33] Conveniently, the $\beta_0^2(20)$, $\beta_0^0(22)$, and $\beta_0^2(02)$ parameters (the **μ-v**, **v-j**, and **μ-j** correlations respectively) can be interpreted semi-classically as an expectation value of the 2nd Legendre polynomial: $\langle P_2(cos\theta)\rangle$, where θ is the angle between the two relevant vectors, giving each parameter limiting values ranging from -0.5 (if the vectors are orthogonal) to 1 (if the vectors are parallel). Here we briefly describe the meaning and interpretation of each of the five bipolar moment parameters.

$\boldsymbol{\beta_0^2(20)}$ [$\boldsymbol{\mu}_{\mathbf{par}}$-v]: $\boldsymbol{\mu}_{\mathbf{par}}$ describes the molecular frame orientation on the parent molecule. $\boldsymbol{\mu}_{\mathbf{par}}$ is dependent on the optical transition of the pump, but will be either parallel (symmetry conserving transition) or perpendicular (symmetry changing transition) to the primary symmetry axis of the molecule. Ion imaging can therefore be used to determine the symmetry of a particular excited state, based on the observed image anisotropy arising from $\boldsymbol{\mu}_{\mathbf{par}}$**-v** correlations.[17] Additionally, the $\boldsymbol{\mu}_{\mathbf{par}}$**-v** correlation describes what direction the fragments are kicked out from the molecule parent molecule. For instance, as shown in Figure 17, a $\boldsymbol{\mu}_{\mathbf{par}}\|\mathbf{v}$ correlation would describe NO fragments recoiling inside the NO_3 plane, while a $\boldsymbol{\mu}_{\mathbf{par}}\perp\mathbf{v}$ correlation describes NO fragments recoiling out of the NO_3 plane.[35] It is important to note that although a $\boldsymbol{\mu}_{\mathbf{par}}$**-v** correlation may be present in the molecular frame, it may not be observable in the laboratory frame if the

dissociation lifetime is long as the molecular orientation may rotate considerably in the lab frame prior to dissociation.

$\boldsymbol{\beta_0^0(22)}$ **[v-j]:** **j** describes the angular momentum axis of the fragment molecule. The image anisotropy due to **j** correlations arises from the overlap between the electric field of the probe laser and $\boldsymbol{\mu_{frag}}$. The relationship between $\boldsymbol{\mu_{frag}}$ and **j** is dependent on the probe transition. Classically, $\boldsymbol{\mu_{frag}}$ of an R or P branch transition ($\Delta J \pm 1$) lies in the molecular plane of rotation ($\boldsymbol{\mu_{frag} \perp j}$), since the electric field from the photon must act upon the rotational plane to alter the angular momentum.[33] For a Q branch transition ($\Delta J = 0$), $\boldsymbol{\mu_{frag}}$ is orthogonal to the rotational plane ($\boldsymbol{\mu_{frag} \| j}$). The correlation between **v** and **j** provides an intuitive picture of the fragment motion as it is ejected from the parent molecule, whether the fragment is "helicoptering" (**v||j**) or "cartwheeling" (**v⊥j)** away (Figure 17).[10] The **v-j** correlation is derived from the forces and torques in the exit channel, and thus is independent of the parent molecule lifetime, unlike the other vector correlations. The implied forces and torques resulting from the measurement of this correlation provides a potent clue about the dissociation dynamics.

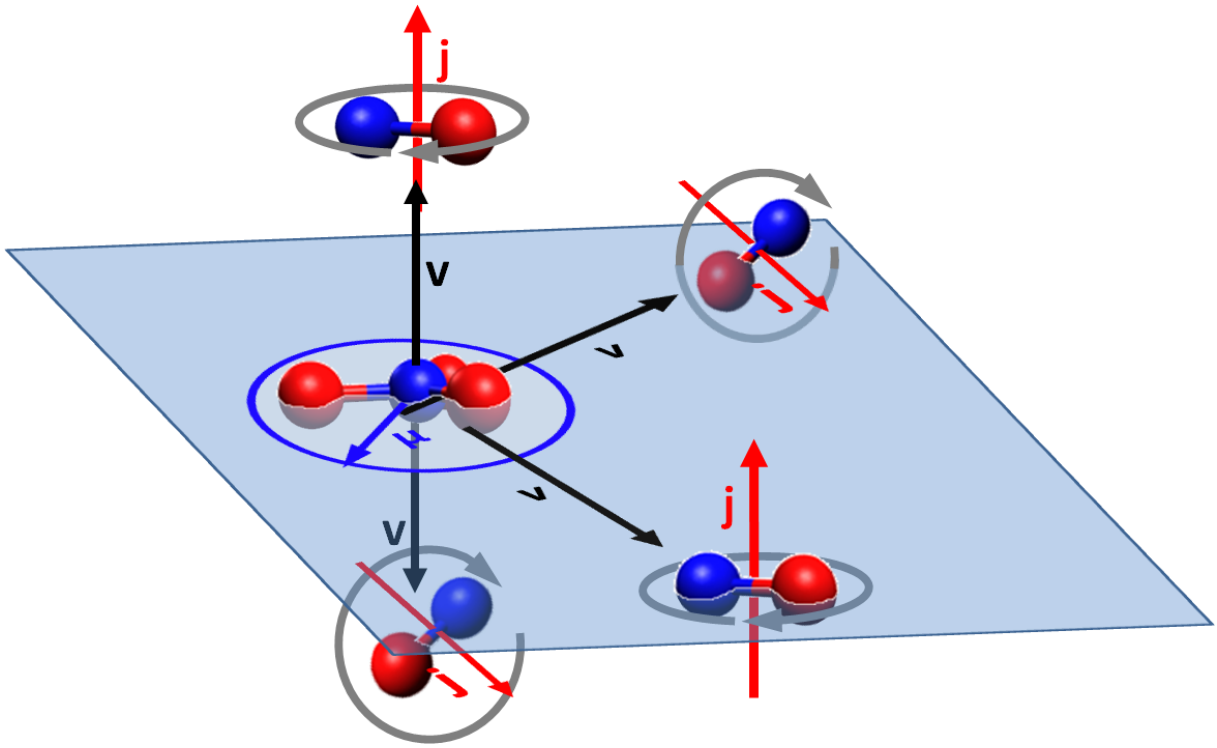

Figure 17: Schematic diagram of limiting vector correlation cases. Example of limiting vector correlation cases for NO_3 photodissociation via the B ← X transition: ($\mu_{par}\perp v \| j$), ($\mu_{par} \| v \perp j$), ($\mu_{par} \| v \| j$), and ($\mu_{par}\perp v \perp j$).

$\beta_0^2(02)$ [μ_{par}-j]: The **μ_{par}-j** correlation describes the relative spatial orientations of the parent molecule and the fragment rotational plane, independent of what direction the fragment is actually ejected. Because the **μ_{par}-j** correlation is independent of **v**, it can thus be measured through simple pump-probe LIF experiments as well as by velocity map ion imaging. The correlation is derived from the total observed signal when the pump and probe laser polarizations are parallel ($I_\parallel$) and perpendicular ($I_\perp$) to each other by the following formula:[33]

$$\beta_0^2(02) = \frac{5}{2h^{(2)}}\left(\frac{I_\parallel - I_\perp}{I_\parallel + 2I_\perp}\right) \tag{4.1}$$

$\boldsymbol{\beta_0^2(22)}$ **[μ_{par}-v-j]:** Typically the actual correlations between the vectors are not completely independent. As an example, when the NO fragment is ejected out of the plane of the molecule it may be helicoptoring (**$\mu_{par}\perp$v$\perp$j**), but when the NO fragment is ejected within the plane it could be frisbeeing instead (**μ_{par}||v||j**). This dependence between the three vectors is described by the so-called "triple vector" **μ_{par}-v-j** correlation.

$\boldsymbol{\beta_0^2(42)}$ **[quartic μ_{par}-v-j]:** In the high-j semi-classical limit is assumed, $\beta_0^2(42)$ is not an independent parameter and is given instead by:[34]

$$\beta_0^2(42) = \frac{7}{12}\beta_0^2(02) - \frac{5}{12}\beta_0^2(22) \tag{4.2}$$

effectively reducing the number of independent vector correlation parameters to four. Deviations from this relationship imply significant quantum interference effects. In this case, the bipolar moments begin to lose their semi-classical interpretation and it is more instructive to use a different set of parameters to describe the vector correlations. In the case of high **j** photofragments produced from direct photodissociation near the axial recoil limit, coherent alignment effects have been shown to vanish.[34] The contribution of coherence effects to the angular momentum alignment (probed with linearly polarized light) of the fragments decreases with a 1/j dependence, so the high-j limit is appropriate when detecting fragments with roughly j >10 where these effects can be maximally responsible for only a few percent of the total **j** polarization.

In typical experiments, the β_n coefficients will represent convolution of the vector correlations described above, and a method must be devised to separate the contribution of each correlation.

A. Analytical expressions for vector correlation determination

All of the vector correlations cannot be derived from a single ion image. Some of the angular distribution is due to the pump laser interacting with $\boldsymbol{\mu}_{\mathbf{par}}$, and some of it is due to the probe laser's interaction with **j**. To determine the contribution from each, images can be taken using different polarization geometries of the pump and probe laser. This results in signal distributions which do not preserve cylindrical symmetry, a property that crushed image reconstruction algorithms require to recover the true anisotropy of the image.[17] Therefore, vector correlation measurements using traditional crushed ion imaging techniques are limited to fitting techniques using synthetic basis set images, or from taking cylindrically symmetric images using multiple probe transitions as has been demonstrated in atomic fragment imaging by Rakitzis et al.[36-37] Although some success has been previously obtained using basis set methods,[30, 38-40] the experiments are challenging since care must be taken to insure identical conditions are maintained between images obtained with different laser geometries since the relative intensities of the images is required. The analysis also requires construction of the appropriate basis sets, and a complex simultaneous fitting algorithm. Additionally, when fragments are produced with a wide range of velocities, extracting speed-dependent vector correlations is difficult with basis set methods. Therefore, we endeavored to create a more accessible method for obtaining speed-

dependent vector correlations from independent ion images by creating a set of analytical equations which are a function of the commonly measured β_n coefficients.

Slice imaging,[14, 41] provides a direct measurement of the speed-dependent signal anisotropy from a single ion image without requiring a reconstruction algorithm, regardless of the laser polarization geometry.[42] Slice imaging has previously been used to measure atomic angular momentum polarization,[43-44] but has not been applied to measure the angular momentum alignment of molecular fragments. If high-**j** molecular fragments are probed, it is not necessary to account for quantum coherence as is the case for atomic fragments. This allows us to determine all of the molecular fragment vector correlations using only four β_n coefficients taken from three independent ion images of different polarization geometries: $\beta_2^{\updownarrow\updownarrow}$, $\beta_4^{\updownarrow\updownarrow}$, $\beta_2^{\updownarrow\odot}$, and $\beta_2^{\odot\updownarrow}$.

B. Deriving the equations

Rakitzis and Zare give the expression for the molecular-frame photofragment detection probability (for k=2) as follows:[29]

$$I\left[\Theta,\Phi,\theta_\varepsilon,\beta,a_q^2(p)\right]= \tag{4.3}$$
$$1+h^{(2)}\{(1+\beta)\cos^2\theta_\varepsilon a_0^2(\|)P_2(\cos\Theta)+(1-\beta/2)\sin^2\theta_\varepsilon a_0^2(\perp)P_2(\cos\Theta)$$
$$+\sin\theta_\varepsilon\cos\theta_\varepsilon\,\mathrm{Re}\left[a_1^2(\|,\perp)\right]\sqrt{3/2}\sin 2\Theta\cos\Phi+(1-\beta/2)\sin^2\theta_\varepsilon a_2^2(\perp)\sqrt{3/2}\sin\Theta\cos 2\Phi\}$$

where Θ is the angle between the probe laser polarization ***P*** and the velocity **v**, θ_ε is the angle between the pump laser polarization ***E*** and **v**, and Φ is the azimuthal angle of ***E*** and ***P*** about **v**. β is the spatial anisotropy resulting from the pump transition and $a_q^2(p)$ are the second rank molecular frame alignment parameters, which are related

algebraically to the $\beta_Q^K(k_1k_2)$ parameters of Dixon by Eqs. (7a-7e) from Rakitzis et al.[45] For sliced image laser polarization geometries, Θ and θ_ε are equal to either the image angle θ (the angle between the fragment velocity and the X axis) if the respective laser is X polarized in the imaging plane, or $\pi/2$ if the laser is Z polarized perpendicular to the imaging plane. The angle Φ will be equal to either 0 if the ***E*** and ***P*** are polarized in the same plane, or $\pi/2$ if they are orthogonal. To relate the detection probability of a specific laser geometry to the measured β_k^{FG} coefficients in equation (1), equation (3) is integrated with the corresponding Legendre polynomial:

$$\beta_k^{FG} = \int_0^\theta I\left[\Theta,\Phi,\theta_\varepsilon,\beta_Q^K(k_1,k_2)\right]P_k(\cos\theta)\left(\frac{2k+1}{2}\right)\sin\theta d\theta \tag{4.4}$$

The results of this integration for the three relevant laser polarization geometries in the high-j limit yield the following equations for the β_k^{FG}coefficients in terms of the bipolar moment parameters of Dixon:

$$\beta_2^{\updownarrow\updownarrow} = \left(\frac{10}{7}\right)\frac{7\beta_0^2(20) - h^{(2)}\left(4\beta_0^2(22) - 7\beta_0^0(22)\right)}{4h^{(2)}\beta_0^2(02) + 5} \tag{4.5a}$$

$$\beta_4^{\updownarrow\updownarrow} = \left(\frac{6h^{(2)}}{7}\right)\frac{7\beta_0^2(02) - 5\beta_0^2(22)}{4h^{(2)}\beta_0^2(02) + 5} \tag{4.5b}$$

$$\beta_2^{\updownarrow\odot} = -\frac{4\beta_0^2(20) + h^{(2)}\left(3\beta_0^2(22) - \beta_0^2(02)\right)}{h^{(2)}\left(\beta_0^2(22) + \beta_0^2(02) + \beta_0^0(22)\right) - 2} \tag{4.5c}$$

$$\beta_2^{\odot\updownarrow} = h^{(2)} \frac{\beta_0^2(02) - 3\beta_0^2(22) - 4\beta_0^0(22)}{2\beta_0^2(20) + h^{(2)}\left(\beta_0^2(22) + \beta_0^2(02)\right) - 2}$$

(4.5d)

Where $h^{(2)}$ is the alignment sensitivity coefficient, which is dependent on the rotational branch of the resonant transition used to ionize the photofragment. Expressions for this coefficient are given by Greene and Zare:[35, 46]

$$P_{\uparrow}: h^{(2)} = -\left(\frac{J+1}{2J-1}\right), \quad Q_{\uparrow}: h^{(2)} = +1, \quad R_{\uparrow}: h^{(2)} = -\left(\frac{J}{2J+3}\right) \tag{4.6}$$

In the high-j limit $h^{(2)}$ approaches -0.5 for P and R branch transitions. The alignment sensitivity for P/R branch transitions is half as large as for Q branch transitions because $\boldsymbol{\mu}_{\mathbf{frag}}$ is defined by a 2D plane ($\boldsymbol{\mu}_{\mathbf{frag}} \perp \mathbf{j}$) instead of a 1D axis ($\boldsymbol{\mu}_{\mathbf{frag}} \| \mathbf{j}$).

The ↕↕ image gives rise to both 2nd and 4th order terms, since both lasers are polarized parallel to the imaging plane and thus the projection of the electric field of each laser onto the fragment velocity varies with θ. While the P_2 coefficient $\beta_2^{\updownarrow\updownarrow}$ is sensitive to all four alignment parameters, the cross term P_4 coefficient $\beta_4^{\updownarrow\updownarrow}$ is only dependent on rotational alignment $\beta_0^2(02)$ and the triple vector **μ-v-j** correlation $\beta_0^2(22)$.

The angular distribution of the XZ and ZX images, however, do not give rise to a P_4 term as only one laser is polarized in the imaging plane. The XZ image anisotropy $\beta_2^{\updownarrow\odot}$ is generally dominated by the **μ-v** correlation $\beta_0^2(20)$, and in the limit of small **j** correlations either due to zero angular momentum fragments or in detection saturation by high probe laser power, the measured image anisotropy reduces to the spatial anisotropy: $\beta_2^{\updownarrow\odot} = 2\beta_0^2(20)$. Similarly, in the limit of small vector correlations involving **μ**, the ZX image anisotropy $\beta_2^{\odot\updownarrow}$ reduces to twice the **v-j** correlation$\beta_2^{\odot\updownarrow} =$

$2h^{(2)}\beta_0^0(22)$. For example, this is the case where the dissociation lifetime is much larger than the parent rotational period, resulting in a loss of all **μ** information prior to fragmentation. Both of these reduced equations for the limiting cases are valid even outside of the high-j limit, and their validity can be easily identified from experimental observations. In the small **j** correlation limit, the image anisotropy will only be dependent on the pump laser polarization ($\beta_2^{\odot\updownarrow} = \beta_2^{\odot\odot}, \beta_2^{\updownarrow\updownarrow} = \beta_2^{\updownarrow\odot}$)and in the small **μ** correlation limit, the image anisotropy will only be dependent on the probe laser polarization ($\beta_2^{\odot\updownarrow} = \beta_2^{\updownarrow\updownarrow}, \beta_2^{\odot\odot} = \beta_2^{\updownarrow\odot}$).

The ⊙⊙ image will always be isotropic, as the electric fields of both lasers are polarized perpendicular to the fragment velocity vector, and thus $\beta_2^{\odot\odot} = \beta_4^{\odot\odot} = 0$. Although this measurement provides no dynamical insight, it is a convenient experimental check as any deviation from zero implies systematic errors such as incomplete laser polarization or a non-uniform Doppler sampling.

The system of four equations (Eq. 5a-5d) can be solved to express the desired bipolar moment parameters in terms of the measured β_K^{FG} coefficients:

$$\beta_0^2(20) = \frac{\left(\left(26\beta_2^{\updownarrow\odot}+77\right)\beta_2^{\odot\updownarrow}-139\beta_2^{\updownarrow\odot}+20\right)\beta_4^{\updownarrow\updownarrow}-\left(\left(30\beta_2^{\updownarrow\updownarrow}+24\right)\beta_2^{\updownarrow\odot}+48\right)\beta_2^{\odot\updownarrow}+\left(36\beta_2^{\updownarrow\updownarrow}+96\right)\beta_2^{\updownarrow\odot}+48\beta_2^{\updownarrow\updownarrow}}{2\left(\left(22\beta_2^{\updownarrow\odot}+7\right)\beta_2^{\odot\updownarrow}+7\beta_2^{\updownarrow\odot}-116\right)\beta_4^{\updownarrow\updownarrow}-\left(\left(6\beta_2^{\updownarrow\updownarrow}+48\right)\beta_2^{\updownarrow\odot}-12\right)\beta_2^{\odot\updownarrow}+12\beta_2^{\updownarrow\odot}+24\beta_2^{\updownarrow\updownarrow}+144} \quad (4.7a)$$

$$\beta_0^0(22) = \frac{\left(\left(26\beta_2^{\updownarrow\odot}-139\right)\beta_2^{\odot\updownarrow}+77\beta_2^{\updownarrow\odot}+20\right)\beta_4^{\updownarrow\updownarrow}-\left(\left(30\beta_2^{\updownarrow\updownarrow}+24\right)\beta_2^{\updownarrow\odot}-36\beta_2^{\updownarrow\updownarrow}-96\right)\beta_2^{\odot\updownarrow}-48\beta_2^{\updownarrow\odot}+48\beta_2^{\updownarrow\updownarrow}}{2h^{(2)}\left(\left(22\beta_2^{\updownarrow\odot}+7\right)\beta_2^{\odot\updownarrow}+7\beta_2^{\updownarrow\odot}-116\right)\beta_4^{\updownarrow\updownarrow}-\left(\left(6\beta_2^{\updownarrow\updownarrow}+48\right)\beta_2^{\updownarrow\odot}-12\right)\beta_2^{\odot\updownarrow}+12\beta_2^{\updownarrow\odot}+24\beta_2^{\updownarrow\updownarrow}+144}$$

(4.7b)

$$\beta_0^2(02) = \frac{5\left(\left(22\beta_2^{\updownarrow\odot}+7\right)\beta_2^{\odot\updownarrow}+7\beta_2^{\updownarrow\odot}-116\right)\beta_4^{\updownarrow\updownarrow}-\left(\left(6\beta_2^{\updownarrow\updownarrow}-24\right)\beta_2^{\updownarrow\odot}-24\right)\beta_2^{\odot\updownarrow}-24\beta_2^{\updownarrow\odot}+24\beta_2^{\updownarrow\updownarrow}}{4h^{(2)}\left(\left(22\beta_2^{\updownarrow\odot}+7\right)\beta_2^{\odot\updownarrow}+7\beta_2^{\updownarrow\odot}-116\right)\beta_4^{\updownarrow\updownarrow}-\left(\left(6\beta_2^{\updownarrow\updownarrow}+48\right)\beta_2^{\updownarrow\odot}-12\right)\beta_2^{\odot\updownarrow}+12\beta_2^{\updownarrow\odot}+24\beta_2^{\updownarrow\updownarrow}+144}$$

(4.7c)

$$\beta_0^2(22) = \frac{7\left(\left(26\beta_2^{\updownarrow\odot}-31\right)\beta_2^{\odot\updownarrow}+31\beta_2^{\updownarrow\odot}+20\right)\beta_4^{\updownarrow\updownarrow}+\left(\left(6\beta_2^{\updownarrow\updownarrow}-24\right)\beta_2^{\updownarrow\odot}+24\right)\beta_2^{\odot\updownarrow}+24\beta_2^{\updownarrow\odot}-24\beta_2^{\updownarrow\updownarrow}}{4h^{(2)}\left(\left(22\beta_2^{\updownarrow\odot}+7\right)\beta_2^{\odot\updownarrow}+7\beta_2^{\updownarrow\odot}-116\right)\beta_4^{\updownarrow\updownarrow}-\left(\left(6\beta_2^{\updownarrow\updownarrow}+48\right)\beta_2^{\updownarrow\odot}-12\right)\beta_2^{\odot\updownarrow}+12\beta_2^{\updownarrow\odot}+24\beta_2^{\updownarrow\updownarrow}+144}$$

(4.7d)

C. General expressions for systems outside the high-j limit

When probing low j fragments and the possibility of quantum coherence effects arises, $\beta_0^2(42)$ must be treated as a free parameter. In this case, the anisotropy coefficients are expressed as:

$$\beta_2^{\updownarrow\updownarrow} = \left(\frac{10}{7}\right)\frac{7\beta_0^2(20) - h^{(2)}\left(4\beta_0^2(22) - 7\beta_0^0(22)\right)}{4h^{(2)}\beta_0^2(02) + 5}$$

(4.8a)

$$\beta_4^{\updownarrow\updownarrow} = \left(\frac{72h^{(2)}}{7}\right)\frac{\beta_0^2(42)}{4h^{(2)}\beta_0^2(02) + 5}$$

(4.8b)

$$\beta_2^{\updownarrow\odot} = \frac{5h^{(2)}\left(6\beta_0^2(42) - 8\beta_0^2(22)\right) - 14\beta_0^2(02)}{h^{(2)}\left(6\beta_0^2(42) + 20\beta_0^2(22) + 14\beta_0^2(02)+35\beta_0^0(22)\right) - 35}$$

(4.8c)

$$\beta_2^{\odot\updownarrow} = 10h^{(2)}\frac{3\beta_0^2(42) - 4\beta_0^2(22) - 7\beta_0^0(22)}{35\beta_0^2(20) + h^{(2)}\left(6\beta_0^2(42) + 20\beta_0^2(22)+14\beta_0^0(22)\right) - 35}$$

(4.8a)

In this case, there are five unknown $\beta_Q^K(k_1k_2)$ parameters and thus this system of equations alone is not solvable. However, it is often possible to independently measure one or more of the bipolar moments. An independent measure of the spatial ($\beta = 2\beta_0^2(20)$) can be obtained by using a non-optical detection technique (if one is available) such as electron impact induced ionization, or by saturating the fragment **j** detection sensitivity using high probe laser power. In addition, a speed-independent rotational alignment $\beta_0^2(02)$ can be measured from the signal intensity of the total (unsliced) ion cloud when the pump and probe lasers are parallel ($I_\parallel$) and perpendicular ($I_\perp$) to each other using Equation (4.1).

D. Speed-dependent vector correlations

An important advantage of slice imaging is that it allows the extraction of *speed-dependent bipolar moment parameters*. In the photodissociation of a system with a polyatomic co-fragment, the multitude of energetic degrees of freedom present often results in a broad speed distribution corresponding to the distribution of internal states of the undetected co-fragment. For such systems, it is likely that different angular momentum polarizations result from fragments arising from unique geometries and exit channel torques. The anisotropy of any speed of an infinitely sliced image can be obtained simply by changing the radial limits of the angular integration. In reality, of course, all slicing has a finite width limited by the experimental detection gate width and the speed of the fragments. Partial slicing has the effect of overlapping the signal from different fragment velocities, averaging the true anisotropy over multiple speeds. To determine the magnitude of this effect, a set of images with a well defined set of speed-

dependent bipolar moment parameters was simulated. The simulated images are composed of 300 evenly distributed fragment velocities ranging from 250 m/s to 850 m/s, with a moderate parent molecule temperature resulting in approximately 100-200 m/s velocity blurring, a reasonable experimental value. The bipolar moments of the lowest speed fragments are defined by the limiting C case as defined by Dixon,[33, 35] where **μ** is parallel to **j** but perpendicular to **v**. As the speed of the fragments increases, the **j** vector gradually moves toward the **v** vector until at the highest fragment speed the bipolar moments are defined by case D, where **v** is parallel to **j** but perpendicular to **μ**. This results in a linear change of the $\beta_0^0(22)$ and $\beta_0^2(02)$ parameters with fragment speed, but $\beta_0^2(20)$ and $\beta_0^2(22)$ values fixed at -0.5 and 0.5 respectively. The resulting image was sliced with varying detection gate widths, and the anisotropy parameters β_k^{FG} extracted at all speeds with overlapping 8 pixel wide bins. The resulting anisotropy parameters were solved with Eqs. (4.7a-4.7d) to obtain the bipolar moment parameters, which are displayed in **Figure 18** as a function of fragment speed.

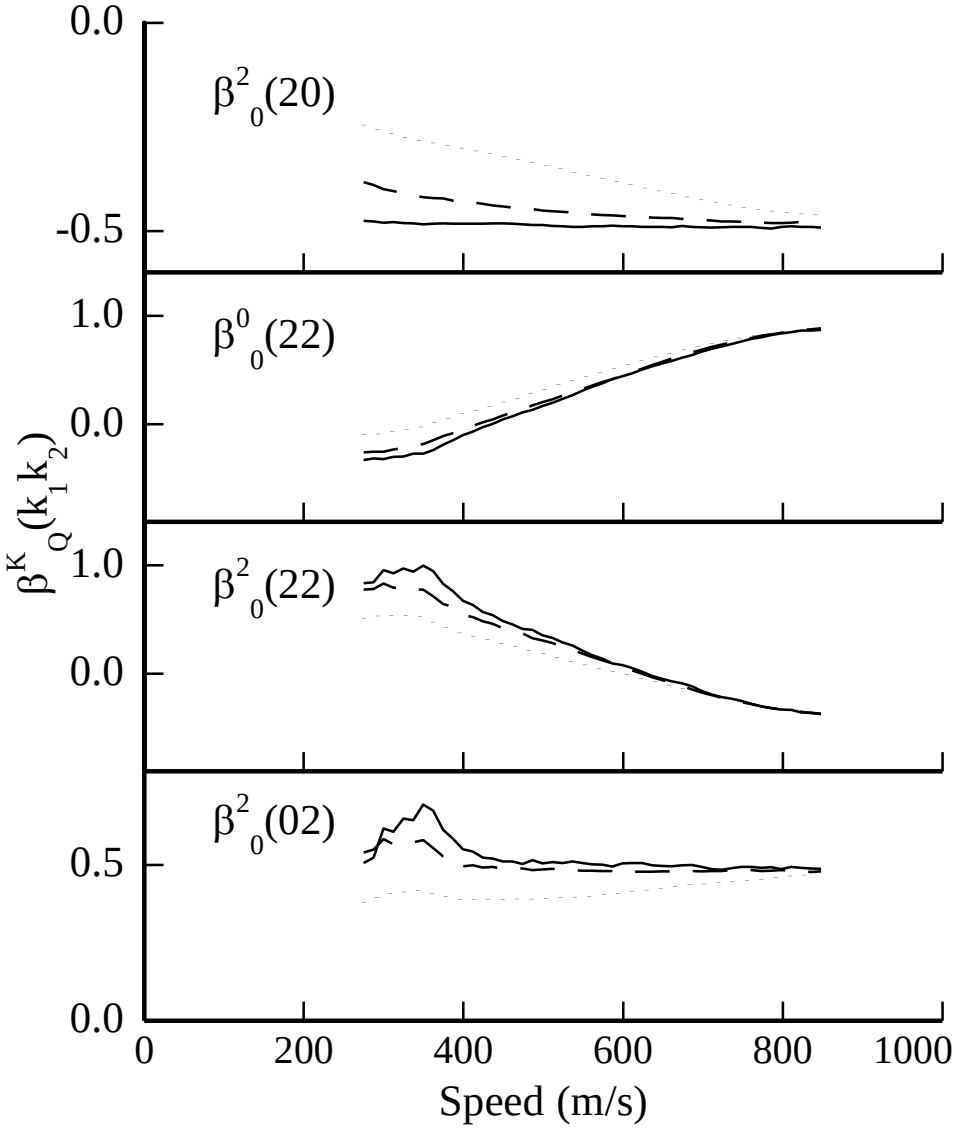

Figure 18: Speed dependent vector correlations of simulated images to demonstrate the effect of imperfect slicing. $\boldsymbol{\beta_Q^K(k_1k_2)}$ parameters for a simulated ion image from a pure Q-branch transition, ranging from limiting case C ($\boldsymbol{v \perp \mu \parallel j}$) at low velocities to limiting case D ($\boldsymbol{\mu \perp v \parallel j}$) at high velocities, at three separate sliced widths: 1% (solid line), 24% (dashed line), and unsliced (dotted line).[47]

As expected, for an unsliced image the observed speed-dependent parameters diverge significantly from their true values at lower speeds as a result of increasing

contributions from higher speeds to the signal at each radii. For slicing widths below approximately 20% of the maximum speed however, this divergence is relatively minor (>10%). It should be noted that the C and D cases presented here should be among the most sensitive cases to finite slicing divergence of the $\beta_0^2(20)$ parameter, since they arise from a perpendicular transition and the majority of the signal is in the center of the image for when the pump laser is polarized within the image plane ($\updownarrow$), which are the geometries most sensitive to $\beta_0^2(20)$. For out-of-plane ($\odot$) pump polarization geometries which are most sensitive to the $\beta_0^0(22)$ parameter, the majority of the signal is around the edges of the image resulting in less divergence from the true value. For a parallel transition, opposite is true and a more accurate speed-dependent $\beta_0^2(20)$ parameter would be obtained while the $\beta_0^0(22)$ parameter would be less accurate at lower fragment speeds.

In order to test and characterize the analytical expressions on a well-studied molecule, both traditional crush imaging and slice imaging experiments were performed on the NO_2 system. The results are shown in Appendix A.

CHAPTER V

THE STORY OF NO_3 PHOTODISSOCIATION

"A theory is something nobody believes, except the person who made it. An experiment is something everybody believes, except the person who made it."

-Albert Einstein

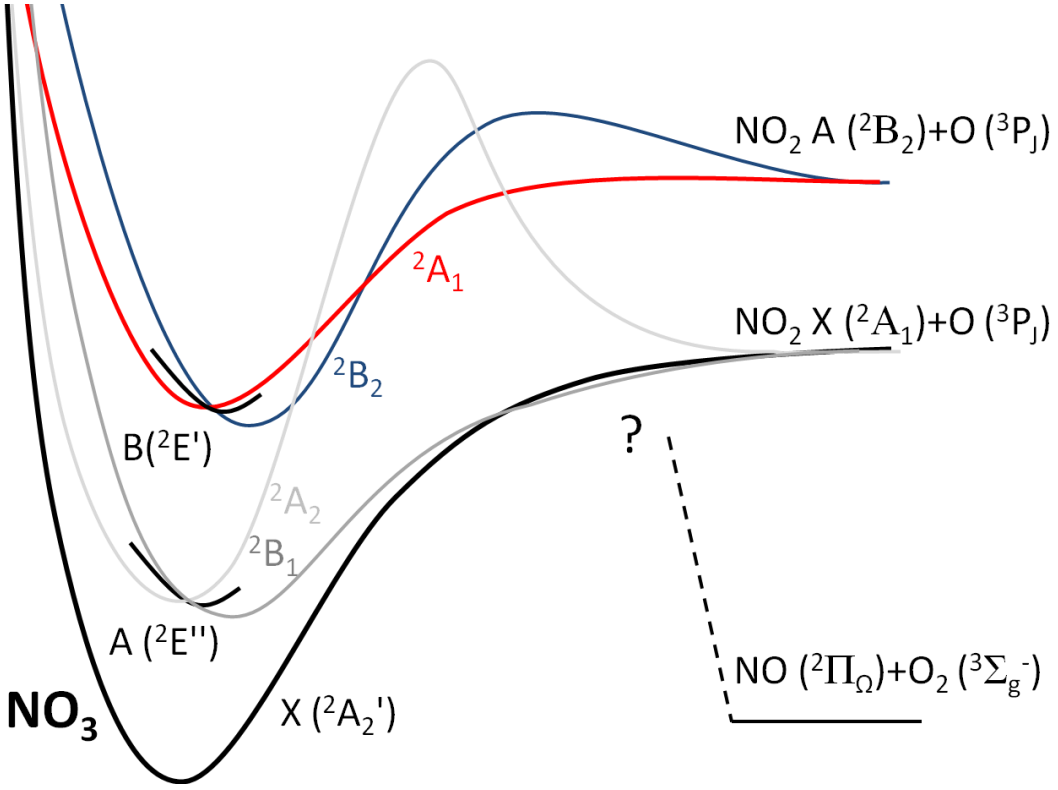

Figure 19: Potential energy curves for the lowest lying electronic states of NO_3. Based on ref [48].

There are three electronic states of NO_3 in the D_{3h} geometry at energies accessible to dissociation via the NO + O_2 channel: the ground X ($^2A'_2$) state, the dark (electric dipole forbidden) A ($^2E''$) state, and the bright B ($^2E'$) state. Both of the excited states are doubly degenerate in the D_{3h} geometry, but are subject to significant

degeneracy breaking Jahn-Teller effects when an N-O bond is stretched, giving way to the A ($^2B_1$), A ($^2A_2$), B ($^2B_2$), and B ($^2A_1$) states in the C_{2v} geometry. Excitation energies and asymptotic correlations have been calculated and discussed at length by Eisfeld and Morokuma.[48] Schematic potentials of these states are provided for visualization purposes in Figure 19.

Visible photolysis proceeds via initial excitation to the 'bright' B ($^2E''$) state. The oscillator strength of the B ($^2E'$) ← X ($^2A'_2$) transition is large, and thus it is expected to have a short radiative lifetime (~50 ps).[48] Experimental fluorescence lifetimes are observed to be much longer (340 ± 20 μs) and have been attributed to strong linear Pseudo-Jahn-Teller (PJT) vibronic coupling with the higher vibrational levels of the ground state mediated by the asymmetric bending and stretching modes.[49-50] The B ($^2E''$) state does not asymptotically correlate to the experimentally observed NO_2 X ($^2A_1$) + O (^3P_J) product channel,[48] providing further evidence for coupling to the lower energy electronic states prior to dissociation. Additionally, the initially excited B ($^2E'$) state is crossed by the A ($^2A_2$) state, due to a large barrier originating from the orbital symmetry forbidden breaking of the N-O bond on this surface.[48] The other A state Jahn-Teller potential, A ($^2B_1$), correlates barrierlessly to the NO_2 X ($^2A_1$) + O (^3P_J) asymptote.

Of more interest to us, however, is the nature of the potential energy surface leading to the NO + O_2 products. As previously discussed the timescale of our measurements do not allow us to observe the progress of the reaction along this surface,

but we can answer this question by interpreting clues found in the two product fragments.

A. Product distribution measurements

The first experiment to measure the internal energy distribution of the $NO_3 \rightarrow NO + O_2$ photoproducts was performed by Davis and Lee in 1993.[18] The authors used neutral time-of-flight photofragment translational spectroscopy to measure the total translational energy distribution of the product fragments (**Figure 20**). The authors utilized electron impact ionization instead of a state-selective REMPI scheme, and thus the translational energy distribution represents an average of all possible product state combinations. Regardless, the energy distribution clearly reveals the presence of highly excited O_2 products, although it was unclear whether the excitation was predominantly electronic O_2 ($^1\Delta_g$; v = 0-4) or vibrational O_2 ($^3\Sigma_g^-$; v = 5-10). Three years later, state-selective LIF experiments conducted by Mikhaylichenko et al. confirmed the presence of excited O_2 products and additionally measured an NO rotational temperature of 1400±300 K with low vibrational energy.[5]

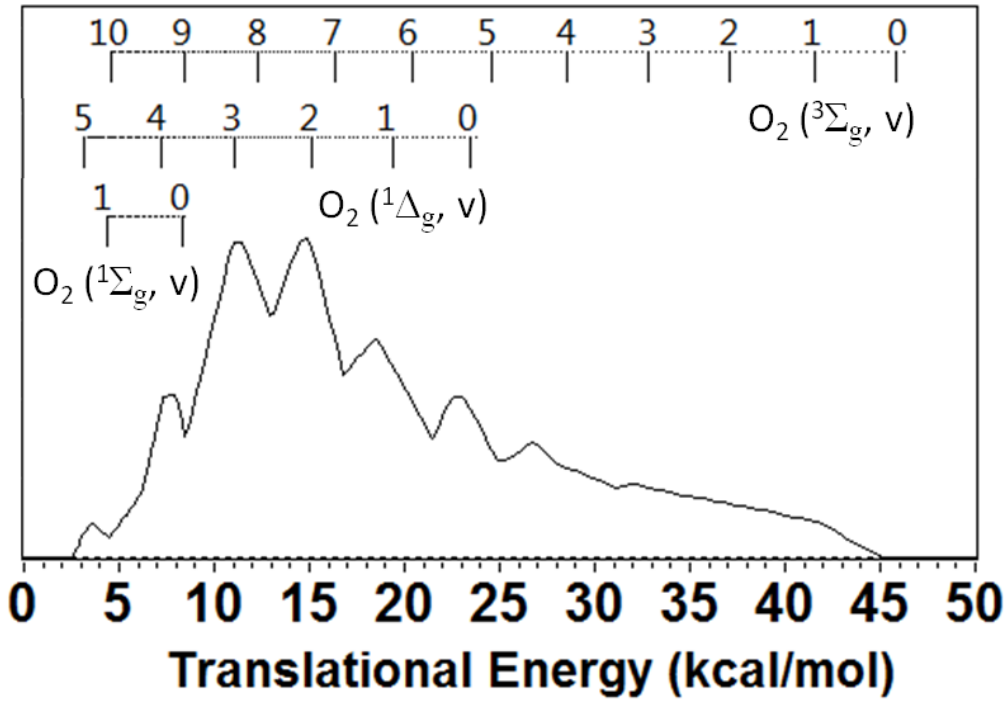

Figure 20: Total translational energy distribution for the NO + O_2 products resulting from NO_3 photodissociation at 588 nm. Reproduced from ref [18]. The calculated maximum relative translational energies for production of NO($^2\Pi$; v=0) + O_2($^3\Sigma$, $^1\Delta$, $^1\Sigma$; v) are indicated by the combs.

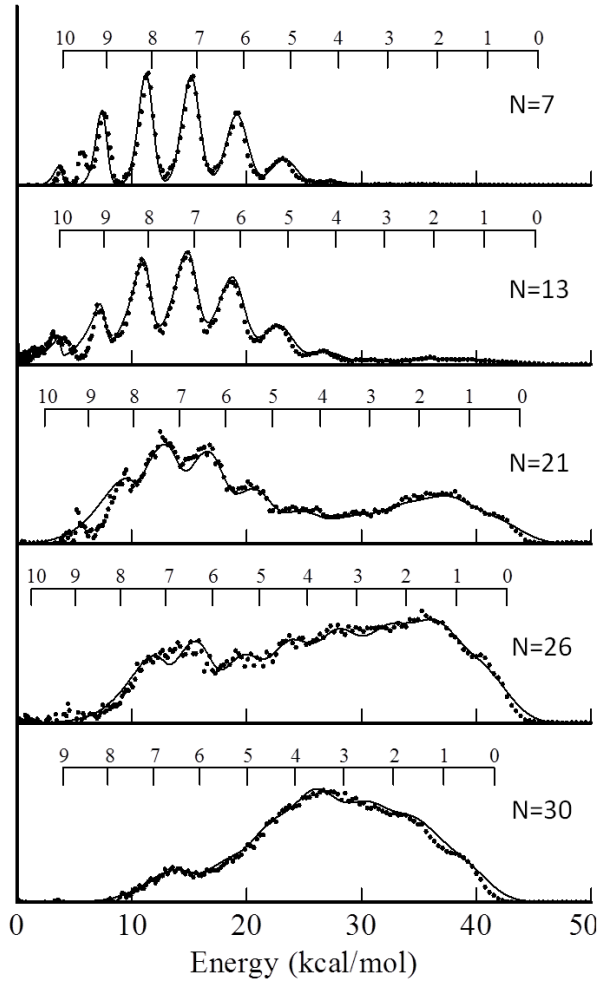

Figure 21: Total translational energy distributions of NO ($^2\Pi$; v=0; N=7, 13, 21, 26, 30) arising from NO_3 photodissociation at 588 nm (dots). Forward convolution fits (solid lines) to the experimental data (dots) are also provided.

Figure 21 shows translational energy distributions derived from ion images NO ($^2\Pi$; v=0; N=7, 13, 21, 26, 30), along with forward convolution fits obtained using the methodology detailed in Chapter III to determine the internal energy distribution of the cofragment. Based on simulations to the $I(E_T)$ distributions we find that the low translational energy signal must originate from vibrational excitation of O_2 ($^3\Sigma_g^-$) fragments. Attempts to model the structure of the NO ($^2\Pi_\Omega$; v=0, N=7) $I(E_T)$assuming

significant O_2 ($^1\Delta_g$) co-fragments were inconsistent with the data. The previous state-averaged measurements of Davis et al.[18] and the lower resolution pump-probe measurements of Mikhaylichenko et al.[5] were unable to discount the formation of O_2 ($^1\Delta_g$) in the dissociation. The combs above the distributions in **Figure 21** correspond to the energetic limits associated with O_2 ($^3\Sigma_g^-$) vibrational states. The $I(E_T)$ distributions were modeled assuming a Gaussian rotational distribution for each O_2 ($^3\Sigma_g^-$) vibrational band of variable intensity. The peak of the rotational distributions varied from N_{max} =11 coincident with NO ($^2\Pi_\Omega$; v=0, N=7) to N_{max} =29 coincident with NO ($^2\Pi_\Omega$; v=0, N=30) with FWHM widths varying from ΔN=12-28 over this same range. A single O_2 rotational distribution was employed for every O_2 vibrational band coincident with a specific NO ($^2\Pi_\Omega$; v=0, N) state. Both the N_{max} and ΔN parameters describing the O_2 rotational distributions showed an increasing trend with increased NO rotation, indicating a positive correlation in the angular momentum of both fragments. Further parameterization was not required to provide reasonable fits to the experimental distributions, although there is evidence that the rotational distributions vary with O_2 vibration for each detected NO state. For the highest NO rotational states individual O_2 vibrational contributions are unresolved and therefore the continued use of Gaussian rotational distributions is driven by convenience since alternative choices would likely still provide a reasonable fits to the experimental distributions. The partitioning between O_2 vibrational and rotational excitation is therefore less certain. The sharp features near 25 kJ/mol that are not fit by the simulations are due to NO arising from NO_2 photodissociation by the probe laser.

The $I(E_T)$ distributions derived from the reconstructed images exhibit strong evidence of two distinct product channels. One channel (Pathway A), formed in coincidence with lower rotational states of NO ($^2\Pi_\Omega$), results in vibrationally excited O_2 ($^3\Sigma_g^-$) fragments (v = 5-10). The $I(E_T)$ distribution associated with of NO ($^2\Pi_{1/2}$; v=0, N=7) in the top panel of Figure 21 shows very narrow peaks corresponding to low O_2 rotational excitation. A second feature begins to emerge in $I(E_T)$distributions associated with higher detected NO rotational states (Pathway B). Although the vibrational structure in this channel is not well-resolved in any image, conservation of energy dictates that the signal must correspond to O_2 ($^3\Sigma_g^-$) fragments as well.

$NO_3 + h\nu \rightarrow NO\ (^2\Pi_\Omega,\ v = 0\text{-}1,\ \text{low N}) + O_2\ (^3\Sigma_g^-,\ v = 5\text{-}10)$ (Pathway A)

$\rightarrow NO\ (^2\Pi_\Omega,\ v = 0\text{-}1,\ \text{high N}) + O_2\ (^3\Sigma_g^-,\ v = 0\text{-}4)$ (Pathway B)

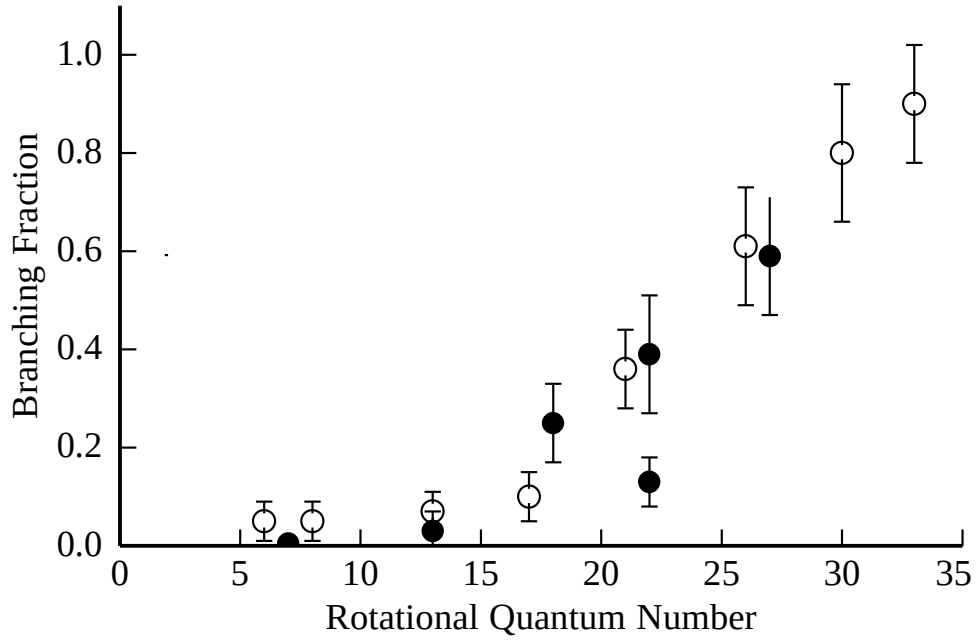

Figure 22: The branching fraction of Pathway B as a function of NO rotational state for NO($^2\Pi_{3/2}$) (filled circles) and NO($^2\Pi_{1/2}$) (open circles).[51]

The branching fraction of Pathway B as a function of NO ($^2\Pi_{1/2}$, v = 0, N) and NO ($^2\Pi_{3/2}$; v=0, N) is shown in Figure 22 and ranges from 0.0±0.05 for NO (N = 7) to above 0.85±0.15 for NO (N = 33). These branching fractions were estimated assuming the correlated O_2 vibrational distribution of each channel was equivalent for each NO state, although subtle differences in these distributions were in fact observed. This assumption, however, was necessary because the loss of structure in the highest NO N-state $I(E_T)$ distributions precluded a unique decomposition into the two channels. The branching of the two pathways with NO rotational state was independent of the probed spin-orbit state. One image associated with the NO ($^2\Pi_{3/2}$; v=0, N=22) state, detected via the P_{22} branch, indicated an under population of Pathway B relative to the trend of the other states. Although initially puzzling, this observation was later identified to be a signature of the Λ doublet preferences of the channels. This effect will be discussed in later in this chapter.

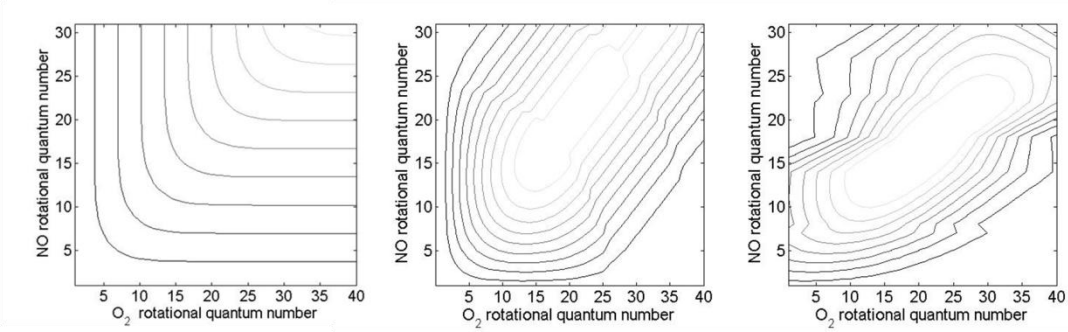

Figure 23: Correlated rotational state distributions of NO and O_2 photoproducts. The left plot shows a simulated statistical angular momentum distribution resulting from NO_3 (T_{rot}=20 K), and the middle shows the same model but constrained by an exit impact parameter of 0.2 Angstroms. The right plot shows the experimental angular momentum distribution extracted from the state-selected NO translational energy distributions weighted with a rotational temperature of 1300 K.[51]

The rotational distributions of the O_2 and NO fragments exhibit a clear positive correlation, i.e. as the rotational state of the detected NO increases, the average rotational state of the correlated O_2 increases. Figure 23 (right panel) shows the correlation between the rotational states of the two fragments for this channel. As previously discussed this was obtained by fitting the $I(E_T)$ distributions derived from state-selected NO (N = 7 - 33) images with Gaussian rotational distributions for correlated O_2, assumed to be equivalent for each O_2 vibrational band. Linear interpolation of the Gaussian parameters was used to provide continuous O_2 rotational distributions. The intensity of each O_2 rotational distribution was weighted using a Boltzmann rotational temperature of 1300 K for NO. The resulting angular momentum correlation in Figure 23 is shown to be highly constrained. Shown for comparison in the left panel of Figure 23 is the statistical, Phase Space Theory (PST), prediction appropriate for describing loose transition states. PST populates coincident states according to 2J+1 rotational degeneracy, conserving both energy and angular momentum:

$$J_{par} = J_{O_2} + J_{NO} + l \tag{5.1}$$

Where l is the orbital angular momentum quantum number of the fragments. The statistical model not surprisingly fails to capture the strong correlations observed experimentally, which could indicate a dynamically constrained impact parameter for the reaction. The impact parameter b is related to the classical orbital angular momentum L and the quantum angular momentum l through the following equation:

$$L = \hbar\, l(l+1) = \mu v b \tag{5.2}$$

Where v is the center of mass recoil velocity and μ is the reduced mass of the molecule. This equation can be used to calculate a maximum l number and constrain the PST model by only counting combinations of J_{NO} and J_{O2} that require $l<l_{max}$ to conserve angular momentum. The middle panel of Figure 23 shows an example of a PST model constrained by a maximum impact parameter of 0.2 Å.

Images of NO ($^2\Pi_\Omega$, v = 1, N) fragments were also obtained via the A-X (0, 1) band near 235 nm. Figure 24 shows the translational energy distribution of NO($^2\Pi_{1/2}$; v=1, N=15) resulting from 588 nm photolysis of NO_3. Although the $I(E_T)$ distributions associated with NO (v = 1) fragments are *energetically* similar to the distributions of the NO (v = 0) images, the available energy is decreased by the NO vibrational energy (~23 kJ/mol). Therefore the O_2 vibrational distributions are shifted by one quantum (~19 kJ/mol) relative to the NO ($^2\Pi_\Omega$, v = 0, N) results. Previously Mikhaylichenko et al. measured the NO vibrational product yield to be about 90% v=0 and 10% v=1.[5] This yield is consistent with Franck-Condon calculations[52-53] assuming there is no change in the bond length between the NO before and after photolysis. The similarity between NO(v=0) and NO(v=1), and the observed absence of higher NO(v) quantum numbers, indicates that the NO fragment acts as a spectator in the NO_3 photolysis.

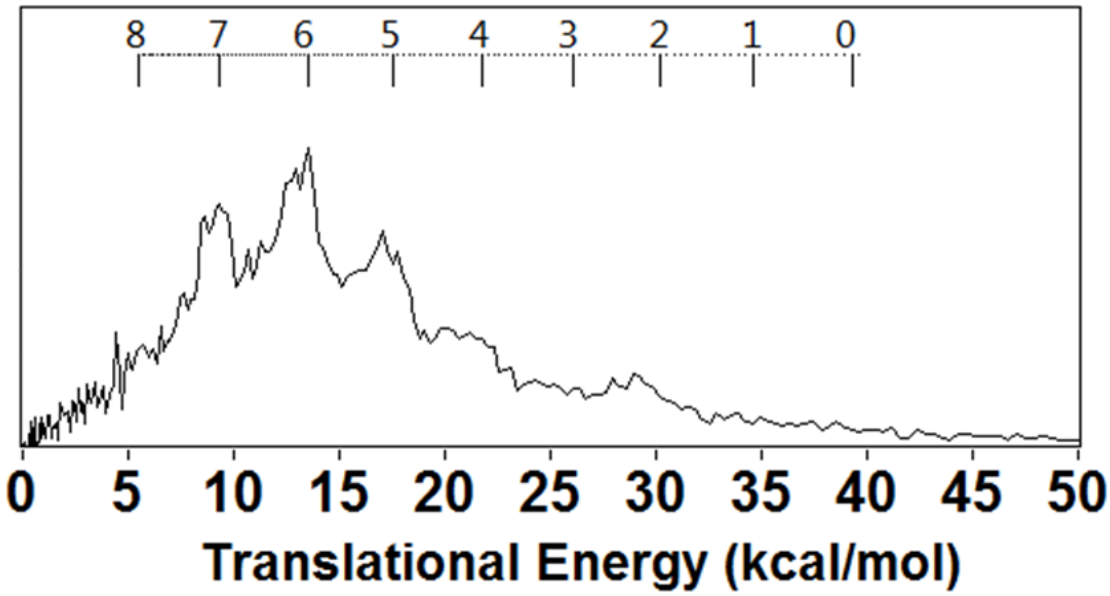

Figure 24: Total translational energy distribution of NO($^2\Pi_{1/2}$; v=1, N=15) resulting from 588 nm photolysis of NO_3.

In the sudden dissociation limit, the vibrational state distribution of the product fragments can be approximated by the wave function overlap (Franck-Condon factor) of a free O_2 molecule and an O_2 molecule with a bond length equal to the O-O bond length in the transition state. We have therefore simulated the O_2 vibrational distributions assuming a sudden approximation, justified by the large release of potential energy in the exit channel, employing vibrational Franck-Condon analysis to estimate the O-O bond length in the transition state. Figure 25 shows the results of Franck-Condon simulations of the vibrational distributions for Pathways A and B assuming a Morse oscillator for the O_2. We find excellent agreement with the experimental derived distributions assuming O_2 bond lengths at the time of impulse of 1.451 Å (A) and 1.320

Å (B), which are considerably extended from the equilibrium O_2 bond length of 1.207 Å.[54]

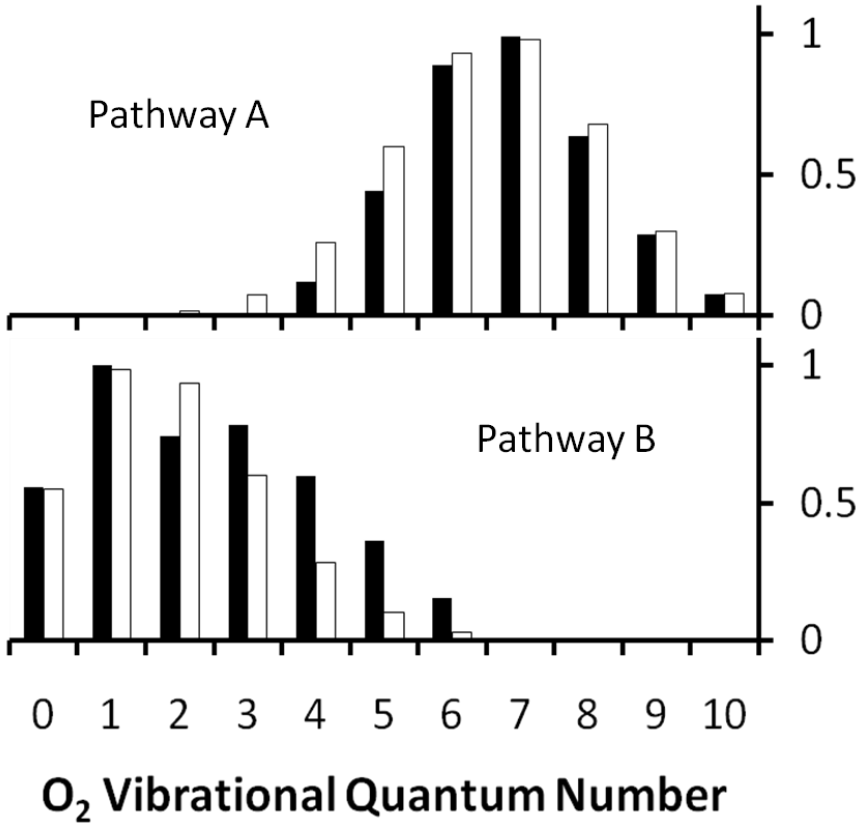

Figure 25: Estimated state-averaged O_2 vibrational distributions for the molecular product channels (black bars) and Franck-Condon simulations (white bars). The O-O bond distances used in the simulations are 1.451 Å (Pathway A) and 1.320 Å (Pathway B) respectively.[51]

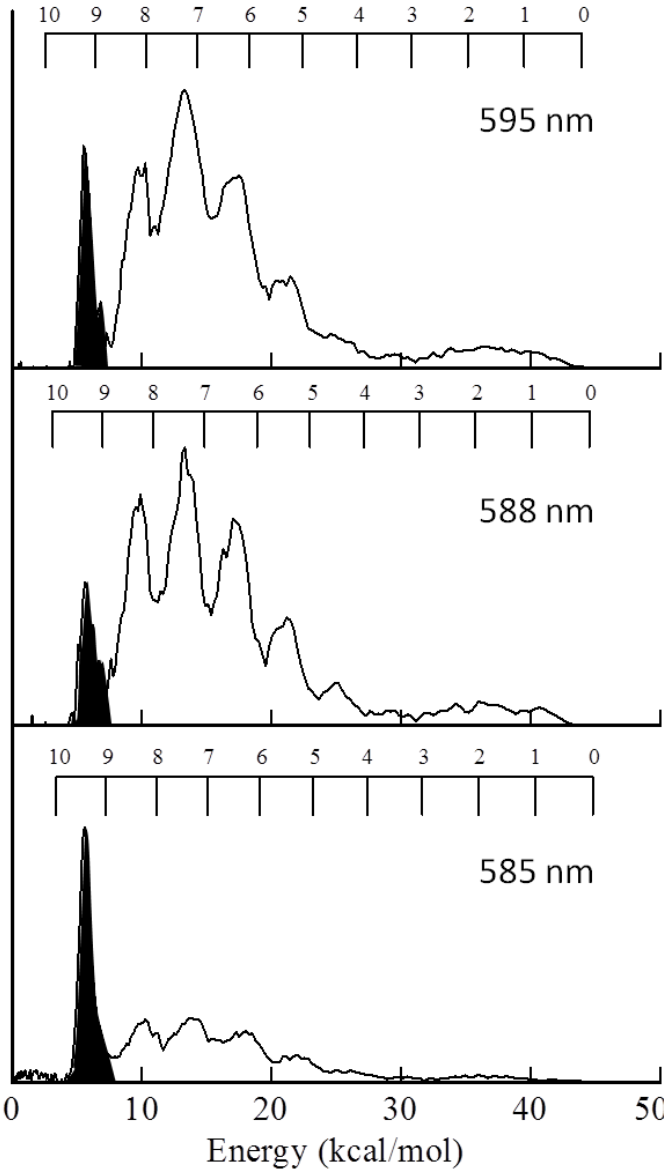

Figure 26: Total translational energy distribution derived from NO($^2\Pi_{1/2}$,v = 0) at different pump wavelengths. The feature near 6 kcal/mol is due to NO_2 photodissociation at 226 nm.

The measured translational energy distributions of specific NO states were found to be independent of the photolysis wavelength over the 585-595 nm range, except for the expected shifts due to the small changes in available energy. As previously noted, this range of wavelengths corresponds to only 0.74 kcal/mol (258 cm^{-1}) in energy and

the product energy partitioning is dominated by the large exit barrier for this channel. In addition, NO_3 parent molecules with a single quantum of vibrational energy (363 cm^{-1}) would have enough energy to dissociate exclusively via the atomic elimination channel. $I(E_T)$ distributions from NO ($^2\Pi_{1/2}$, v = 0, N = 17) at 585 nm, 588 nm, and 595 nm are shown in Figure 26. The feature associated with the 225 nm photodissociation of background NO_2 has intentionally not been subtracted from these distributions to illustrate the relative change in the NO + O_2 channel at different photolysis wavelengths since the NO_2 contribution is only dependent on the fixed probe laser. Figure 26 shows the signal relative to the probe induced dissociation of NO_2 as a function of wavelength. As expected, the contribution from the NO + O_2 channel decreases sharply at 585 nm, the atomic elimination channel threshold, and exhibits a maximum near 588 nm which was also observed by Davis et al.[18] corresponding to a maximum in the NO_3 absorption cross section.

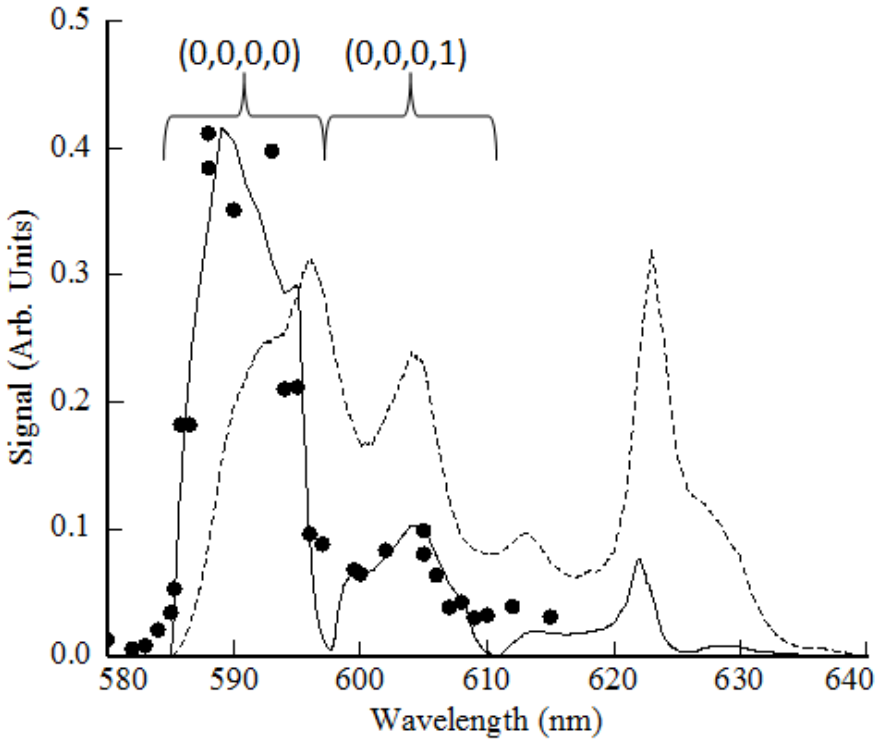

Figure 27: The relative experimental yields for the NO + O_2 channel at a series of experimental wavelengths (closed symbols). Simulated yields of the NO + O_2 channel with 20 K rotational and 300 K vibrational temperatures and 300 K rotational and 300 K vibrational temperatures are shown as the solid and dashed lines respectively.[51]

The relative intensity of the NO_2 background signal and the NO_3 signal at different wavelengths can be used to estimate the temperature of the parent NO_3 molecules in the molecular beam based on the model of Johnston et al.[3] The relative signal intensities were simulated with a simple model assuming a unitary quantum yield for NO production if the combined pump photon and NO_3 internal energy is above the NO + O_2 channel threshold, but a quantum yield of 0 if the combined energy is above the NO_2 + O threshold, where that channel dominates. The solid line in Figure 27

shows the expected NO product yield arising from T_{vib}=300 K and T_{rot}=20 K NO_3 molecules, which provides a best fit to the experimental data. The much colder rotational temperature of the NO_3 molecular beam is not unexpected, as rotational cooling is more efficient than vibrational cooling. However, although the beam itself is comprised of a 300 K distribution of vibrational states, only a single vibrational state of NO_3 gives rise to NO + O_2 products at a particular wavelength, as the 258 cm^{-1} window where this channel is observed is smaller than the lowest NO_3 vibrational frequency (363 cm^{-1}, Table 3). In this sense, our 588 nm ion images effectively arise from a 0 K NO_3 vibrational distribution.

Table 3: Vibrational modes and frequencies of NO_3

D_{3h}	Mode	Frequency (cm^{-1})[55]
ν_1 (a'_2)	Sym. Stretch	1061
ν_2 (a''_2)	Out-of-plane bend	762
ν_{3-4} (e'_2)	Asym. Stretch (2)	1490
ν_{5-6} (e'_2)	Asym. Bend (2)	363

B. The roaming oxygen atom

The clues obtained from the initial ion imaging experiment strongly indicated that Pathway A arises from the so-called "roaming mechanism", originally observed in formaldehyde (CH_2O) photodissociation 1993 by van-Zee et al using LIF experiments[6] and later in 2004 using ion imaging.[7] The authors observed two pathways from in their ion imaging results as well: one pathway which resulted in rotationally excited CO and vibrationally cold H_2 fragments, and one pathway which resulted in rotationally cold

CO and vibrationally excited H_2 fragments. The former pathway has long been known to arise from a "skewed" transition state, where the hydrogen atoms come together on one side of the C-O bond. This creates a strong torque on the fragments during dissociation, resulting in rotationally excited fragments. The other pathway however, with the help of theoretical calculations, was identified as a new type of mechanism: the roaming mechanism. The roaming mechanism was characterized as a frustrated atomic elimination pathway. One of the hydrogen atoms is stretched to long bond lengths, but is not able to fully break the bond and form the HCO + H products. Instead, the loosely bound hydrogen slowly "roams" about the rest of the molecule, exploring a large and flat region of the potential energy surface. Eventually, it encounters a reactive site and abstracts another oxygen atom, creating H_2 and CO. The H_2 is formed at an extended bond length, which leads to the observed vibrational excitation in the photofragment. This vibrational excitation is exactly what we observe in the O_2 photoproduct from NO_3 photodissociation. Furthermore, the roaming channel is only accessible in formaldehyde at photolysis energies that lie just below the HCO + H asymptote. As we have previously noted, the threshold of the NO + O_2 channel is less than one kcal/mol below the NO_2 + O asymptote. Therefore, we proposed a roaming oxygen atom mechanism as an explanation for Pathway A (Figure 28).

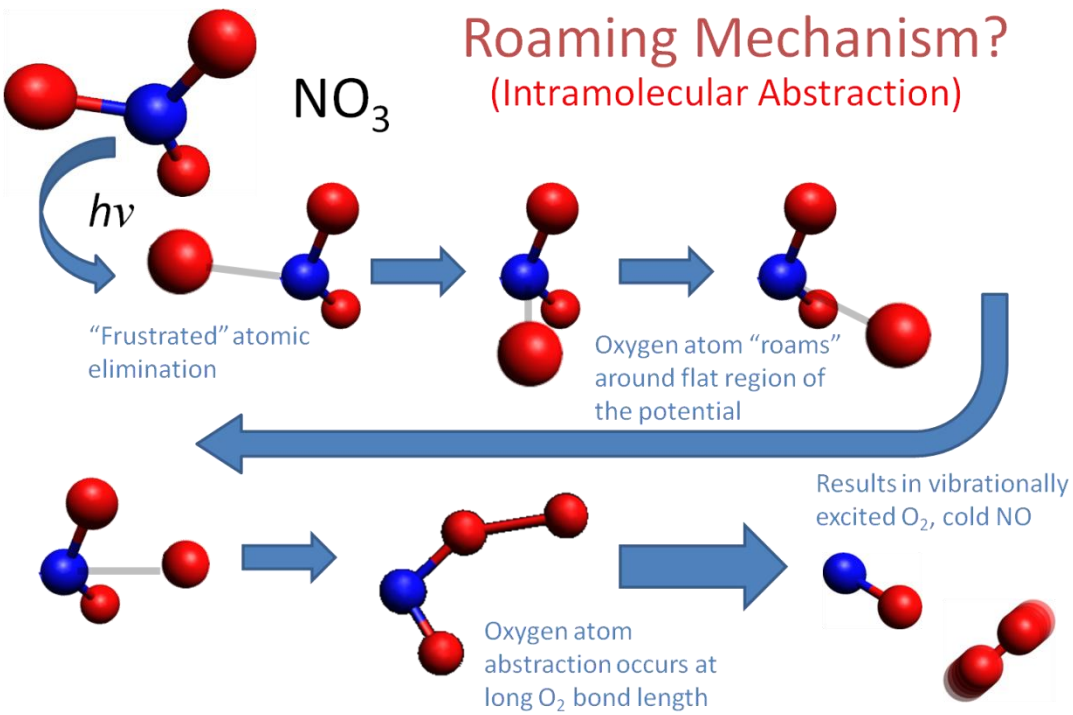

Figure 28: Diagram of possible oxygen roaming-type mechanism for NO_3 photodissociation.

Recent trajectory calculations by Christoffel et al. predicted similar H_2 vibrational distributions arising from the unimolecular roaming mechanism and the direct H + HCO abstraction reaction.[56] Thus, the O_2 produced as a result of oxygen atom roaming, or large amplitude motion, should resemble the dynamics of direct oxygen atom abstraction from NO_2. Although the O + NO_2 reaction proceeds via both a direct (60%) and complex forming mechanism (40%)[57] we predict that >70% of the complexes will follow a roaming mechanism. Therefore, a comparison with the bimolecular results should be instructive.[56] Vibrationally excited O_2 fragments from the thermal $NO_2 + O \rightarrow NO + O_2$ reaction have been previously observed by Lipscomb

et al. using flashlamp absorption spectrometry,[58] and later Smith et al. reported more detailed LIF measurements.[59] Due to diminishing Franck-Condon factors, relative O_2 vibrational state populations could only be determined for v = 6-11 states, where a monotonic decrease in population was observed. The O_2 vibrational distributions from Smith et al. as well as the NO state-averaged O_2 vibrational distributions obtained in the present study are displayed in Figure 29. The agreement between the two distributions are remarkable, although measurements of the O_2 (v = 0-5) populations resulting from the $O + NO_2 \rightarrow NO + O_2$ reaction would have provided a more convincing connection, particularly the clear maximum at O_2 (v = 6-7).

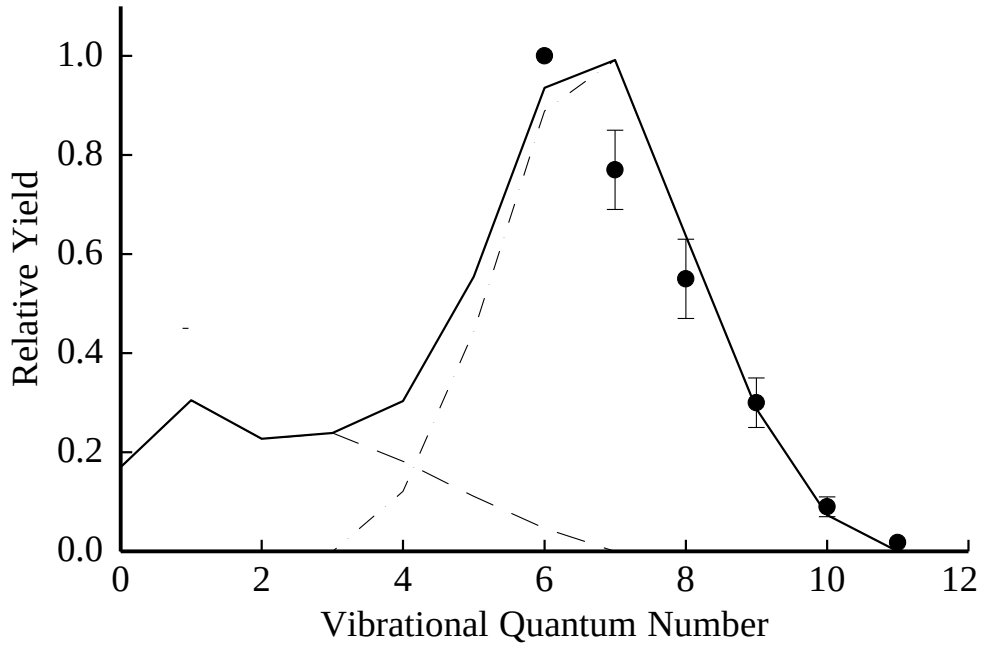

Figure 29: The total O_2 vibrational distribution from NO_3 dissociation at 588 nm (solid line) compared to LIF measurements (symbols) arising from the O (^{3}P) + $NO_2 \rightarrow NO + O_2$ reaction reported by Smith et al [59]. Also shown are the approximate state-averaged vibrational distributions of Pathway A and Pathway B separately.[51]

The nature of Pathway B, however, was less clear. Because the resulting product distribution is similar to the skewed transition state channel of formaldehyde, we hypothesized that it may arise from a previously undiscovered tight transition state.

C. Ab initio calculations

In an attempt to explain our experimental results, Xiao et al. performed ab initio calculations of key features of the potential energy surfaces for the lowest four electronic states of NO_3.[60] The potentials were explored systematically at the five state-averaged CASSCF(11e,8o)/6-31G level by the global reaction route mapping (GRRM) method. These calculations revealed a series of conical intersections between the different electronic potentials, through which the authors hypothesized the reaction could proceed to the NO + O_2 asymptote. The proposed mechanism is shown in Figure 30. After initial excitation to the B (^{2}E') state, a conical intersection (CI_{B-A}) leads to the optically dark A ($^2A_2$) state, due to a large barrier originating from the orbital symmetry forbidden breaking of the N-O bond on this surface.[48] From there, the other A state Jahn-Teller potential, A ($^2B_1$), can be accessed via another conical intersection, CI_{A-A}. Oxygen atom roaming then occurs on the A ($^2B_1$) state, which then accesses a third conical intersection (CI_{A-X}) to the X($^2A_2$ ') ground state just before oxygen atom abstraction, where the molecular structure resembles ONO-O.[60]

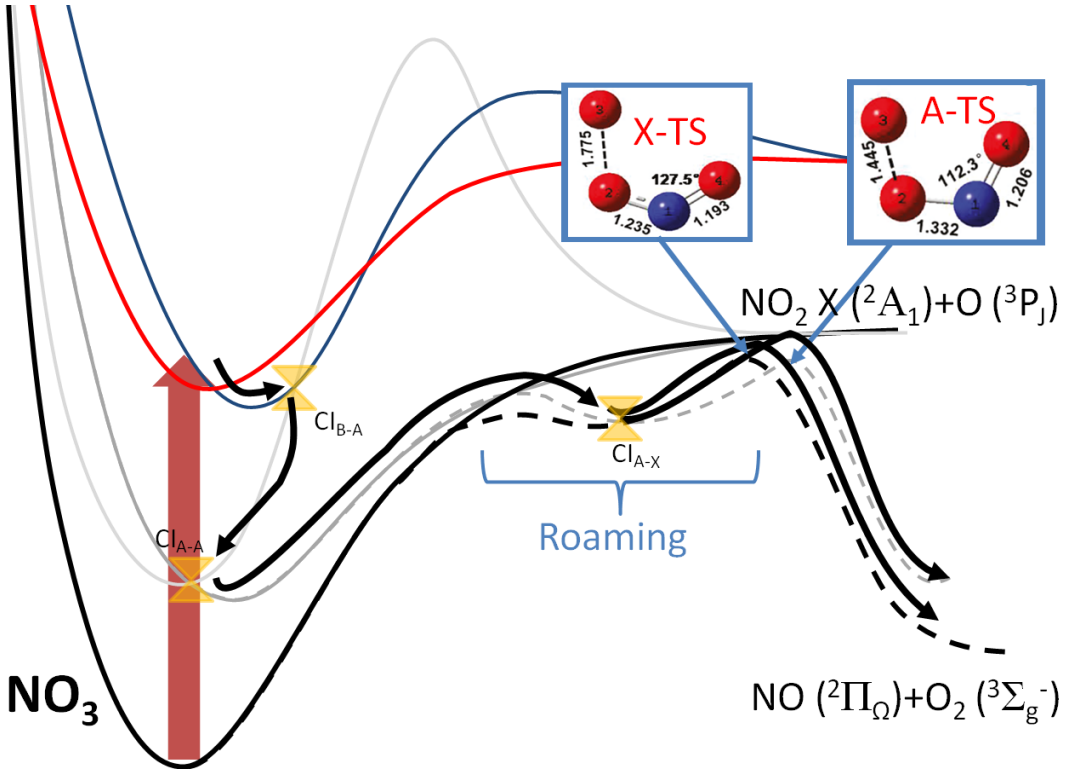

Figure 30: Schematic diagram of dissociation mechanism proposed by Xiao et al. [60] The nuclear geometries of the ONO-O transition state of each channel is shown in the inset.

Ab initio classical trajectory calculations were performed starting from transition states for the O_2 elimination on the dark state and ground state PESs by using the Born-Oppenheimer molecular dynamics (BOMD) model, in combination with DFT methods. The results from the trajectories on the dark state produce vibrationally cold O_2, while the trajectories on the ground state produce vibrationally excited O_2. These results indicate that *both* reaction pathways may be due to the roaming mechanism, on a bifurcated potential energy surface.

This result was unexpected, and would make $NO_3 \rightarrow NO + O_2$ photodissociation the first observed reaction without a traditional transition state pathway. Furthermore, this would be the first roaming reaction to access multiple excited states. We therefore endeavored to obtain experimental proof of this intriguing mechanism.

D. Λ doublet propensities

An experimental test of this two-state roaming theory requires that a signature of the dissociative electronic state be retained in the photofragments. Electronic symmetry must be conserved for chemical processes, and thus the electronic orbital symmetry in NO_3 should be maintained in the product fragments. If this orbital symmetry can be measured in the fragments and compared to the calculated orbital occupancies of the NO_3 molecule in the exit channel of both electronic potentials, the electronic state origin of each pathway can be revealed.

The orbital symmetry of a diatomic molecule in a $^2\Pi$ electronic configuration such as the ground state of NO is described by its propensity for one of the two Λ doublet states: $^2\Pi$ (A") or $^2\Pi$ (A'). A $^2\Pi$ (A") Λ doublet propensity indicates the singly occupied $p\pi$-orbital lobe is oriented orthogonal to the fragment rotational plane, whereas an $^2\Pi$ (A') Λ doublet propensity indicates the lobe is oriented along the fragment rotational plane. A classic example of the use of Λ doublet propensities in deciphering photodissociation dynamics is found in another atmospheric molecule: water.

One of the most fascinating aspects of the photodissociation of water in the first absorption band is its strong preference for producing OH fragments in the upper Λ doublet state, the stimulated emission of which has been proposed as an origin for

interstellar masers.[61] The origin of this Λ doublet preference however is quite easily understood when put in the context of electronic symmetry conservation.[62] The absorption of a photon leads to an excited electronic state of water characterized by an unpaired electron in an out of plane *pπ*-orbital lobe. When the molecule dissociates, the orbital orientation is preserved in the resulting OH fragment and the *pπ*-orbital lobe containing the unpaired electron must be oriented out of its rotational plane (the $^2\Pi$ (A") Λ doublet state). Conversely, dissociation of water on the ground potential surface via the O (^{1}D) + $H_2 \rightarrow H_2O \rightarrow$ OH + H reaction yields the opposite Λ doublet products.[63] The unpaired electron in the OH molecule forms a H-OH *s*-*p* sigma bond in the ground state of water, and thus the *pπ*-orbital lobe remains oriented in the OH rotational plane (the $^2\Pi$ (A') Λ doublet state) after the bond fractures.[62] The correlation between Λ doublet propensities and electronic origin provides a convenient route toward distinguishing pathways on different electronic potentials, provided the electronic states have different electronic symmetries.

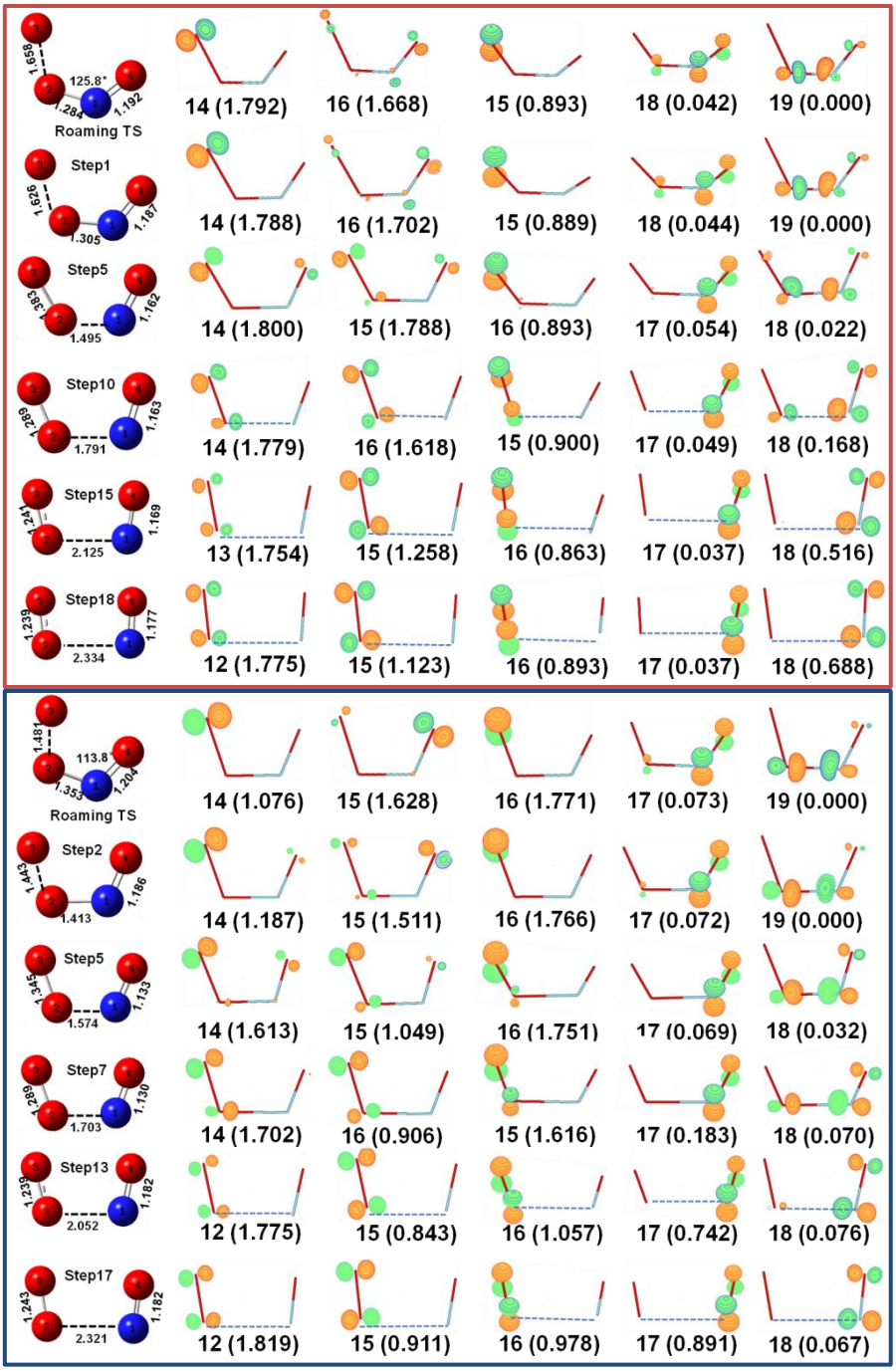

Figure 31: Evolution of the key electronic orbital in the NO_3 exit channel derived from the CASSCF calculations. Some representative structures in the exit channel after the roaming transition state on both the ground (upper) and first excited (lower) electronic potentials by Maeda and coworkers.[60] The occupancy of the orbital is shown at each step in parentheses. In plane dissociation results in opposite NO Λ doublet propensities for the two pathways.

Ab initio calculations were performed on the NO_3 system to determine the evolution of the electronic orbitals in the NO_3 exit channel, in order to predict the preferred Λ doublet state arising from each electronic state potential surface. These orbitals were obtained by CASSCF calculations and calculated for some representative structures along the reaction pathways determined in our previous study.[60] The results shown in Figure 31 support in-plane dissociation on both surrfaces, and conveniently predict opposite Λ doublet propensities for each pathway. The *pπ*-orbital lobe in the NO fragment containing the unpaired electron lies in the NO rotational plane ($^2\Pi$ (A') Λ doublet state) for trajectories evolving on the ground state of NO_3, whereas the lobe is perpendicular to the NO rotational plane ($^2\Pi$ (A") Λ doublet state) for trajectories evolving on the dark state of NO_3. Thus experimental measurements of the NO Λ doublet propensities should show an A' preference for Pathway A and an A" preference for Pathway B, if the two-state dissociation model is correct.

Experimentally, the two Λ doublet states can be preferentially probed through optical transitions of different rotational branches. Classically, the transition dipole moment of an $R^{(N)}$ or $P^{(N)}$ branch transition lies in the molecular plane of rotation, since the electric field from the photon must act upon the nuclear dipole moment to change its rotational angular momentum quantum number by ± 1 (here we refer to N, the angular momentum aside from the electron spin, instead of the total angular momentum J which is not necessarily normal to the rotational plane). Conversely, the transition dipole moment of a $Q^{(N)}$ branch is orthogonal to the molecular plan of rotation, resulting in no net change in rotational angular momentum. The transition dipole of the A ← X

transition in NO, the resonant step of our two photon REMPI detection sceme, is defined by the same *pπ*-orbital lobe which characterizes the NO Λ doublet state, leading to preferential absorption from the $^2\Pi$ (A") Λ doublet for $Q^{(N)}$ branch (ΔN=0) transitions and the $^2\Pi$ (A') Λ doublet for $P^{(N)}/R^{(N)}$ branch (ΔN±1) transitions. This preferential absorption can also be understood by the **(+ ←→ -)** symmetry selection rule, as shown in Figure 32. Λ doublet preferences of NO photoproducts are therefore typically characterized by the ratio of $Q^{(N)}$ and $P^{(N)}/R^{(N)}$ branch line intensities in optical spectra.[64-65] Laser-induced fluorescence measurements of NO originating from NO_3 photodissociation in a molecular beam have been previously conducted by Wittig and coworkers, who observed a "slight" overall propensity of the $^2\Pi$ (A') Λ doublet state, although this propensity appears to fluctuate as a function of NO J.[5] However, because there are two Pathways to NO products and each one has an opposite Λ doublet preference, the Λ doublet propensity cannot be measured simply by optical intensities as the signal bias from each pathway will be anti-correlated and the total observed signal intensity will not change significantly.

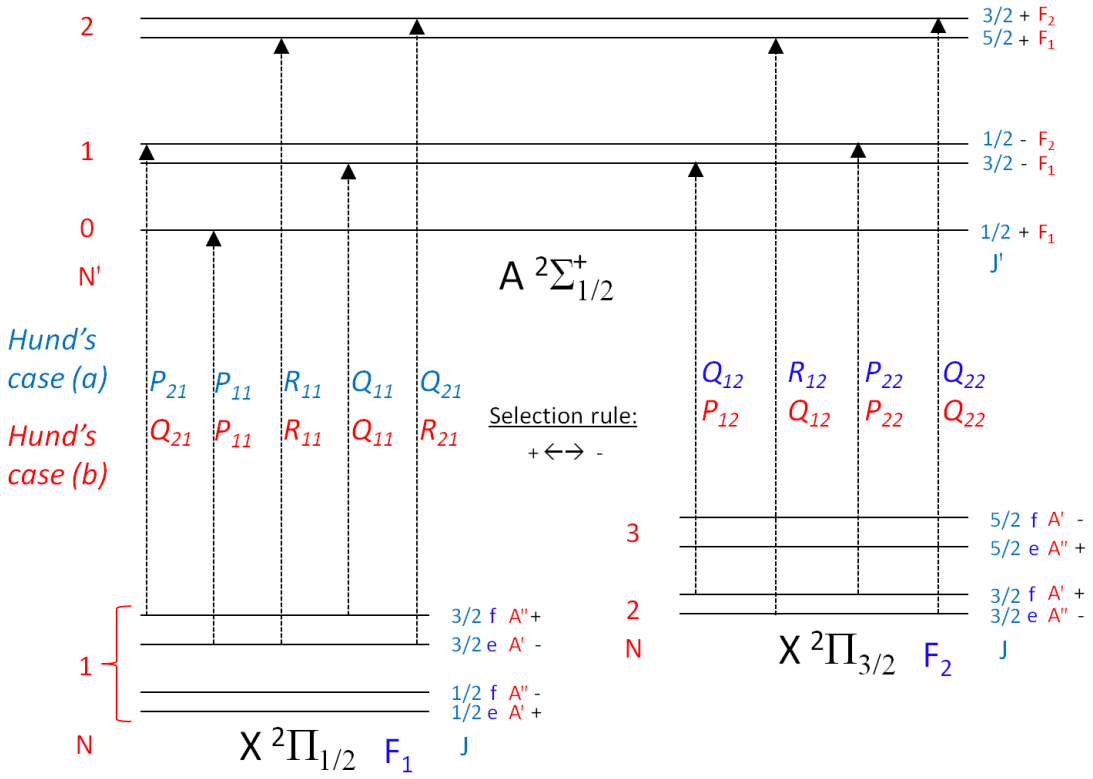

Figure 32: Lowest lying A ← X rotational branch transitions in NO. Due to parity selection rules, the Hund's case (b) (ΔN) $Q^{(N)}$ branch transitions only originate from the $^2\Pi$ (A'') Λ doublet states, while the $P^{(N)}/R^{(N)}$ branch transitions only originate from the $^2\Pi$ (A') Λ doublet states.

In ion imaging experiments, the NO resulting from both dissociation pathways is measured simultaneously and differentiated via their center-of-mass velocities. Comparing the total signal of each pathway between two ion images probed via $Q^{(N)}$ and $R^{(N)}/P^{(N)}$ branches is challenging, due to fluctuating beam conditions and other experimental variables, and thus an absolute Λ doublet propensity value is difficult to measure via ion imaging. However, the *relative* Λ doublet propensity of the two pathways can be obtained easily, and accurately, from the ratios of each channel when the NO is probed via different rotational branch transitions. The fractional yields of

pathways A and B for a particular ion image are given by χ_A and χ_B respectively. The observed fractional yields however, are also a function of the Λ doublet propensity of each pathway, c_A^Λ and c_B^Λ, which represent the fractional yield of the $^2\Pi$ (A") Λ doublet for each pathway. The observed relative intensity of the two pathways in a $Q^{(N)}$ branch ion image, which probes the $^2\Pi$ (A") state, is given by:

$$R_{A:B}^{Q} = \frac{\chi_A c_A^\Lambda}{\chi_B c_B^\Lambda} \tag{5.3}$$

And the relative intensity of the two pathways in a $P^{(N)}$ or $R^{(N)}$ branch ion image, which probes the $^2\Pi$ (A') state, is given by:

$$R_{A:B}^{P,R} = \frac{\chi_A\left(1-c_A^\Lambda\right)}{\chi_B\left(1-c_B^\Lambda\right)} \tag{5.4}$$

The ratio of the relative intensities for the two branches yields the relative Λ doublet ratios for the two pathways.

$$\frac{R_{A:B}^{Q}}{R_{A:B}^{P,R}} = \frac{c_A^\Lambda}{\left(1-c_A^\Lambda\right)} \cdot \frac{\left(1-c_B^\Lambda\right)}{c_B^\Lambda} = \frac{R_{A''_{:}A'}^{A}}{R_{A''_{:}A'}^{B}} \tag{5.5}$$

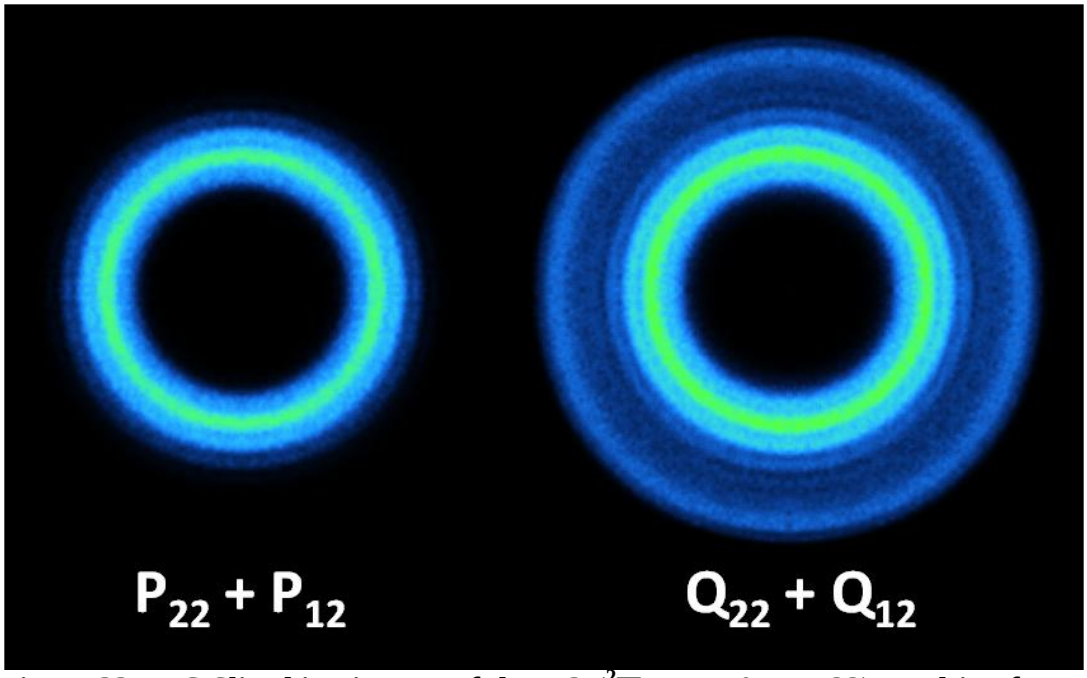

Figure 33: DC Sliced ion images of the NO ($^2\Pi_{3/2}$; v = 0; N = 22) resulting from NO_3 photodissociation at 588 nm probed via P and Q branch transitions. The maximum intensity of each image has been normalized to approximately the same value for the sake of comparison. The inner rings observed in both images arise from pathway A, while the outer rings which appear suppressed in the P branch image arise from pathway B.

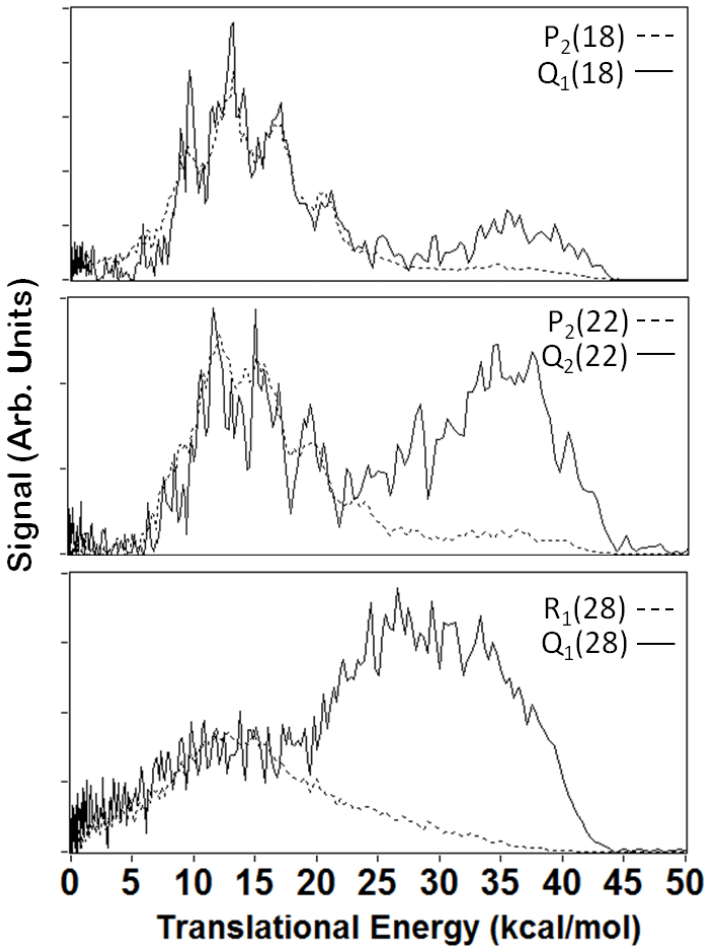

Figure 34: Total translational energy distributions derived from NO ($^2\Pi_\Omega$; v = 0; N = 18, 22, 28) fragment ion images resulting from NO_3 photodissociation at 588 nm probed via both the $P^{(N)}/R^{(N)}$ (dashed) and $Q^{(N)}$ (solid) branches. Differences in the relative intensity between the two channels indicate a Λ doublet propensity. Each pair of ion images is normalized to preserve the peak intensity of the low energy channel for visual comparison.

Ion images of the same quantum state of NO probed via different rotational branches are shown in Figure 33, and reveal noticeable qualitative differences between the relative intensities of the two pathways. Figure 34 shows the translational energy distributions derived from ion images of various NO rotational quantum numbers,

probed via both the $P^{(N)}/R^{(N)}$ and $Q^{(N)}$ branches. The differences in the relative intensities are dramatic, suggesting large and opposite Λ doublet propensities for the two pathways, which rapidly increase as N grows from 18 to 28. Pathway A shows an increased relative propensity in the $P^{(N)}/R^{(N)}$ branch images, indicating a $^2\Pi$ (A') Λ doublet preference, whereas Pathway B shows an increased relative propensity in the $Q^{(N)}$ branch images, indicating a $^2\Pi$ (A") Λ doublet preference. These are the same Λ doublet preferences predicted by the orbital occupancy calculations, providing strong evidence for multi-state roaming.

The ratio of the relative intensity of the two pathways for the $Q^{(N)}$:$P^{(N)}/R^{(N)}$ branch images as a function of N is provided in Figure 35. Isolated spectral lines for both the $Q^{(N)}$ and $P^{(N)}/R^{(N)}$ rotational branches were obtained for four N values (13, 18, 22, and 28) spanning the range of the NO rotational distribution where both Pathways are observed.

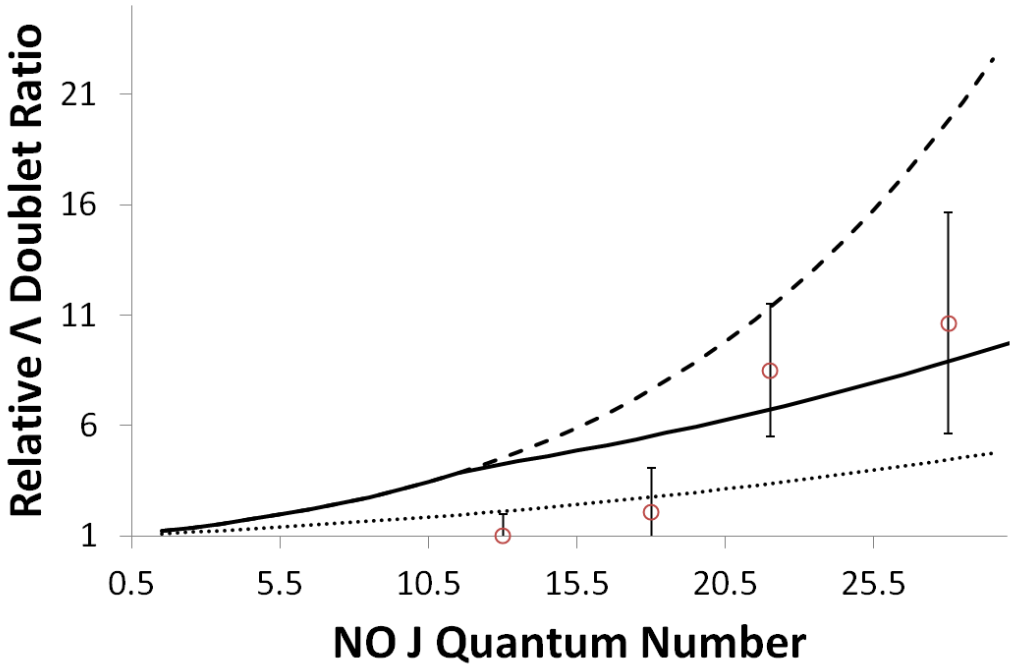

Figure 35: Relative Λ doublet ratios of the NO (v=0) fragment originating from Pathways A and B from 588 nm photolysis of NO_3, obtained from $P^{(N)}/R^{(N)}$ and $Q^{(N)}$ branch experimental images. The large error bars arise from uncertainty in assignment of the signal at intermediate velocities where the signal from both pathways overlap, and the inherent sensitivity of relative measurements. The dotted line shows the expected ratio arising from a maximum Λ doublet propensity in a single pathway, and the dashed line shows the expected ratio from a maximum Λ doublet propensity in both pathways. The solid line shows the result of a maximum $^2\Pi$ (A'') Λ doublet propensity for Pathway B, and a statistical 2:1 $^2\Pi$ (A') Λ doublet propensity for Pathway A.

Although the relative measurement does not appear to directly reveal whether the observed propensities arise from Pathway A, B, or both, the magnitude of the relative propensities can in fact only be obtained when large and opposite Λ doublet propensities are present in both pathways. This is consistent with a model where Pathway A arises

from ground state dissociation, and Pathway B arises from dissociation on the first excited state.

The maximum Λ doublet propensity is governed by the degree to which the orbital angular momentum and nuclear rotation are coupled, and therefore the Λ doublet states are only well defined at larger values of J. As the rotational energy of the molecule increases, electronic orbital angular momentum begins to uncouple from the NO bond axis and begins to couple to the nuclear rotation axis. This effect is proportional to the ratio of the spin-orbit coupling parameter A_v and the rotational constant B_v. The maximum Λ doublet propensity is given by the following equation:[66]

$$c_{max}^{\Lambda} = 0.5 + \left[4 + \frac{\left(\frac{A_v}{B_v} - 2\right)^2}{\left(J+\frac{3}{2}\right)\left(J-\frac{1}{2}\right)}\right]^{-\frac{1}{2}} \tag{5.6}$$

From this equation, the limiting values of the relative Λ doublet ratios for the two pathways at a particular NO J quantum number can be obtained. In Figure 5, the maximum relative Λ doublet ratio is shown assuming that only one pathway possesses a Λ doublet preference (dotted line), and assuming that both pathways possess opposite Λ doublet preferences (dashed line). It is clear that the experimental observations cannot arise from an NO Λ doublet propensity for only one of the two pathways.

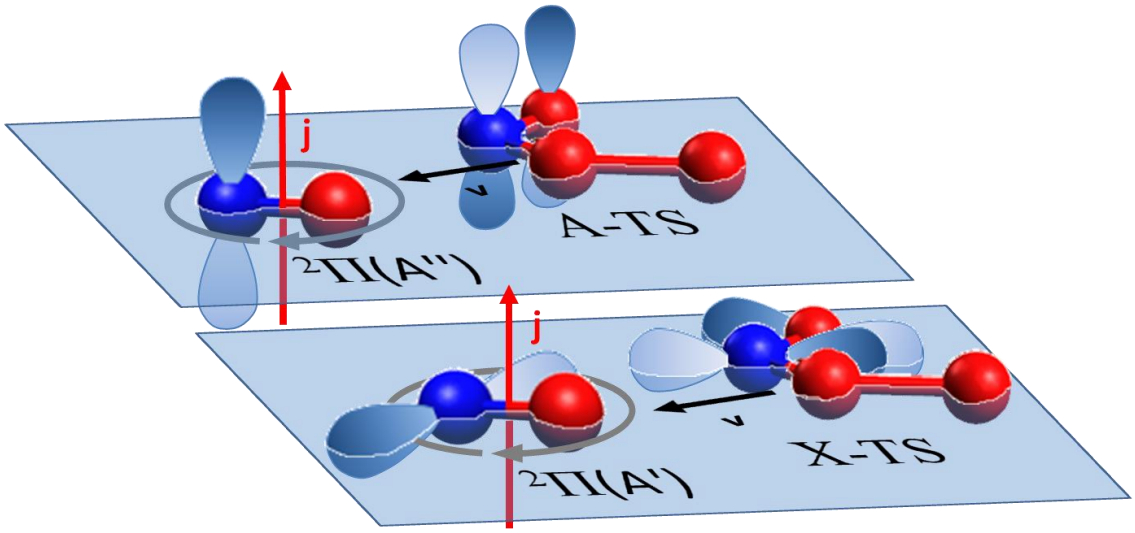

Figure 36: Schematic diagram illustrating the electronic orbital containing the unpaired electron in the X and A electronic states of NO_3 at the roaming transition states, and in the resulting NO fragment. The electronic symmetry of the parent is maintained in the NO fragment, resulting in distinct NO Λ doublet states for trajectories originating from the two NO_3 electronic potentials.

It is important to note that the predicted Λ doublet preferences for the two electronic states only arise from dissociation constrained to the molecular plane (Figure 36). If the NO fragment is ejected with a statistical distribution of velocities and angular momentums, a 2:1 preference for the $^2\Pi$ (A') Λ doublet would be expected for both pathways (since the orbital is constrained to the two-dimensional xy plane as opposed to a one-dimensional z axis). The question may then arise whether the observed $^2\Pi$ (A') Λ doublet preference in Pathway A is due to dynamic constraints, as we propose, or due to a statistical unconstrained dissociation. A model assuming a maximum $^2\Pi$ (A'') Λ doublet propensity for Pathway B and a statistical $^2\Pi$ (A') Λ doublet propensity for Pathway A is shown as the solid line in Figure 35, and is also consistent with our results. To investigate this question, we performed additional experiments to look for evidence

of dynamical constraints in the dissociation process by measuring fragment vector correlations, specifically the **v-j** correlation which should be perpendicular for planar dissociation.

E. Vector correlations

Dynamical constraints in photodissociation are manifested in the correlations between the $\boldsymbol{\mu}_{\mathbf{par}}$, **v**, and **j** vectors, as detailed in Chapter IV. The transition dipole moment of the B ← X transition of NO_3 lies in the molecular plane, and thus prompt planar dissociation would give rise to a $\boldsymbol{\mu}_{\mathbf{NO3}}\|\mathbf{v}$ correlation. However, NO_3 has a long dissociative lifetime relative to its rotational period,[12] and thus all correlations between $\boldsymbol{\mu}_{\mathbf{NO3}}$ and the product vectors are sufficiently depolarized in the laboratory-frame that they cannot be experimentally observed.[16] However, this does not eliminate correlations between fragment **v** and **j** which are a result of torques in the exit channel created at the moment of dissociation, and will be observed independent of the dissociation lifetime. If the roaming oxygen atom abstraction is limited to the molecular plane, the rotation of the NO and O_2 fragments should also lie in the molecular plane, resulting in $\mathbf{v}\perp\mathbf{j}$ correlations in the two fragments. In contrast, if the oxygen atom is abstracted from an unconstrained set of angles, or the fragment velocity vector is statistically distributed, no **v-j** correlation will be observed. This is the predicted result of roaming dynamics, which has been characterized by loose abstraction geometries. Indeed, previous Doppler measurements of the photoproducts originating from the methyl fragment roaming channel of acetaldehyde photodissociation detected no **v-j**

correlations in the CO fragment,[67] and unconstrained abstraction geometries were observed in theoretical trajectory calculations of formaldehyde.[68]

Since there are no lab-frame $\boldsymbol{\mu_{NO3}}$ correlations, the **v-j** correlation alone contributes to the observed image anisotropy, and can be easily determined from a single ion image. As mentioned earlier, the transition dipole moment $\boldsymbol{\mu_{NO}}$ is parallel to **j** for a Q branch transition ($\Delta J = 0$), and perpendicular to **j** for an R or P branch transition ($\Delta J \pm 1$). Therefore, if the electric field $\boldsymbol{E}$ of the probe laser is polarized vertically in the plane of the image, and if there is some sort of correlation between **v** and **j** (and thus $\boldsymbol{\mu_{NO}}$), fragments recoiling in different lab-frame directions will be detected with different efficiencies ($I = |\boldsymbol{E} \cdot \boldsymbol{\mu_{NO}}|^2$) resulting in an anisotropic distribution of signal in the ion image. However, if the probe laser is polarized normal to the image plane, $|\boldsymbol{E} \cdot \boldsymbol{\mu_{NO}}|$ will be independent of the fragment velocity in the 2D-image plane and the ion image should always be isotropic in the absence of other vector correlations.

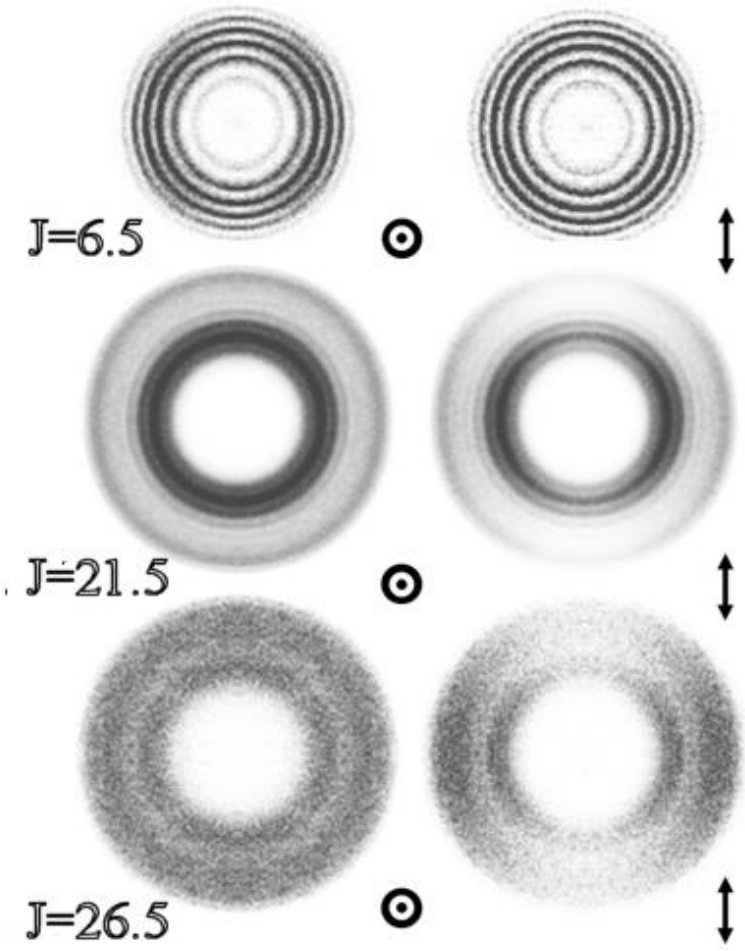

Figure 37: DC Sliced ion images of NO ($^2\Pi_\Omega$; v = 0; J = 6.5, 21.5, 26.5) fragments produced from NO_3 photodissociation at 588 nm, using two different probe laser polarizations to reveal vector correlations. The out-of-plane probe polarization (left panel) produces isotropic images, while the in-plane probe polarization (right panel) gives rise to signal anisotropy originating from the v-j correlation.

Figure 37 shows ion images of three different NO rotational states ($^2\Pi_\Omega$; v = 0; J=6.5, 21.5, and 26.5) probed via a Q branch transition. The images were obtained at two different probe laser polarization geometries, with the electric field polarized either perpendicular to the image plane, which should result in an isotropic signal distribution,

or parallel to the imaging plane, where any image anisotropy originates from the **v-j** correlations. The **v-j** correlation is quantified by the $\beta_0^0(22)$ parameter of Dixon, and represents the expectation value $\langle P_2(\cos\ \theta_{vj})\rangle$, where θ_{vj} is the angle between the **v** and **j** vectors. The $\beta_0^0(22)$ parameter ranges from -0.5 when **v** and **j** are orthogonal, to 1.0 when **v** and **j** are parallel. No dependence of the signal on the pump laser polarization was found for any of the images, confirming the lack of detectable $\boldsymbol{\mu_{NO3}}$ correlations. Therefore, the **v-j** correlation parameter, $\beta_0^0(22)$, can be obtained directly from the anisotropy of the image acquired when the probe laser is polarized in the image plane (Derived from Eq. 4.5):

$$\beta_2^{F\updownarrow} = 2h^{(2)}\beta_0^0(22) \tag{5.7}$$

As a rigorous test of the validity of our zero $\boldsymbol{\mu_{NO3}}$ correlations assumption, we have determined all of the vector correlations detailed in Chapter IV (**μ-v, μ-j, v-j,** quadratic **μ-v-j,** and quartic **μ-v-j**) for the NO (J=26.5) fragment from images of all three different laser geometries using the complete Equations 4.7a-4.7d. The results of this are shown in Figure 38, and verify the **v-j** correlation is the only significantly non-zero term.

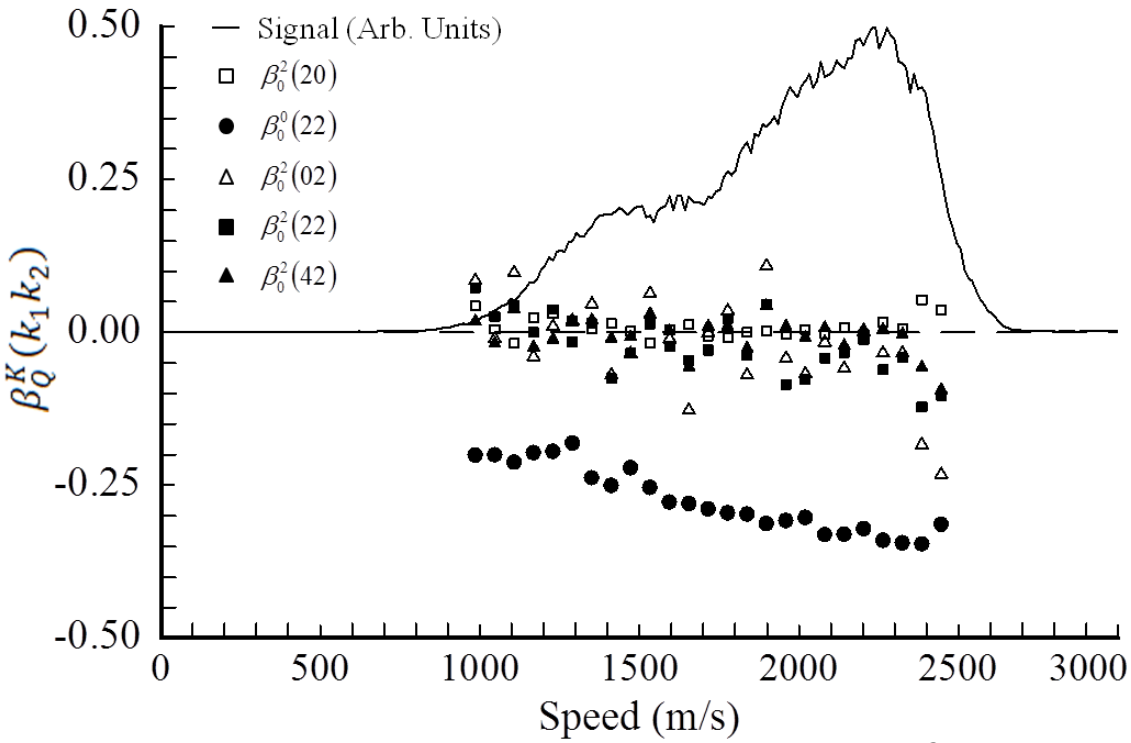

Figure 38: All five possible vector correlations as a function of NO ($^2\Pi_{1/2}$; v=0, J=26.5) recoil speed. Obtained using 60 m/s bins via the equations provided in reference [16]. All of the correlations are effectively zero, except for the v-j correlation $\boldsymbol{\beta_0^0(22)}$. The total translational energy distribution is shown as the solid line, with an arbitrary intensity scale.

Although no **v-j** correlation is observed for low J NO fragments, the images reveal the presence of strong **v⊥j** correlations in the higher J fragments (J ≥ 18.5). At large values of J, there is overlap in the signal associated with Pathway A and Pathway B, which complicates the extraction of Pathway specific **v-j** correlations. Fortunately, the observed Λ doublet propensities provide a convenient method for deconvoluting the signal originating from the two pathways. By probing a P/R branch image, the signal originating from Pathway A can be enhanced, despite the low yield of this pathway at high NO J states.

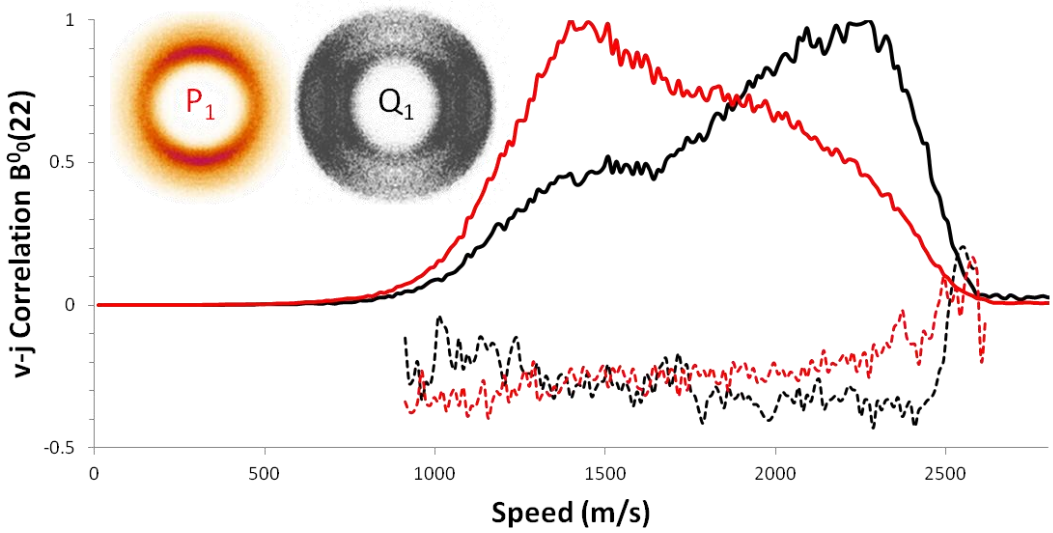

Figure 39: Speed distribution and speed dependent v-j correlation parameter $\beta_0^0(22)$ for NO ($^2\Pi_{1/2}$; v = 0; J=26.5) probed via a Q branch transition and NO ($^2\Pi_{1/2}$; v = 0; J = 29.5) probed via a P branch transition resulting from NO_3 photodissociation at 588 nm. The negative values of $\beta_0^0(22)$ indicate a v⊥j correlation. The two raw sliced ion images are shown in the inset.

Figure 39 shows the **v-j** correlation parameter, $\beta_0^0(22)$, as a function of the NO recoil speed for ion images probed via the $P_1(29.5)$ transition which is dominated by Pathway A (>70%) and the $Q_1+P_{21}(26.5)$ transition which is dominated by Pathway B (>80%). Analysis of both images results in approximately identical average **v⊥j** correlations. A slight speed dependence in the **v-j** correlation is observed, with an opposite trend detected when the different rotational branches are probed. It is unclear at this time whether these subtle trends are related to the Λ doublet bias of the two branches, or an unknown experimental effect.

The averaged, speed-independent **v-j** correlation, $\langle\beta_0^0(22)\rangle$, is shown in Figure 40 as a function of the NO(v = 0) total angular momentum quantum number, J. The

values are averaged over both pathways, as both Pathway A and Pathway B yield similar $\beta_0^0(22)$ values. We find that the $\langle\beta_0^0(22)\rangle$ parameter decreases abruptly from near 0 to values around -0.30±0.1 between NO J quantum numbers of 12.5 and 18.5, and then remains nearly constant as J increases. Conservation of angular momentum and energy often results in increasing **v-j** correlations with increasing fragment J. The constant value observed here may be an indication that the **v⊥j** correlations are due primarily to exit channel dynamics, and not simply angular momentum conservation**.** It should also be noted that even the maximum detected NO J state accounts for less than 10% of the available energy in the dissociation.

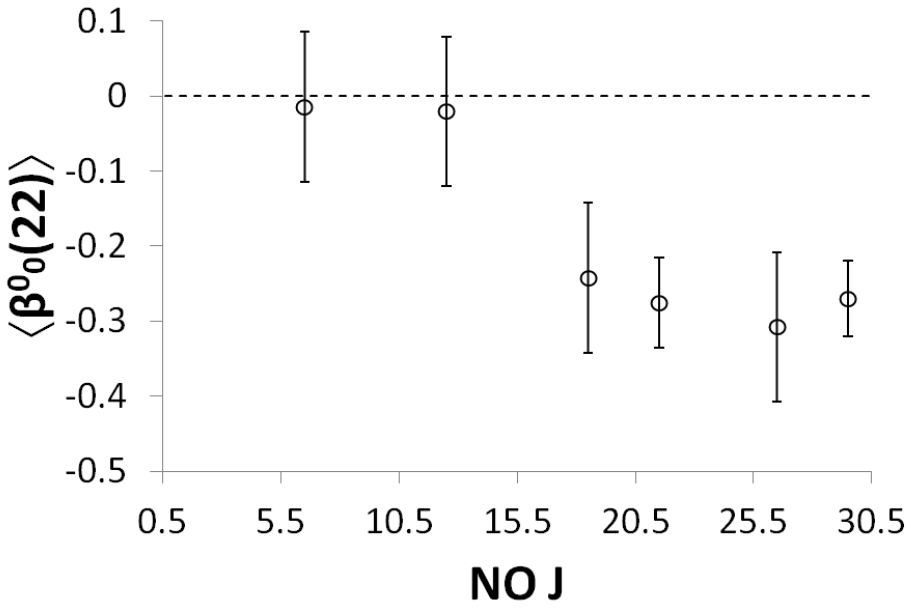

Figure 40: Average v-j correlation $\langle\beta_0^0(22)\rangle$ as a function of NO (v=0) total angular momentum quantum number, J.

The strong $\mathbf{v}_{\perp}\mathbf{j}$ correlation observed in the NO fragment in both channels is consistent with dissociation in the molecular plane, as shown in Figure 36. Additional evidence for this model lies in the highly correlation between the NO and O_2 rotational distributions, which we reported in Chapter V.A to be larger than statistically predicted for both pathways. This would be expected from an in-plane dissociation where large opposite torques should be generated in both fragments.

The sudden onset of the **v-j** correlation at NO (J=18.5) is intriguing, and corresponds to the states when Pathway B is first observed in the images. However, as we have shown, both pathways exhibit approximately equivalent **v-j** correlations. The onset of the **v-j** correlations also coincides with a large increase in the rotational distribution of the O_2 cofragment. This may imply that the low J NO signal we observe arises from a subset of trajectories on the ground state surface (Pathway A) where the abstraction is not constrained to the molecular plane.

The clear experimental observation of directed torques in the roaming dynamics of NO_3 dispels previous speculation about unconstrained abstraction and a lack of **v-j** correlation to be a signature of the roaming mechanism.[69] This should not be unexpected, as roaming dynamics are analogous to the corresponding bimolecular reaction, which may or may not possess geometrical constraints and strongly directed torques.[70] Based on our measurements, we would predict similar stereodynamics in $NO_2 + O \rightarrow NO + O_2$ reactive scattering.

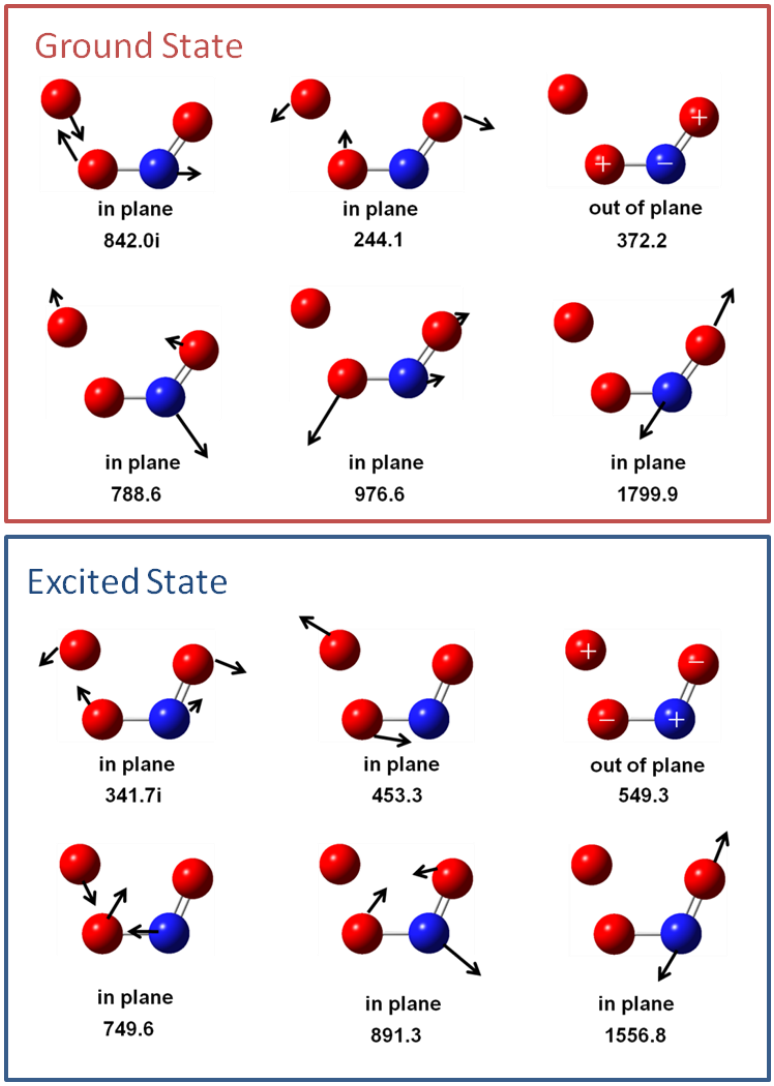

Figure 41: Vibrational modes and frequencies of the ground and excited state roaming transition states. Frequencies are given in wavenumbers (cm^{-1}). The length of the arrow indicates vibrational strength, and the "+" and "-"denote the out of plane motion of the atoms.

Theoretical vibrational analysis performed by Maeda and coworkers provides additional explanation for the unconstrained abstraction geometries observed for formaldehyde photodissociation. There are two known transition states (first-order saddle points) in the exit valley of the roaming pathway of H_2CO;[71-72] one has a non-

planar geometry and another is planar. In contrast to H_2CO, in NO_3 the saddle points in both of the two electronic states have planar geometry.

Furthermore, the planar saddle point for H_2CO has a very low frequency out-of-plane mode; the frequency is only 32 cm^{-1} at the UCCSD/aug-cc-pVDZ level.[72] However, out-of-plane modes at the saddle points of NO_3 have relatively high frequencies of 549 cm^{-1} and 372 cm^{-1} in the first excited and ground states, respectively, at the 3S-(11e, 8o) CASPT2/6-31+G* level (Figure 41); these high out-of-plane frequencies imply that a majority of roaming trajectories are confined to planar geometries when they go through the bottleneck of the exit valley. Thus, planar roaming trajectories likely dominate in NO_3, in contrast to H_2CO.

The reaction coordinates (denoted by an imaginary frequency in Figure 41) obtained through this vibrational analysis is also worth noting. The reaction coordinate for the excited state is characterized by counter-rotation in the two fragments, consistent with the larger observed angular momentum of the products resulting from this pathway.

CHAPTER VI

THE RESOLUTION: CONCLUSIONS AND FUTURE WORK

"There are two possible outcomes: if the result confirms the hypothesis, then you've made a measurement. If the result is contrary to the hypothesis, then you've made a discovery."

-Enrico Fermi

The combined theory and experiments described in Chapter V provide us with a detailed picture of the long mysterious $NO_3 \rightarrow NO + O_2$ photolysis reaction, which is the first observed reaction to occur entirely via the roaming mechanism.

Roaming in NO_3 is initiated by a frustrated atomic elimination at photolysis energies just below the $NO_3 \rightarrow NO_2 + O$ asymptote (< 1 kcal/mol), where the N-O bond does not have the energy to break. The loosely bound oxygen atom slowly "roams" about the rest of the molecule, exploring a large and flat region of the potential energy surface. Eventually, it encounters a reactive site and abstracts another oxygen atom, creating O_2 and NO. Our experiments reveal several unique facts about this mechanism.

First, oxygen atom roaming in NO_3 takes place on both the ground X ($^2A'_2$) and first excited A ($^2B_1$) electronic potentials as evidenced by experimental relative Λ doublet propensities. The magnitude of the measured relative Λ doublet ratios implies that NO originating from both Pathway A and Pathway B possess strong and opposite Λ doublet propensities. Pathway A shows a preference for producing the $^2\Pi$ (A') Λ doublet state, while Pathway B shows a preference for producing the $^2\Pi$ (A") Λ state. This is consistent with the interpretation of previous orbital occupancy calculations of

the X ($^2A'_2$) and A ($^2B_1$) states in the roaming exit channel, which were calculated to give rise to $^2\Pi$ (A') and $^2\Pi$ (A") NO Λ doublet states respectively. The presence of $\mathbf{v}\perp\mathbf{j}$ correlations implies that the $^2\Pi$ (A') propensity in Pathway A is not due to statistical arguments, but due to orbital symmetry conservation in a dynamically constrained dissociation.

Additionally, the observation of strong $\mathbf{v}\perp\mathbf{j}$ correlations in the NO arising from both Pathway A and Pathway B combined with theoretical calculations of the ONO-O transition state geometries show that the exit channel dynamics are constrained to the molecular plane. No **v-j** correlations have been observed in prior roaming systems, and unconstrained dynamics has formerly been put forward as a signature of roaming behavior.[67, 69] The photolysis dynamics of NO_3 has revealed that this is not correct. Roaming has been referred to as an intra-molecular abstraction, and we find that this description is very much the case. The roaming abstraction will only be unconstrained if the corresponding bi-molecular reaction is unconstrained, and we hypothesize that the $NO_2 + O \rightarrow NO + O_2$ reaction requires similar abstraction angles to what we observe here. Studies of this reaction in a cross-beam experiment would therefore be instructive towards understanding the relationship between the two processes.

Despite considerable progress towards elucidating the photoinduced dissociation dynamics, a few questions remain. Our asymptotic experimental measurements are primarily sensitive to the dynamics in the exit channel, and thus the complete dynamical evolution of the system from the Franck-Condon region to the products is still unclear. Although it is known that the absorption of visible light initially populates the ‘bright’ B

(^{2}E") state of NO_3, it is less certain whether the reaction the proceeds through the ground state, the first excited state, or both. Strong linear Pseudo-Jahn-Teller (PJT) vibronic coupling with the higher vibrational levels of the ground state mediated by the asymmetric bending and stretching modes suggests initial coupling to the X (^{2}A'$_2$) state,[49-50] while the theoretical calculations of Xiao et al. have suggested direct coupling to the A (^{2}A$_2$) and then A (^{2}B$_1$) state.[60] Both the ground X (^{2}A'$_2$) state and the first excited A (^{2}B$_1$) are asymptotically correlated to the NO_2 X (^{2}A$_1$) + O (^{3}P$_J$) products, and therefore roaming may occur on one or both of these potentials. Morokuma and co-workers have identified a conical intersection (CI_{A-X}) between the two potentials in the roaming region just before oxygen atom abstraction, where the molecular structure resembles ONO-O.[60] The curve-crossing probability associated with CI_{A-X} is largely dependent on which potential the trajectory originates. Based on previous work,[73] and the photofragment translational spectroscopy work of Davis and Lee,[18] approximately ~80% of the total NO + O_2 products proceed by Pathway A via the ground state transition state (X-TS),and ~20% proceeds by Pathway B via the excited state transition state (A-TS). Therefore, if CI_{A-X} is approached on the ground X (^{2}A'$_2$) state potential, the surface crossing probability to the A (^{2}B$_1$) state is 20%. However, if CI_{A-X} is approached on the excited A (^{2}B$_1$) state potential, the surface crossing probability to the X (^{2}A'$_2$) is 80%. Furthermore, if CI_{A-X} is approached on *both* electronic surfaces, the crossing may be ignored entirely. Clearly, additional theoretical studies are warranted to distinguish between these surface crossing possibilities.

The question arises of whether roaming reactions are more or less prone to non-adiabatic surface crossing in the exit channel than conventional dissociation dynamics. Roaming-type mechanisms sample a large area of the potential energy surface in the flat asymptotic region of the surface where the electronic potentials converge, and thus may often involve multistate dynamics. It is therefore intriguing that no other system exhibiting roaming behavior has shown any evidence of excited state dynamics. The majority of roaming molecules identified, however, have been close-shelled. Open-shelled molecules such as NO_3 possess many low-lying excited states approaching the same product asymptotes, and multi-state roaming should be more likely for radical molecules. One example of a radical molecule where multi-state roaming is likely to play a role in the photolysis mechanism is CH_2NO_2, which dissociates into NO + H_2CO via a currently unknown mechanism.[74] The similar electronic structure CH_2NO_2 to NO_3 may indicate a similar multi-state roaming mechanism is occurring. Ion imaging studies on this system and other radical molecules may be instructive toward answering some of these questions, and the answers may hold important implications concerning the nature of roaming and excited state chemistry.

A related question is: is there any difference between the outcome of roaming and the corresponding direct abstraction reaction? We have stated previously that the two processes have been shown to be analogous in the formaldehyde system, although in that case roaming occurs only on a single potential surface.[56] Careful measurements of the product distributions resulting from the bimolecular $NO_2 + O \rightarrow NO + O_2$ reaction would determine if this is also the case for the NO_3 system where there is the possibility

of multi-state roaming. The bimolecular reaction has been shown to proceed either via direct abstraction (60%), or by first forming an excited complex (40%).[57] If the direct abstraction reaction also accesses the excited state pathway, the resulting product distribution should match the outcome of our photolysis experiments. However, if the direct abstraction reaction does *not* access the excited state pathway, a significantly lower population of the lower vibrational quantum numbers of O_2 will be observed.

REFERENCES

[1] J. Chappuis, Annales Scientifiques de l'E.N.S. **11,** (1881).

[2] Miller, Terry. Private Correspondance, (2011).

[3] H. S. Johnston, H. F. Davis, and Y. T. Lee, J. Phys. Chem. **100,** 4713 (1996).

[4] F. Magnotta, and H. S. Johnston, Geophys. Res. Lett. **7,** 769 (1980).

[5] K. Mikhaylichenko, C. Riehn, L. Valachovic, A. Sanov, and C. Wittig, J. Chem. Phys. **105,** 6807 (1996).

[6] R. D. Vanzee, M. F. Foltz, and C. B. Moore, J. Chem. Phys. **99,** 1664 (1993).

[7] D. Townsend, S. A. Lahankar, S. K. Lee, S. D. Chambreau, A. G. Suits, X. Zhang, J. Rheinecker, L. B. Harding, and J. M. Bowman, Science **306,** 1158 (2004).

[8] D. W. Chandler, and P. L. Houston, J. Chem. Phys. **87,** 1445 (1987).

[9] A. T. J. B. Eppink, and D. H. Parker, Rev. Sci. Instrum. **68,** 3477 (1997).

[10] G. E. Hall, N. Sivakumar, P. L. Houston, and I. Burak, Phys Rev Lett **56,** 1671 (1986).

[11] J. A. Davidson, A. A. Viggiano, C. J. Howard, I. Dotan, F. C. Fehsenfeld, D. L. Albritton, and E. E. Ferguson, J. Chem. Phys. **68,** 2085 (1978).

[12] H. F. Davis, P. I. Ionov, S. I. Ionov, and C. Wittig, Chem. Phys. Lett. **215,** 214 (1993).

[13] J. Luque, LIFBASE Software, http://www.sri.com/psd/lifbase (2012).

[14] D. Townsend, M. P. Minitti, and A. G. Suits, Rev Sci Instrum **74,** 2530 (2003).

[15] G. M. Roberts, J. L. Nixon, J. Lecointre, E. Wrede, and J. R. R. Verlet, Rev. Sci. Instrum. **80,** (2009).

[16] M. P. Grubb, M. L. Warter, C. D. Freeman, N. A. West, K. M. Usakoski, K. M. Johnson, J. A. Bartz, and S. W. North, J. Chem. Phys. **135,** (2011).

[17] B. Whitaker, *Imaging in Molecular Dynamics* (Cambridge University Press, New York, 2003).

[18] H. F. Davis, B. S. Kim, H. S. Johnston, and Y. T. Lee, J. Phys. Chem. **97,** 2172 (1993).

[19] M. P. Ahmed, D.S.; Suits, A.G., *Atomic and Molecular Beams, the State of the Art* (Springer, New York, 2001).

[20] J. M. Brown, A. R. H. Cole, and F. R. Honey, Mol Phys **23,** 287 (1972).

[21] T. Amano, and E. Hirota, J Mol Spectrosc **53,** 346 (1974).

[22] R. M. Badger, A. C. Wright, and R. F. Whitlock, J Chem Phys **43,** 4345 (1965).

[23] J. F. Noxon, Can J Phys **39,** 1110 (1961).

[24] G. E. Hall, and P. L. Houston, Annu Rev Phys Chem **40,** 375 (1989).

[25] A. Bjorck, *Numerical Methods for Least Squares Problems* (SIAM, Philadelphia, 1996).

[26] Hall, Greg. Private correspondence, (2011).

[27] A. J. Orrewing, and R. N. Zare, Annu Rev Phys Chem **45,** 315 (1994).

[28] R. J. Gordon, and G. E. Hall, Adv Chem Phys **96,** 1 (1996).

[29] T. P. Rakitzis, and R. N. Zare, J Chem Phys **110,** 3341 (1999).

[30] A. S. Bracker, E. R. Wouters, A. G. Suits, and O. S. Vasyutinskii, J Chem Phys **110,** 6749 (1999).

[31] T. P. Rakitzis, and A. J. Alexander, J Chem Phys **132,** (2010).

[32] L. D. A. Siebbeles, M. Glassmaujean, O. S. Vasyutinskii, J. A. Beswick, and O. Roncero, J Chem Phys **100,** 3610 (1994).

[33] R. N. Dixon, J Chem Phys **85,** 1866 (1986).

[34] M. L. Costen, S. W. North, and G. E. Hall, J Chem Phys **111,** 6735 (1999).

[35] G. E. Hall, and M. Wu, J Phys Chem-Us **97,** 10911 (1993).

[36] T. P. Rakitzis, Chem Phys Lett **342,** 121 (2001).

[37] T. P. Rakitzis, P. C. Samartzis, and T. N. Kitsopoulos, Phys Rev Lett **8712,** (2001).

[38] J. A. Bartz, S. C. Everhart, and J. I. Cline, J Chem Phys **132,** (2010).

[39] V. K. Nestorov, R. D. Hinchliffe, R. Uberna, J. I. Cline, K. T. Lorenz, and D. W. Chandler, J Chem Phys **115,** 7881 (2001).

[40] A. L. Peden, R. D. Kieda, K. A. Breck, J. R. Basore, C. A. Kent, and J. A. Bartz, J Phys Chem A **114,** 10922 (2010).

[41] C. R. Gebhardt, T. P. Rakitzis, P. C. Samartzis, V. Ladopoulos, and T. N. Kitsopoulos, Rev Sci Instrum **72,** 3848 (2001).

[42] S. K. Lee, R. Silva, S. Thamanna, O. S. Vasyutinskii, and A. G. Suits, J Chem Phys **125,** (2006).

[43] T. P. Rakitzis, and T. N. Kitsopoulos, J Chem Phys **116,** 9228 (2002).

[44] S. K. Lee, D. Townsend, O. S. Vasyutinskii, and A. G. Suits, Phys Chem Chem Phys **7,** 1650 (2005).

[45] T. P. Rakitzis, G. E. Hall, M. L. Costen, and R. N. Zare, J Chem Phys **111,** 8751 (1999).

[46] C. H. Greene, and R. N. Zare, Annu Rev Phys Chem **33,** 119 (1982).

[47] Reprinted with permission from Grubb, M.P; Warter, M. L.; Freeman, C. D.; West, N. A.; Usakoski, K. M.; Johnson, K. M.; Bartz, J. A.; North, S. W. Journal of Chemical Physics 2011, 135, 092401, 2011. Copyright 2011, American Institute of Physics.

[48] W. Eisfeld, and K. Morokuma, J. Chem. Phys. **114,** 9430 (2001).

[49] H. H. Nelson, L. Pasternack, and J. R. Mcdonald, J. Chem. Phys. **79,** 4279 (1983).

[50] R. T. Carter, K. F. Schmidt, H. Bitto, and J. R. Huber, Chem. Phys. Lett. **257,** 297 (1996).

[51] Reprinted with permission from Grubb, M.P.; Warter, M. L.; Johnson, K. M.; North, S. W. Journal of Physical Chemistry A 2011, 115, 3218.. Copyright 2011, American Chemical Society.

[52] M. J. Berry, Chem. Phys. Lett. **27,** 73 (1974).

[53] R. Schinke, *Photodissociation Dynamics* (Cambridge University Press, Cambridge, 1993).

[54] J. S. Mcknight, and W. Gordy, Phys Rev Lett **21,** 1787 (1968).

[55] B. S. Kim, P. L. Hunter, and H. S. Johnston, J Chem Phys **96,** 4057 (1992).

[56] K. M. Christoffel, and J. M. Bowman, J. Phys. Chem. A **113,** 4138 (2009).

[57] J. Troe, Berich Bunsen Gesell **73,** 906 (1969).

[58] F. J. Lipscomb, R. G. W. Norrish, and B. A. Thrush, Proc R Soc Lon Ser-A **233,** 455 (1956).

[59] I. W. M. Smith, R. P. Tuckett, and C. J. Whitham, Chem. Phys. Lett. **200,** 615 (1992).

[60] H. Y. Xiao, S. Maeda, and K. Morokuma, J Phys Chem Lett **2,** 934 (2011).

[61] P. Andresen, G. S. Ondrey, and B. Titze, Phys. Rev. Lett. **50,** 486 (1983).

[62] J. E. B. M.N.R Ashfold, *Molecular Photodissociation Dynamics* (Royal Society of Chemistry, Letchworth, 1987).

[63] A. C. Luntz, J. Chem. Phys. **73,** 1143 (1980).

[64] F. Lahmani, C. Lardeux, and D. Solgadi, Chem. Phys. Lett. **129,** 24 (1986).

[65] A. E. Bruno, U. Bruhlmann, and J. R. Huber, Chem. Phys. **120,** 155 (1988).

[66] P. Andresen, G. S. Ondrey, B. Titze, and E. W. Rothe, J. Chem. Phys. **80,** 2548 (1984).

[67] P. L. Houston, and S. H. Kable, Proc. Natl. Acad. Sci. U.S.A. **103,** 16079 (2006).

[68] J. D. Farnum, X. B. Zhang, and J. M. Bowman, J. Chem. Phys. **126,** (2007).

[69] J. M. Bowman, and B. C. Shepler, Annu Rev Phys Chem **62,** 531 (2011).

[70] S. J. Klippenstein, Y. Georgievskii, and L. B. Harding, J. Phys. Chem. A **115,** 14370 (2011).

[71] L. B. Harding, S. J. Klippenstein, and A. W. Jasper, PCCP **9,** 4055 (2007).

[72] S. Maeda, and K. Ohno, Chem. Phys. Lett. **460,** 55 (2008).

[73] M. P. Grubb, M. L. Warter, K. M. Johnson, and S. W. North, J. Phys. Chem. A **115,** 3218 (2011).

[74] D. R. Cyr, D. J. Leahy, D. L. Osborn, R. E. Continetti, and D. M. Neumark, J Chem Phys **99,** 8751 (1993).

[75] D. C. Robie, M. Hunter, J. L. Bates, and H. Reisler, Chem Phys Lett **193,** 413 (1992).

[76] C. H. Hsieh, Y. S. Lee, A. Fujii, S. H. Lee, and K. P. Liu, Chem Phys Lett **277,** 33 (1997).

[77] G. E. Busch, and K. R. Wilson, J Chem Phys **56,** 3638 (1972).

[78] T. Suzuki, V. P. Hradil, S. A. Hewitt, P. L. Houston, and B. J. Whitaker, Chem Phys Lett **187,** 257 (1991).

[79] A. V. Demyanenko, V. Dribinski, H. Reisler, H. Meyer, and C. X. W. Qian, J Chem Phys **111,** 7383 (1999).

[80] R. P. Baker, M. L. Costen, G. Hancock, G. A. D. Ritchie, and D. Summerdeld, Phys Chem Chem Phys **2,** 661 (2000).

[81] R. Uberna, and J. I. Cline, J Chem Phys **102,** 4705 (1995).

[82] T. H. Baer, William L., *Unimolecular Reaction Dynamics: Theory and Experiments* (Oxford University Press, Oxford, 1996).

[83] J. T. Muckerman, J. Phys. Chem. **93,** 179 (1989).

[84] A. Benshaul, R. D. Levine, and Bernstei.Rb, J. Chem. Phys. **61,** 4937 (1974).

APPENDIX A

NO_2 VECTOR CORRELATION MEASUREMENTS

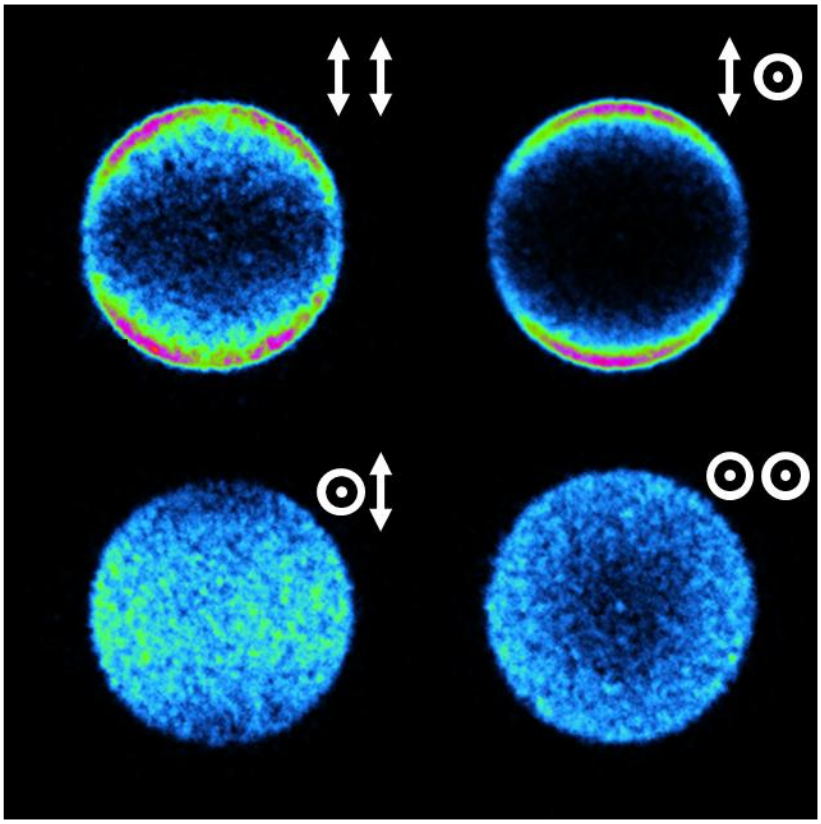

Figure A-1: Crushed ion images of NO (v=0, J=26.5) probed via the $Q_{11} + P_{21}$ transition arising from the 355 nm photolysis of NO_2. Images obtained using all four pump/probe polarization geometries are shown.[47]

In order to test the analysis of Chapter IV on a well-studied molecule, both traditional crush imaging and slice imaging experiments were performed on the NO_2 system. The photodissociation dynamics of NO_2 at 355 nm have been extensively studied and the scalar distributions,[75-76] spatial anisotropy,[77-79] and vector correlations[80-81] of the products have been previously reported. As a triatomic

molecule, conservation of angular momentum dictates that the NO fragment must exhibit strong **v** ⊥ **j** angular momentum polarization if it arises from a low J parent NO_2 molecule, which is expected in the case of a supersonic molecular beam expansion.

Crushed ion images for NO (v=0, J=6.5, 18.5, and 26.5) fragments were obtained from NO_2 photolysis at 355 nm. Images corresponding to four pump/probe polarization geometries of the NO (v=0, J=26.5) fragments probed via the $Q_{11} + P_{21}$ transition at 225.4 nm are shown in Figure A-1. To test Equations (4.7a)-(4.7d) against a known procedure for extracting the bipolar moments, the two-dimensional crush images were fit using the forward convolution method developed by Nestorov et al.[39] The approach, implemented in the program *fimage,* fits the experimental crush images with synthetic images using the semi-classical bipolar harmonic scheme developed by Dixon.[33] The synthetic images are a convolution of the bipolar harmonics expressions weighted by the bipolar moment parameters, with a displaced Gaussian speed distribution. In a fitting sequence, all four pump/probe polarization geometries are simultaneously fit by a corresponding set of synthetic images until a minimum in χ^2 is reached after which the bipolar moments are extracted. The total image intensities as well as the spatial signal distributions are used as constraints in the fitting process, and thus it is not necessary to assume the semi-classical limit in the analysis and $\beta_0^2(42)$ may be treated as a free parameter in the fit. The results of the analysis with both a free and fixed $\beta_0^2(42)$ parameter are provided in Table A-1.

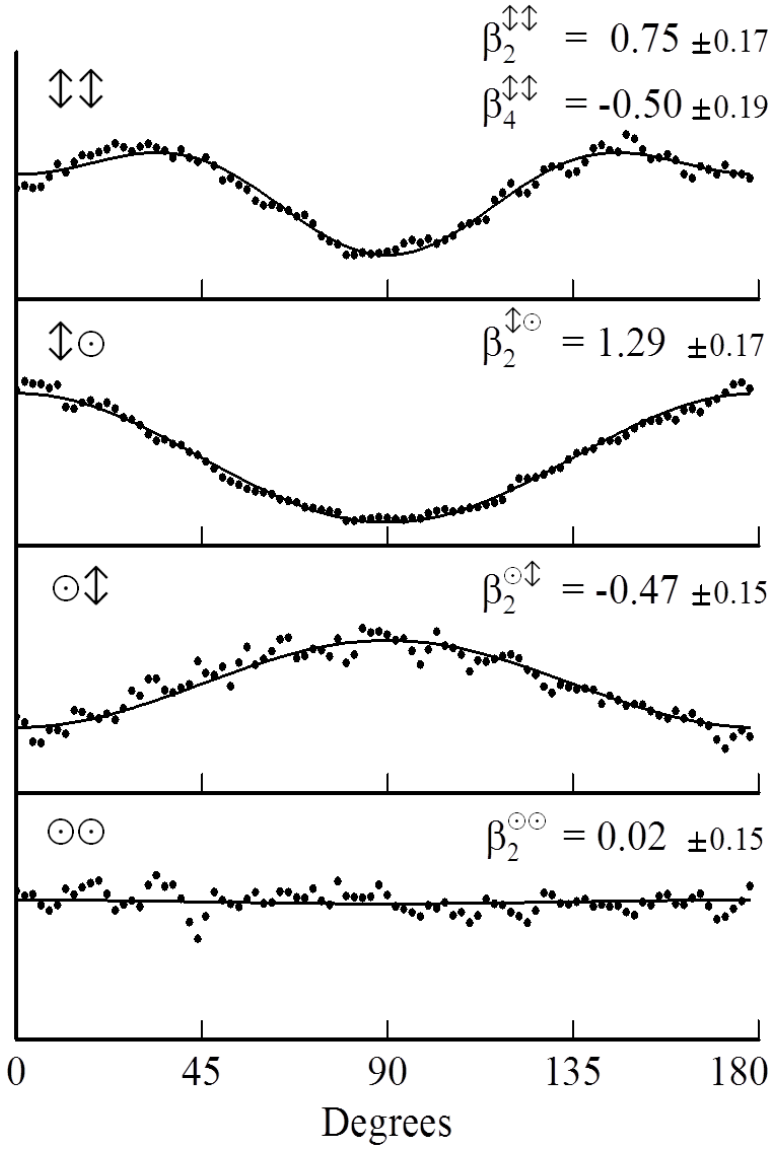

Figure A-2: Anisotropy arising from different laser polarizations. Finite width integrated angular distributions of the images shown in Figure 1 (closed symbols) and simulated distributions from the best fit to Equation (1) (solid lines).[47]

When the measured images consist of a single speed component, the signal at the maximum ion cloud radius is equivalent to the angular distribution that would be obtained from sliced imaging. We therefore analyzed the crushed ion images using Eqs. (4.7a-4.7d) by integrating a narrow radial range (5-8 pixels) around the outer edge of

each raw crushed image. The angular distributions obtained from the Figure 1 images in this manner are displayed in Figure A-2, along with their best fit β_k^{FG} coefficients. Because these images were probed through a mixed transition (90% Q_1 and 10% P_{21}), the resulting $\beta_Q^K(k_1k_2)$ parameters found from Eqs (4.7a-4.7d) assuming a pure Q branch transition must be modified to include the effect of both contributions. Equations (4.5a-4.5d) can be easily corrected for mixed transitions, as the contribution to the β_k^{FG} coefficients from different transition branches can be weighted and summed:

$$\beta_k^{FG}\left(h_{T1}^{(2)}, h_{T2}^{(2)}, \ldots h_{Tn}^{(2)}\right) = \chi_{T1}\beta_k^{FG}\left(h_{T1}^{(2)}\right) + \chi_{T2}\beta_k^{FG}\left(h_{T2}^{(2)}\right) + \ldots \chi_{Tn}\beta_k^{FG}\left(h_{Tn}^{(2)}\right) \quad \text{(A.1)}$$

Where χ_T is the fractional contribution of a particular transition. Solving these equations for the $\beta_Q^K(k_1k_2)$ moments however is not trivial, and so the uncorrected $\beta_Q^K(k_1k_2)$ moments from Eqs (4.7a-4.7d) were plugged into the mixed-transition corrected versions of Eqs. (4.5a-4.5d) and then adjusted until the experimental β_k^{FG} coefficients were matched.

Table A-1: Bipolar moments calculated from fimage and the analytical equations. Values obtained through iterative basis set fitting using the *fimage* software with both a four and five (in parenthesis) parameter fit as explained in the text. These values are compared to bipolar moment parameters obtained from the analytical expressions of Eqs. (4.7a)-(4.7d) applied to the same experimental images (Faux-sliced). The analytical expression for $\boldsymbol{\beta_0^2(42)}$ assumes the semi-classical approximation and is given by Eq. (4.2).[47]

	$b_0^2(20)$	$b_0^0(22)$	$b_0^2(02)$	$b_0^2(22)$	$b_0^2(42)$
$Q_{11} + P_{21}$ (26.5)	0.59 (0.59)	-0.30 (-0.31)	-0.27 (-0.27)	0.17 (0.17)	-0.23 (-0.25)
Faux-sliced:	0.66 ± 0.06	-0.30 ± 0.05	-0.26 ± 0.10	0.18 ± 0.07	-0.23 ± 0.05
$Q_{11} + P_{21}$ (18.5)	0.69 (0.69)	-0.28 (-0.28)	-0.27 (-0.27)	0.28 (0.28)	-0.27 (-0.27)
Faux-sliced:	0.73 ± 0.07	-0.28 ± 0.06	-0.30 ± 0.12	0.18 ± 0.07	-0.25 ± 0.06
$Q_{22} + R_{12}$ (6.5)	0.44 (0.44)	-0.05 (-0.05)	-0.11 (-0.11)	0.18 (-0.18)	-0.14 (-0.14)
Faux-sliced:	0.54 ± 0.11	-0.21 ± 0.11	-0.24 ± 0.21	0.09 ± 0.10	-0.18 ± 0.12

The resulting bipolar moments obtained from both analysis methods are shown in Table A-1. The values of the NO state selected bipolar moments given in Table A-1 are consistent with the work of Baker et al. which were based on Doppler profile analysis in both a 300 K thermal sample and a 10 K molecular beam.[80] No attempt was made to correct the values to account for depolarization due to the parent velocity distribution. Given the approximate temperature of the molecular beam such corrections are <10% for even the highest detected NO rotational states. The spatial anisotropy parameters, $\beta = 2\beta_0^2(20)$, are consistent with the values reported by Demyanenko et al. including the decrease in magnitude between J=18.5 and J=26.5 due to reorientation of the asymptotic velocity to conserve angular momentum.[79] The **v-j** $\beta_0^0(22)$ and **μ-j** $\beta_0^2(02)$ correlations are consistent with the dissociation of a triatomic molecule from an initially low rotational parent with the transition dipole in the plane and in agreement with previous measurements. The non-limiting **v-j** correlation is not unexpected given depolarization due to both thermal motion and initial parent rotational angular momentum which provides both out-of-plane motion (helicity) and in-plane motion which results in a deviation from the axial recoil limit.

The bipolar moments obtained from fimage with a four parameter fit (with $\beta_0^2(42)$ fixed by the semi-classical approximation in Equation 4.2) give nearly identical results to the bipolar moments obtained from the full five parameter fit, which is consistent with the assumed high-j limit. The results from the fimage analysis is also in good agreement with those obtained from Equations (4.7a-4.7d), with minor deviations expected since only a small fraction of the total ion signal is used for the faux-slicing

method. This is a noted advantage in cases where there is significant background noise in the center of the image. For instance, the Q_{22} + R_{12} (6.5) image contains a massive center spot due to the rotationally cold free NO present in the molecular beam, which posed a significant challenge in the fimage analysis. Despite obvious qualitative anisotropy in raw images indicating the presence of a significant **v-j** correlation, fimage returned smaller than expected values for the $\beta_0^0(22)$ and $\beta_0^2(02)$ parameters due to this background signal. Slice imaging is naturally immune to such issues since only the high speed signal is analyzed, and thus provides more reliable vector correlations for such cases. As an additional check on the equivalence of the two analysis methods, both methods were applied to a simulated ion image and resulted in excellent agreement with the true bipolar moments.

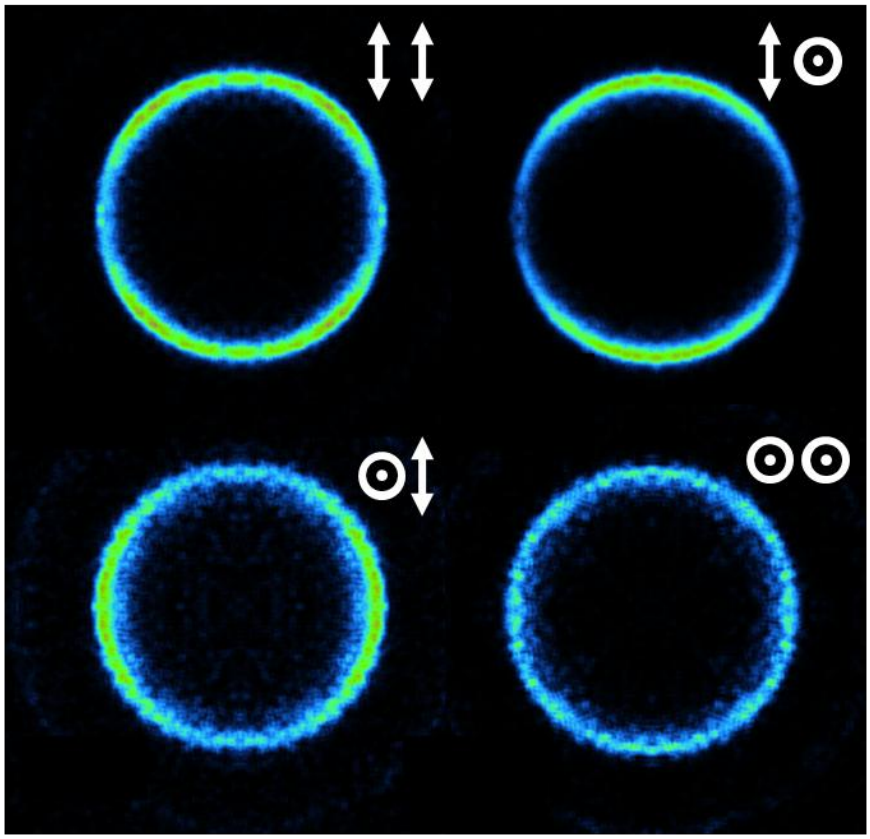

Figure A-3: Sliced ion images of NO (v=0, J=26.5) probed via the $Q_{11} + P_{21}$ transition arising from the 355 nm photolysis of NO_2. Images obtained using all four pump/probe polarization geometries are shown.[47]

To demonstrate the intended use of our analysis method, sliced ion images of the NO_2 system were also obtained (Figure A-3). The bipolar moments derived from the experimental sliced images are given in Table A-2. Although the bipolar moments obtained from these images do not compare unfavorably to those in Table 1 from crushed ion images, it should be noted that they were obtained on a different experimental apparatus. Subtle differences are consistent with variations in beam conditions which result in differences in the initial parent velocity distribution and rotational temperature. A molecular beam with a slightly warmer rotational temperature

results in smaller observable vector correlations. A comparison to the analysis of non-sliced images on the same apparatus yielded consistent results.

Table A-2: Bipolar moment parameters of sliced NO_2 images. These values were obtained using the analytical expressions of Eqs. (4.7a)-(4.7d). The analytical expression for $\boldsymbol{\beta_0^2(42)}$ assumes the semi-classical approximation and is given by Eq. (4.2).[47]

	$\beta_0^2(20)$	$\beta_0^0(22)$	$\beta_0^2(02)$	$\beta_0^2(22)$	$\beta_0^2(42)$
$Q_{11} + P_{21}$ (26.5)	0.43 ± 0.06	-0.26 ± 0.04	-0.20 ± 0.07	0.09 ± 0.05	-0.15 ± 0.03
$Q_{11} + P_{21}$ (18.5)	0.52 ± 0.09	-0.18 ± 0.05	-0.21 ± 0.08	0.12 ± 0.07	-0.17 ± 0.03
$Q_{22} + R_{12}$ (6.5)	0.46 ± 0.06	-0.10 ± 0.05	-0.09 ± 0.12	0.04 ± 0.07	-0.07 ± 0.06

APPENDIX B

$NO_3 \rightarrow NO_2$ + O PRODUCT CHANNEL

Images of the O (^3P_J) fragments originating from the O (^3P_J) + NO_2 atomic elimination channel were obtained at wavelengths between 582 nm and 598 nm, both above and below the 0 K channel thresholds. All the measured images were isotropic ($\beta=0.1 \pm 0.2$) consistent with the lifetimes reported by Davis et al.[12] The branching between the three spin-orbit states of oxygen as a function of wavelength was found by integrating the total image signal of each selectively ionized spin-orbit state and subtracting the background NO_2 signal from probe beam dissociation. The results for photodissociation at 583 nm are presented in Table B-1. The experimental fine structure branching ratios are very close to the statistical prediction, as expected for a barrierless dissociation on the ground state potential energy surface.

Table B-1. Experimental and statistical branching ratios of O (^3P_J) products resulting from NO_3 photodissocation at 583 nm.[51]

	Experimental	**Statistical**
O ($^3P_2$)	0.54±0.05	0.55
O ($^3P_1$)	0.38±0.08	0.33
O ($^3P_0$)	0.08±0.03	0.11

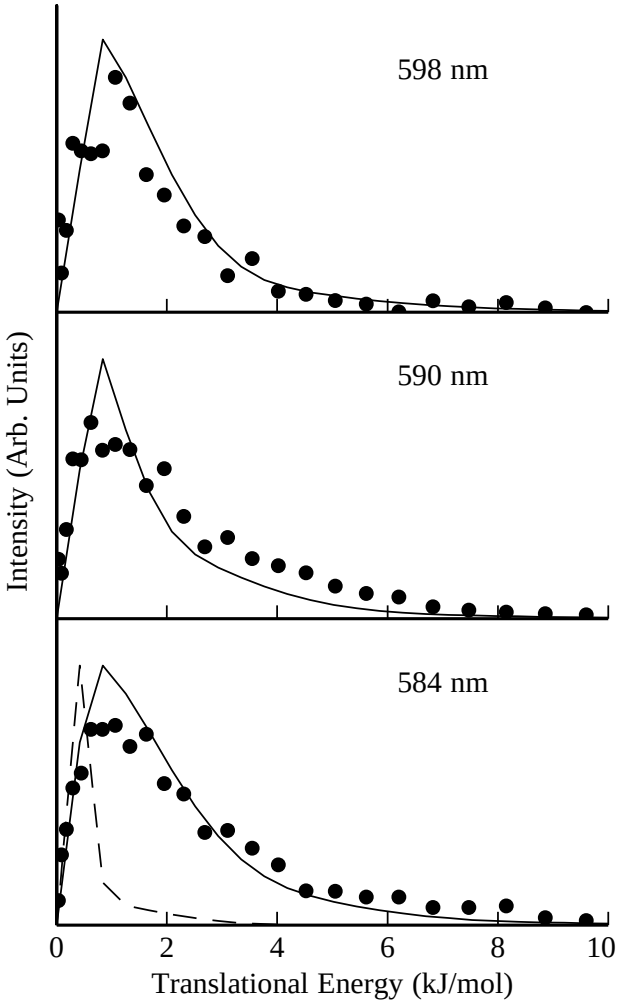

Figure B-1. Total translational energy distributions of $NO_3 \rightarrow O(^3P_2) + NO$ resulting from NO_3 photodissociation at three pump wavelengths (symbols). Also shown are simulated prior distributions assuming a parent NO_3 rotational temperature of 20 K and vibrational temperatures of 300 K (solid line) and 100 K (dashed line).[51]

The $I(E_T)$ distributions derived from $O(^3P_2)$ images were not sensitive to photolysis wavelength over the range from 582 nm to 598 nm, and we observed no significant difference between the $O(^3P_j)$ images at a given wavelength. The distributions measured at 584 nm, 590 nm, and 598 nm are shown in Figure B-1 (filled circles) and are all broad and peak near zero translational energy as expected for barrierless dissociation.[82] The results are in good agreement with the state-averaged distributions

reported by Davis et al.[18] which is not surprising given the similarity between the $I(E_T)$ distributions associated with each oxygen fine structure state. We have modeled the $I(E_T)$ distributions using a prior distribution[83-84], suitable for describing statistical energy partitioning, to further characterize the initial parent NO_3 energy distribution. The $I(E_T)$ distributions were of the following form,

$$P(f_T) = (f_T)^{1/2}(1 - f_T)^{7/2} \quad \text{(B.1)}$$

where f_T is the fraction of the available energy in translation.[83] Distributions for each ro-vibrational state of the parent NO_3 were weighted according to assumed Boltzmann temperatures for both rotation and vibration. We find that the final distributions are sensitive to the parent internal energy, as measurements lying below the 0 K channel threshold necessarily arise from the dissociation of rotationally and vibrationally excited parent molecules. Prior distributions assuming an NO_3 rotational temperature of 20 K and vibrational temperature of 300 K provide a satisfactory fit to the data are shown as the solid lines in Figure B-1, consistent with the results of the temperature characterization detailed in Chapter V.A. Lowering the parent vibrational distribution to 100 K (dashed line) results in a colder $I(E_T)$ distribution than observed, but the modeled distribution was less sensitive to the parent rotational temperature which is more accurately determined in Chapter V.A. The higher vibrational temperature of the beam is not unexpected given the heated source and the higher efficiency for rotational cooling relative to vibrational cooling in the jet expansion.

VITA

Michael Patrick Grubb received his Bachelor of Science degree in chemistry from Texas A&M University in 2007. He entered the chemistry graduate program at Texas A&M University in August of 2007, and received his Doctor of Philosophy degree in May 2012.

Michael Grubb may be reached at Chemistry Department, c/o Dr. Simon W. North, TAMU, College Station, TX, 77843-3255. His email is mgrubb@mail.chem.tamu.edu.